Structural, thermal and electrochemical studies of nano tungsten carbides

A

Thesis

Submitted in partial fulfillment of the

requirements for the award of degree of

DOCTOR OF PHILOSOPHY

By

Gourav Singla

(Registration No. 901112008)

Under the supervision of

Dr. O. P. Pandey
Senior Professor &
Dean (R&SP)

Dr. Kulvir Singh
Professor &
Associate Dean (Strategy)

School of Physics and Materials Science

Thapar University, Patiala – 147 004 (INDIA)

August-2016

Dedicated to Parents

THAPAR
UNIVERSITY
(Declared as Deemed-to-be-University u/s 3 of the UGC Act, 1956)
Thapar Technology Campus, Post Box No. 32
Patiala 147 004 Punjab India
Fax : +91-175-2364498, 2393005
URL : www.thapar.edu

CERTIFICATE

This is to certify that this thesis entitled **"Structural, thermal and electrochemical studies of nano tungsten carbides"** which is being submitted by **Mr. Gourav Singla** in partial fulfilment of the requirements for the award of the degree of Doctor of Philosophy in the School of Physics and Materials Science, Thapar University, Patiala, Punjab, India is an exclusive record of candidate's own research work under our supervision. The thesis in part or in full has not been submitted in any other university or institute for the award of any degree. The thesis is fit to be considered for the award of degree of Doctor of Philosophy.

Dr. O.P. Pandey
Senior Professor and Dean (R&SP)
School of Physics and Materials Science
Thapar University
Patiala-147 004 (INDIA)

Dr. Kulvir Singh
Professor and Associate Dean (Strategy)
School of Physics and Materials Science
Thapar University
Patiala-147 004 (INDIA)

Index

Acknowledgments

It is my pleasure to express my deep sense of thanks and acknowledge the contribution of several individuals who journeyed with me since I have started to work on this thesis. Without their guidance and help in one way or another, this dissertation would not have been completed.

It is my pleasure to express my deep sense and gratitude first to my supervisors **Dr. O. P. Pandey,** Senior Professor and Dean (R&SP) and **Dr. Kulvir Singh,** Professor and Associate Dean (Strategy), Thapar University, Patiala for their encouragement and endless support throughout this journey. I am forever in debt to them for their timely suggestions with kindness, to generate enthusiasm and inspiration in me for research during my entire Ph.D. tenure.

It is my privilege to thank **Prof. Prakash Gopalan**, Director, Thapar University, Patiala for providing me resources in the university and needful help during the various stages of my work. I would also like to thank **Dr. Manoj Sharma,** Head, School of Physics and Materials Science, Thapar University, Patiala for his kind help and co-operation during my research work.

I would like to thank **Department of Science and Technology** (Government of India, New Delhi) and **Thapar University** (Patiala) for financial support to accomplish this project.

I take this opportunity to record my sincere thanks to my doctorate committee members **Dr. N. K. Verma, Dr. Amjad Ali** and **Dr. B. N. Chudasama** for their constructive suggestions and critical comments during my progress report presentations. I also acknowledge **Dr. K. K. Raina**, **Dr. Puneet Sharma**, **Dr. B.C. Mohanty, Dr. S. D. Tiwari, Dr. D. P. Singh, Dr. S. Jana** and **Dr. Suneel Kumar** for their support whenever I approached them.

I also thank to **Ms. Loveleen K Brar** for her suggestions and help throughout my research work.

I would like to acknowledge my sir **Dr. Satish Kumar Sharma** (SMCA, Thapar University) for providing me moral support timely.

My sincere thanks to **Dr. Akshay Kumar,** Assistant professor, Sri Guru Granth Sahib World University, Fatehgarh Sahib for providing me all possible help during my initial research work starting from M.Tech. project.

I am highly grateful to my seniors **Dr. Jasmeet Grewal, Dr. Gurbinder Kaur, Dr. Kamalpreet Kaur, Dr. Vishal Kumar, Dr. Ravi Shukla, Dr. Parveen Kumar, Dr. Bhupinder Kaur, Dr. Harjinder Singh, Dr. Manoj Sharma, Dr. Mukesh, Dr. Ranvir Singh Panwar, Dr. Kapil Sood and Dr. Sanjay Kumar** who have been the constant source of moral support throughout my research work.

I am privileged for having best friends **Mr. Paramjyot Kumar Jha** and **Mr. Suresh Kumar** who provided great company during this journey. Even though they are not directly involved in this study but it was great pleasure to work with them and appreciate their ideas, help and good humor.

I would like to include a special note of thanks to **Ms. Mani Mahajan** for her critical suggestions, consistent help, moral support and encouragement all the time specifically during the completion of this manuscript.

I am highly thankful to my friend **Dr. Akash Katoch** for his unconditional support whenever I really feel his help in my research.

I am thankful to my colleague **Dr. Samita Thakur, Dr. Jagdeep Kaur, Dr. Chandni, Dr. Mintu Tyagi, Mrs. Shiwani Sharma Malhotra, Mr. Sunil Kuamr Arya, Mr. Satwinder Singh, Mrs. Pooja Singla, Mrs. Parveer Bassi and Dr. Bhupinder Pal Singh** for their help whenever I approached them.

I also thank to my juniors **Mr. Rameez Ahmed**, **Mr. Aayush Gupta, Mr. Gourav Sharma, Ms. Navjot, Ms. Purnima Sharma, Mrs. Anu Gupta, Mr. Anoop Pratap Singh, Mr. Savid Khan, Mr. Piyush Sharma** and **Mr. Santosh** for their whole-hearted support.

I would like to thank **Mr. Sumit Bhardwaj (Research Scholar, NIT Hamirpur)** and **Mr. Samir (Research Scholar, IIT Delhi)** for their help whenever I needed them.

I am also thankful to **Mr. Purushotam, Mr. Jant Singh, Mr. Indermani Mishra, Mr. Sukhvinder Verma, Mrs. Praveen, Mrs. Neelam, Mr. Lalji Verma, Mr. Vijay, Mr. Pardeep Singla** for their valuable support in one way or another during my entire research work. All the staff members of **SAI Lab and Mechanical Workshop,** Thapar University, Patiala is also highly acknowledged for helping me in my research work.

I could not forget to give my sincere thanks to **Mr. S.P. Singh** (CTR, Ludhiana) for his dedication to help me whenever I approached him.

Last but not least, my deepest appreciation belongs to **my family**. Although you have not been literally beside me when I am finishing this manuscript, I would like you to know that you are all my inspirations and motivations for everything. Thank you for supporting me and allowing me to follow my ambitions. Without your endless support, enduring love, constant guidance, motivations, prayer and encouragement, I could not have completed this project of my life.

Above all, the hidden force by **Almighty God** for their precious blessings and positive energy to sustain during all stages of this work. I would also like to thank him for all the special people that surround me.

Gourav Singla

(Gourav Singla)

List of SCI Publications

From Ph.D. work

1. **Gourav Singla**, K. Singh, O. P. Pandey, Williamson–Hall study on synthesized nanocrystalline tungsten carbide (WC), *Applied Physics A* 113 (2013) 237–242.
2. **Gourav Singla**, K. Singh, O. P. Pandey, Structural and thermal analysis of in situ synthesized C–WC nanocomposites, *Ceramics International* 40 (2014) 5157–5164.
3. **Gourav Singla**, K. Singh. O.P. Pandey**,** Effect of Processing Variables on WC Nanoparticles Synthesized by Solvothermal Route, *Particulate Science and Technology*, 33 (2015) *36-41*.
4. **Gourav Singla**, K. Singh, O. P. Pandey, Synthesis of carbon coated tungsten carbide nano powder using hexane as carbon source and its structural, thermal and electrocatalytic properties, *International Journal of Hydrogen Energy* 40 (2015) 5628-5637.
5. **Gourav Singla**, K. Singh, O. P. Pandey, Study on single step solid state synthesis of WC@C nanocomposite and electrochemical stability of synthesized WC@C & Pt/WC@C for alcohol oxidation (methanol/ethanol), *Journal of Alloys and Compounds* 665 (2016) 186–196.
6. **Gourav Singla**, K. Singh, O. P. Pandey, Catalytic activity of tungsten carbide-carbon (WC@C) core-shell structured for ethanol electro-oxidation, Materials Chemistry and Physics (*under Review*).

Other than Ph.D. work

1. **Gourav Singla**, K. Singh, O.P. Pandey, Structural and thermal properties of in-situ reduced WO_3 to W powder, *Powder Technology* 237 (2013) 9–13.
2. **Gourav Singla**, Paramjyot Kumar Jha, Jasmeet Kaur Gill, and K. Singh, Structural, thermal and electrical properties of Ti^{4+} substituted Bi_2O_3 solid systems**,** Ceramics International 38 (2012) 2065–2070.
3. Paramjyot Kumar Jha, Jasmeet Kaur Gill, **Gourav Singla**, K. Singh and O. P. Pandey, Structural, thermal and electrical properties of (100-x) ZrO_2 (x) Bi_2O_3 compound, Ionics 18 (2012) 759–767.
4. **Gourav Singla**, K. Singh, Dielectric properties of Ti substituted $Bi_{2-x}Ti_xO_{3+x/2}$ ceramics, Ceramics International 39 (2013) 1785–1792.

5. **Gourav Singla**, K. Singh, Effect of TiO_2 on the photo catalytic properties of Bismuth oxide, Environmental Technology. 35 (2014) 1520-1524.
6. Loveleen K. Brar, **Gourav Singla**, Navjot Kaur, O. P. Pandey, Thermal stability and structural properties of Ta nanopowder synthesized via simultaneous reduction of Ta_2O_5 by hydrogen and carbon, Journal of Thermal Analysis and Calorimetry 119 (2015) 175-182.
7. Loveleen K Brar, **Gourav Singla** and O. P. Pandey, Evolution of structural and thermal properties of carbon-coated TaC nanopowder synthesized by single step reduction of Ta-Ethoxide, RSC Adv. 5 (2015) 1406-1416.
8. Mani Mahajan, **Gourav Singla**, K. Singh, O.P. Pandey, Synthesis of grape-like carbon nanospheres and their application as photocatalyst and electrocatalyst, Journal of Solid State Chemistry 232 (2015) 108–117.

List of papers presented in conferences (National/International)

1. **Gourav Singla**, K Singh, O P Pandey**,** Time effect on synthesis of Nanocrystalline tungsten carbide, International Conference On Energy Efficient Materials Manufacturing Methods & Machineries For Ceramic Industries ((**IC2E4MCI-11**), held on December 19-20, 2011 at Agra.
2. **Gourav Singla**, K Singh, O P Pandey, A New Route to Synthesis Nanocrystalline Tungsten Carbide, National conference on Recent Trends in Materials Science Research (**RTMSR**) held on September 3-5, 2012 in National Institute of Technology (NIT)-Srinagar.
3. **Gourav Singla**, K. Singh and O. P. Pandey, Synthesis of Nanocrystalline Tungsten Carbide (WC) Powder, International conference on recent trends in applied physics and materials science (**RAM-2013**) held on Feb. 1-2, 2013 at Govt. College of engineering and technology, Bikaner.
4. **Gourav Singla**, K. Singh and O. P. Pandey, Effect of processing variables on WC nanoparticles synthesized by solvothermal route, International Conference & Exhibition of Powder, Granule and Bulk Solids: Innovations and Applications held on November 28-30, 2013 at Thapar University, Patiala, India.
5. **Gourav Singla**, K. Singh and O. P. Pandey, Synthesis of nanocrystalline tungsten carbide (WC) powder, National Conference on Innovative molecules for Sustainable Future, **NCIMSF-2013** held on October 24-26, 2013 at Thapar University, Patiala, India.
6. **Gourav Singla**, K. Singh and O. P. Pandey, Synthesis of carbon coated tungsten carbide for catalytic application in fuel cells, First International Conference on Emerging Trends in Engineering & Applied Sciences, held on December 27-28, 2013, Jaipur, India.
7. **Gourav Singla**, K. Singh and O. P. Pandey, In-situ reduction/carburization WO_3 by hydrocarbon, National conference on Microscopy in Materials Science and Biomimetic Technology, held on February 26-28, 2015, Kanpur, India.
8. **Gourav Singla**, K. Singh and O. P. Pandey, Structural, thermal and electrochemical study of single step synthesized WC nanopowder, 17^{th} Topical Meeting of the International Society of Electrochemistry, from 31 May to 3 June 2015, in Saint-Malo, France.
9. **Gourav Singla**, K. Singh and O. P. Pandey, Role of hydrocarbon in the reduction/carburization of tungsten oxide, 2^{nd} conference on the Microscopy in Materials Science (**AMST**), from February 25-27, 2016, in Thapar University, Patiala.

List of Figures

Page No.

Chapter 1

Chapter 3

Chapter 4

Chapter 5

List of Tables

Preface

Among all the available carbide materials, carbides of tungsten (WC/W_2C) are unique class of materials exhibiting versatile applications in the field of mechanical and electrochemical engineering. Further, it is observed that the materials at nano scale can be used for different electrical, electronics, mechanical, chemical and electrochemical applications, thus widening their demands. These widened applications are due to their different morphological features. The performance of WC especially in electrochemical devices can be enhanced by reducing their size. Due to their smaller sizes, it attains higher surface area, which provides additional active sites for reactants. So the synthesis of tungsten carbide nano powder has become the subject of interests where main focus is to meet the demands of industry. Many recent important technological breakthroughs can be attributed to the ongoing developments in the synthesis of WC nano powder. The synthesis of WC nanoparticles normally includes control of size and shape. Conventionally, the synthesis of WC done at high temperature (> 1400 ºC) involving many intermediate steps. Therefore, there is a need to develop new synthesis routes to obtain the product at relatively lower temperature in single step.

The present work deals with the synthesis and characterization of tungsten carbide(s) (WC/W_2C) nano powder by thermo-chemical route. Further, the prepared materials have been tested as electrocatalyst in acidic and alcohol media. The entire work of the thesis is divided into six chapters.

- In **Chapter 1,** the details of the transition metal carbides (TMCs) with their crystal structure and properties are given. Among all the TMCs, the importance of tungsten carbide(s) has been focused and presented. The phase diagram of tungsten–carbon along with the crystal structures of different allotropes ($WC/W_2C/WC_{1-x}$) of tungsten carbide(s) is also described. The applications of the WC in mechanical and energy production are discussed. At last a brief idea about the different synthesis techniques adopted for the preparation of tungsten carbide(s) nano powder has been described.
- **Chapter 2** presents the literature on the synthesis of WC/W_2C nano powder, obtained through different method by using different tungsten precursors in the presence of different carbon source and reducing agents. In literature work, all the efforts made by different group for getting carbide(s) (WC/W_2C) powder at nano scale has been described by giving the details of synthesis conditions. Furthermore, the work on the

electrochemical activity of the nano crystalline tungsten carbide powders with Pt and Pd as supporting materials done by the other groups has been presented.

- **Chapter 3** describes the detail of experimental procedure followed for the synthesis of WC and W_2C nanopowders from WO_3. The different techniques like X-ray diffraction (XRD), Thermal analysis (TGA/DTG/DSC), Transmission electron microscopy (TEM), Raman spectroscopy, BET analysis used for the characterization of prepared nano powders have been discussed in this chapter. To check the feasibility of the synthesized powders for catalytic activity, the electrochemical measurements have been performed. For this, the details of sample preparation and their testing have also been given in this chapter.
- **Chapter 4** deals with the results and discussion part of the present work. It has been presented in two sections. In the first section the synthesis of tungsten mono-carbide (WC) nano powder by thermo-chemical route with three different carbon sources has been described. The reaction path for the reduction and carburization with temperature and time has been presented for all three carbon sources. On the basis of reaction path the reaction mechanism for obtaining WC nano particles have also proposed. The thermodynamic study has been done to predict the feasibility of reduction and carburization reactions at different temperature. Further, the structural, thermal, surface area and micro structural analysis have been done for all the samples.
- In the second section, the formation of tungsten semi-carbide (W_2C) nano powders under the influence of fast cooling has been discussed. In this section the same carbon source viz acetone, activated charcoal and hexane have been taken. For obtaining the W_2C nano powder the optimization in the synthesis conditions has been done by varying temperature, time and carburizing agent amount. Among all the obtained products, the best sample which contained higher amount of W_2C has been characterized using different techniques for structural, thermal analysis, Raman, specific surface area and microstructural analysis.
- **Chapter 5** deals with the results related to the suitability of the obtained product as electrocatalyst in acidic and alcohol media with and without depositing platinum nano particles. The effect of alcohol concentration on the electrocatalytic activity of prepared electrocatalyst has also been analyzed in this chapter.

- In **chapter 6**, the entire work of the present study is summarized and concluded. The present work shows that tungsten carbide(s) nano powder having different morphology can be synthesized from WO_3 by changing the carburizing agent in single-step. The conclusion made on the synthesis of carbide nano powder has been presented. Moreover, the results obtained from the electrochemical study of prepared carbide have also been concluded in this chapter and found that the product obtained from solid carbon source attributes better electrochemical properties than the liquid carbon sources.

CHAPTER 1

INTRODUCTION

Overview

In this chapter the details of the transition metal carbides (TMCs) with their crystal structure and properties are given. Among all the TMCs, the importance of tungsten carbide(s) has been presented. The history on the development of tungsten carbide is also mentioned. The phase diagram of tungsten–carbon along with the crystal structures of different allotropes ($WC/W_2C/WC_{1-x}$) of tungsten carbide(s) is also discussed. The applications of the WC in the form of cemented carbide (WC-Co) for mechanical and platinum deposited active catalyst (Pt/WC) for energy production applications are discussed. At last a brief idea about the different synthesis techniques for the preparation of tungsten carbide(s) nano powder with their limitations has been described.

1.1 Transition metal carbides (TMCs)

The term carbides are only applied to those compounds which are formed by carbon and other elements of lower or equal electronegativity. Metal carbides because of higher strength and durability constitute a diverse class of materials and traditionally have been used in extreme conditions of temperature and pressure; for example, in rocket nozzles and drill bits. The higher hardness property increases its usage in cutting tools, golf shoe spikes and in ferrous alloys to enhance the toughness of steels. Moreover, due to the higher melting point (>1800 °C) these carbides are also called *refractory* carbides **[1]**.

Among all types of carbides, the interstitial carbide known as transition metal carbides (TMCs) from group IV-VI is only carbide, which meets the criteria of refractory and its structure leads to combinations of metallic, covalent and ionic bonds. Although in carbides, the C-atoms are situated in the interstitial voids of the metallic sublattice to form a nonmetallic sublattice **[2]** but these interstitial C-atoms have greater influence on the crystal structure and certain properties of the parental metal lattice. Moreover, due to the stability of interstitial carbides over a broad range of composition, it can be considered essentially as non-stoichiometric materials **[3]**. In other words, there exist vacancies in terms of missing C-atoms within the lattice of carbides which are called structural vacancies. However, the presence of these vacancies is a characteristic feature of carbides that are related to the group of non-stoichiometric compounds. The concentration of vacancies as well as their ordered or disordered distribution in a crystal lattice has a strong effect on the properties of such carbides. Because of such a kind of nature, TMCs have highest melting point, high thermal and chemical stability and could be considered as potential low cost substitutes for now-a-days industrial refractory materials.

1.2 Crystal structure of interstitial metal carbides/TMCs

Since, in carbides the metallic sub lattice symmetry differs from that of transition metallic lattices, hence, the crystal structure of metals get modified with the formation of carbides e.g. metals with the body centered cubic (bcc) structure (W, Nb, Mo, Ta, V, Cr) form carbides having cubic or hexagonal metallic sublattices. Moreover, both the experimental and theoretical studies also confirm that with introducing C-atom into the lattice of the early transition metals an expansion of the lattice constant occurs **[4]**. The changes within the crystal structure of metals after the formation of carbides attribute strong metal-carbon

interactions while direct interactions between carbon atoms are negligibly small **[5]**. Such kind of variation has been explained by Hagg's rule. According to Hagg's rule the formed structure depends on the ratio $r = r_X/r_M$; where r_X and r_M corresponds to the radii of the nonmetal (C atom) and metal atoms, respectively. When r is less than 0.59, the common structures will be simple like face-centered cubic (fcc), hexagonal closed packed (hcp) or simple hexagonal (hex), with the C atoms placed in the large interstitial sites of octahedral. However, with the increase in value of r greater than 0.59, the metallic arrangement distorts and forms complicated structure. When r is less than 0.59, the light elements are accommodated in the large interstitial sites of the relatively simple host metal structure. The interstitial site must be smaller than the interstitial atom to avoid insufficient bonding between C-atoms and metal atoms, which makes the structure unstable. On the other hand, the interstitial site should not be too much smaller than the interstitial atom otherwise the interstitial atom will expand the host metal lattice. It leads to weak the metal-metal interactions, and the structure will lose its stability.

It has been shown that the TMCs shows the range of performances depending on the nature of the metal centers, the carbon (C)/metal (M) ratio, and orientation of the carbide surfaces **[6-8]**. The increase in M/C ratio in moving towards the right in the periodic table represents the rejection of C by the metal and reflects the decreasing stability of the carbides.

1.3 Properties of carbides

- The bonding in carbides arises due to the interaction of carbon *2s* and *2p* orbital with d orbital of metal. Moreover, due to the comparable electronic properties of carbides with noble metal, tungsten carbide (WC) has an electrocatalytic property similar to platinum (Pt).
- The physical and mechanical properties of carbides resemble to ceramic materials but not to metals. Carbides are well known materials for high melting point, higher hardness and strength. These properties are even highest as compared to ceramic materials.
- The electric and magnetic properties of carbides are similar to metals. The carbides have higher resistivity than pure metals, but the region of resistivity still exists within the range of metals. Moreover, the carbides also show paramagnetism with lower magnetic susceptibility within the range of magnitude of parent metal.

As shown in **figure 1.1**, transition metal carbides (TMCs) become the backbone of several components and utilized for different applications like metal cutting, mining, rock drilling, wear parts, corrosion resistance parts, coating materials, catalyst, thermal protection systems, superconductor, hypersonic vehicles **[4, 9-14]**. However, in most of the high-performance applications, the material of choice among TMCs is ultimately based upon tungsten carbide(s) (WC/W_2C) either as cemented carbide WC-Co for mechanical tools **[15-18]** or electrocatalyst used in fuel cell applications **[19-21]**.

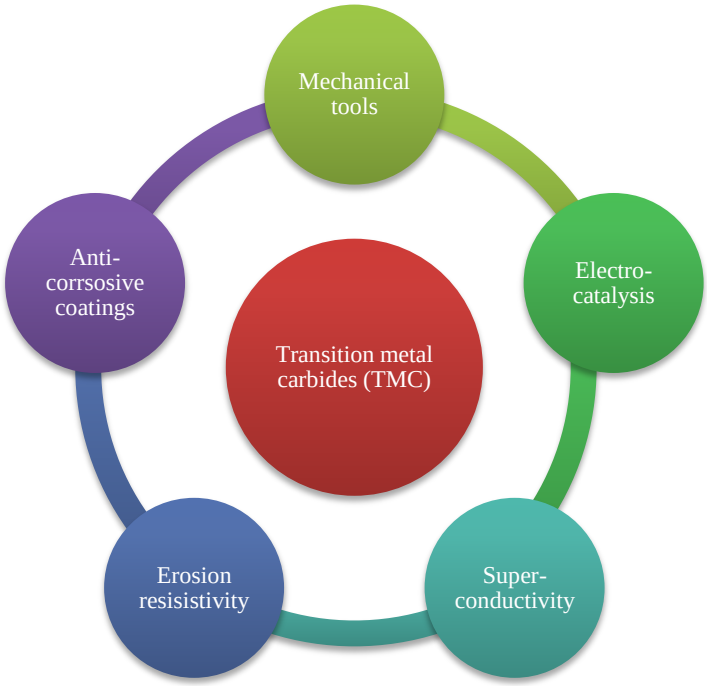

Figure 1.1: Applications of transition metal carbides.

1.4 Properties of tungsten carbide (WC)

Tungsten carbide (WC) was first synthesized by H. Moissan in 1893. Moissan had also produced fused tungsten metal by the electro-thermal way (earlier tungsten metal produced which is only in the form of a powder) in 1897. Since, in metal carbide (MC), the C-atoms modify the chemical reactivity through ensemble and ligand effects to moderate level **[22-24]**, so due to the presence of the C-atoms the number of metal atoms will be limited that can be exposed to metal carbide surface. Moreover, the formation of metal-carbon (M-C) bonding changes the electronic properties of the metal **[25]**. Hence, the specific features of formed compound are the combinations of main attributes of parental metal (thermal and electrical conductivity) and compound (hardness). So, the metal carbides can exhibit clear advantages over their parent metals in terms of activity, selectivity, and durability **[22]**. Moreover,

partially filled *5d* subshell of W extends outward to the periphery of the atom and is strongly influenced by carbon atom. Since, the change of symmetry and a slight expansion of the metallic lattice in carbide ensure stability in the structure. So, the practical interest in WC determines the active elementary investigations of its concentrations through phase diagram and crystal structure.

1.5 Crystal structure and phase diagram of tungsten carbide(s)

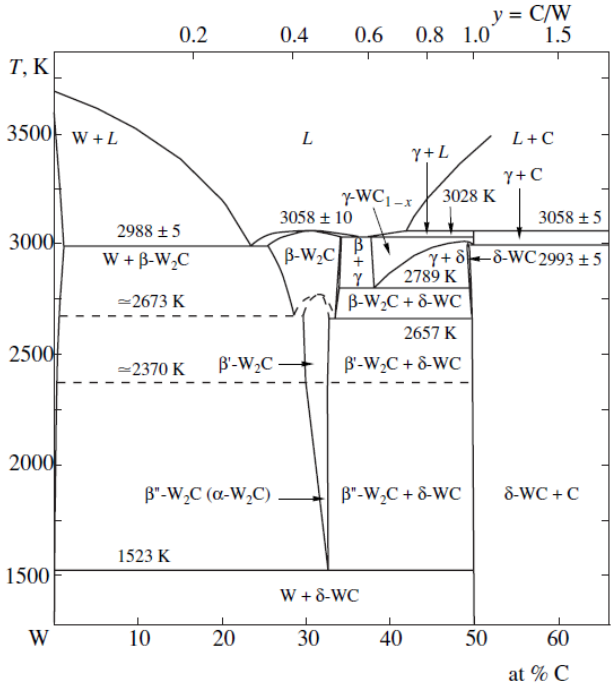

Figure 1.2: Phase diagram of W-C system **[26]**.

The phases of tungsten carbide(s) formed in the W–C systems belong to the group of non-stoichiometric interstitial compounds. The W–C system has mainly three phases, WC_{1-x}, W_2C and WC, having several structural modifications. These phases are stable in certain temperature and concentration ranges (**figure 1.2**). The major phase in the W–C system is the higher tungsten carbide *δ*-WC (WC), which has no homogeneity region, while lower carbide W_2C has relatively wide homogeneity regions. In *δ*-WC (**figure 1.3(a)**) system, both the W and C atoms form simple hexagonal sub-lattices (space group *P-6m2)* with lattice parameters a = 0.2906 nm and c = 0.28375 nm.

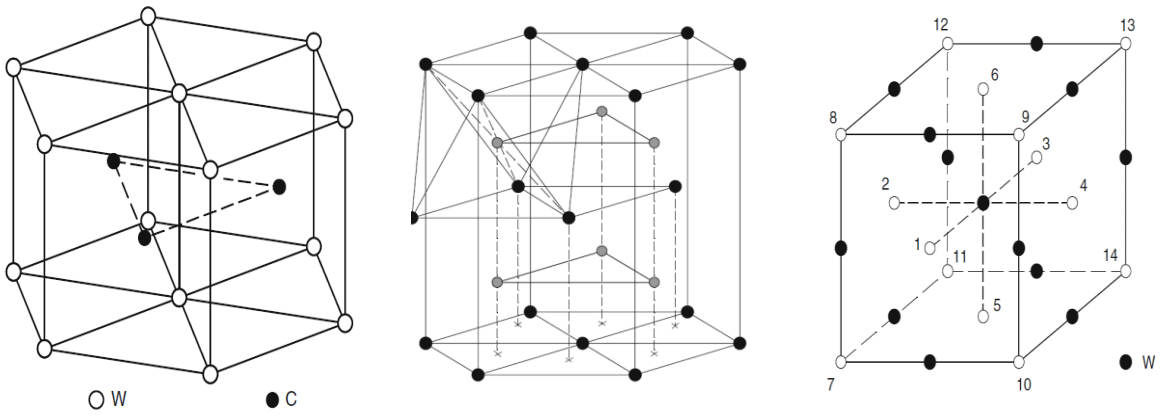

(a) **(b)** **(c)**

Figure 1.3: Crystal structure of **(a)** WC **(b)** W_2C and **(c)** WC_{1-x} **[5]**.

The host-metal atom (tungsten) is arranged in a close-packed structure, and the C-atom occupies specific interstitial sites in that structure as shown in **figure 1.3(a)**. Moreover, the lower tungsten carbide W_2C is designated by three modifications viz low-temperature β''-W_2C, intermediate β'-W_2C and high-temperature β-W_2C, which are also represented as α-, β- and γ-W_2C, respectively **[26]**. In all W_2C types, the W-atoms form hcp structure (space group $P6_3/mmc$), in which one-half of octahedral interstitials are occupied by C-atoms (**figure 1.3(b)**). Depending on the distribution of C-atoms, the lower carbide W_2C can be disordered at a high temperature or ordered at a low temperature. Hence, due to the different types of C-atom distribution, the possibility of the formation of several structural modifications of W_2C exists. In the composition range between the lower tungsten carbide β-W_2C and the higher carbide δ-WC, there exists the cubic phase (space group $Fm\bar{3}m$) WC_{1-x} (**figure 3(c)**) **[26]**.

1.6 Applications of tungsten carbide(s)

Tungsten carbide (WC) has the potential to improve the mechanical properties of cutting tools. Moreover, among hard alloys and refractory carbides specifically in group VI, tungsten carbide (WC) is one of the carbide which has high melting point (2800 °C), high hardness (H_v = 22 GPa), low coefficient of thermal expansion (5.2 × 10^{-6} /K), high thermal conductivity, good wear resistance over as wide range of temperature **[26, 27-29]**. In industries, tungsten carbide (WC) in the form of cemented carbide with nanocrystalline grain

structure after sintering has been well known for its exceptional hardness and wear/erosion resistance.

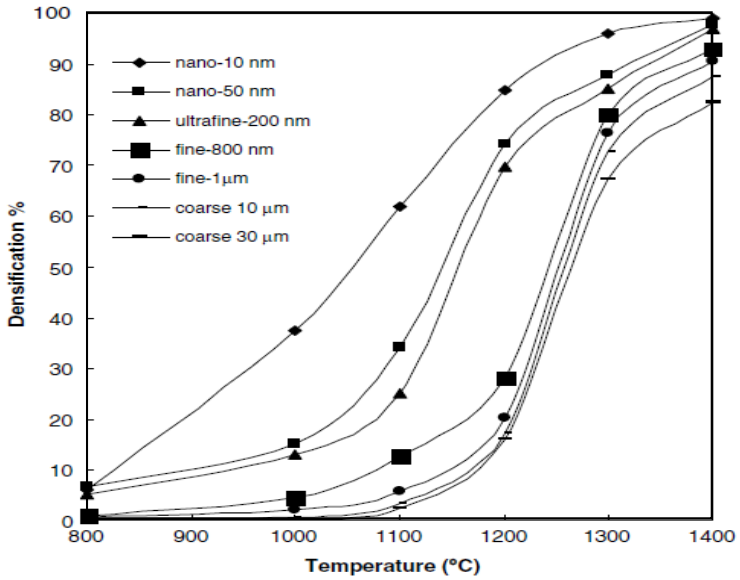

Figure 1.4: The percent of densification of WC–Co as a function of the temperature during continuous heating for various initial particle sizes **[30]**.

Basically cemented carbide is a metal matrix composite which is formed by hard ceramic particles, like WC, into a cobalt metallic (Co) matrix **[31]**. Cemented carbides have a unique combination of good toughness and high hardness within a wide range and used in the most versatile hard materials group for engineering and tool applications. The proportion of carbide phase is normally 70 % to 97 % of the total weight of the composite having grain between 0.2 μm and 20 μm. The hardness which is indirectly depended on the densification of the materials is significantly higher especially from consolidation of nanosized powders as could be expected from conventional powders (**figure 1.4**).

1.6.1 Importance of WC/W_2C in catalysis

Moreover, in recent years, all fuel cells used in electric vehicles require hydrogen (H_2) as a fuel **[32]** which can be generated directly by reforming the methanol, ethanol, butane, or biomass-derived materials. It converts chemical energy of fuel into electrical energy through an electrochemical reaction **[33]** by using a material (Pt) which effectively catalyzes the electrochemical reactions on each electrode surface of fuel cells **[34]**. However, Pt as a catalyst suffers from several drawbacks, including slow kinetics, low efficiency, high cost, and limited lifetime **[35, 36]**. So, in order to commercialize the usage of energy conversion

technologies one of the most important challenges is to either replace or support the high-cost metal catalyst with a high surface area substrate. But due to the continuous advancing development of energy storage and production, the carbon supported Pt catalysts (Pt/C) have been used extensively **[36, 37]**. However, due to the higher operating temperature conditions and cycling conditions of fuel cells carbon support catalysts corrode rapidly **[38, 39]**. Furthermore, due to the carbon oxidation/corrosion Pt catalyst agglomeration occur which tends to degrade the performance significantly **[40]**. Thus, current research is focused upon the development of new non carbon-based support catalyst materials, which have low cost, high performance, stability, and durability.

Among the non-carbon supports candidates; metal carbide (MC) appears to be an important material that shows good electronic conductivity, chemically inert, low cost, tolerance to CO poisoning and are widely used in cutting tools **[15, 41, 42]**. Moreover, the experimental results showed that at ambient conditions MC has been oxidized at around 600 °C **[43, 44]**, which is much higher than the required temperature for operating the low temperature operated fuel cells. In addition, the Pt like catalytic behavior of MC could result in a cooperative way with the metal catalyst, leading to enhancement in the catalyst activity **[45]**.

Moreover, an early study of **Levy and Boudart [45]** on an isoelectronic structure of WC and platinum has focused a considerable amount of attention on the new scope of WC in the research field. The continuous extensive study on WC has made it a good candidate as a catalyst for substitute materials like noble metals (Pt, Pd, Au etc.). For the application of tungsten carbide(s) (WC, W_2C) as a catalyst, it has been observed that it shows high catalytic activity in fuel cells because of its noble metal-like activity, high stability, and CO poisoning tolerance **[46, 47]**. Some research has also revealed that WC can act as excellent anodic and cathodic materials **[46]**. Furthermore, many experiments and calculations indicate that WC/W_2C is utilized as an excellent candidate for fabrication of a high-efficient and stable catalyst system in which small-sized metal nano particles (Pt, Pd, etc.) are deposited onto the surface of WC/W_2C **[14, 46-48]**. Moreover, the synthesis of materials in nano range increased the exposed active sites and improved contact areas with reactants **[49-51]** which results in improvement of the performance. So, WC/W_2C in nano sized can be considered as a promising candidate for next-generation as an electrocatalyst support due to its synergistic effect when combined with platinum nanoparticles (**figure 1.5**). It could lead to Pt/WC electrocatalysts with a higher intrinsic activity **[52]**.

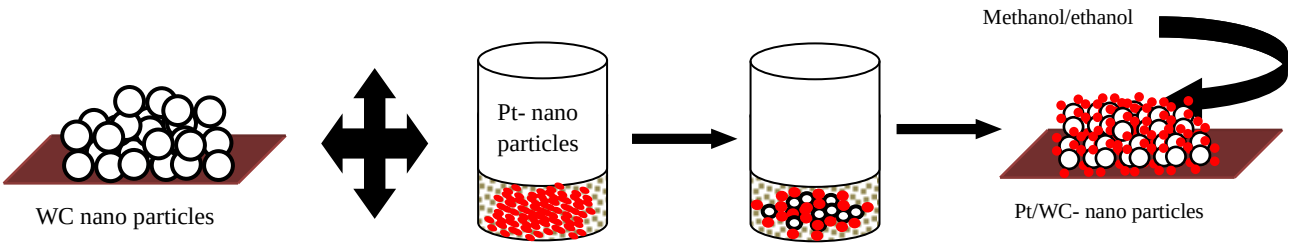

Figure 1.5: Schematic process of platinum nano particles deposition on WC nano particles.

1.7 Synthesis of nano crystalline tungsten carbide(s)

In the era of nanotechnology, when we discuss about nano particles then we usually emphasize on particles with dimensions less than 100 nm on an atomic and molecular scale. However, the significant contributions of nanotechnology have been revealed in the fields of materials science. Many recent important technological breakthroughs can be attributed to the ongoing developments in nanotechnology. There are many ways to synthesize nano materials by suitable processing techniques such as top-down and bottom-up approaches. In the **top-down** approach the nano structured material has been prepared by breaking up the bulk shaped material into the lower size until the microstructure exhibit nanostructure. While in **bottom-up** approach, involve the synthesis of nanocrystalline materials from nanocrystalline particle even at atom, ions or molecules orderly assembled into the desired structure. While several techniques to produce WC nanopowders have been developed, but only a few of them have been proven at the industrial level. Production challenges include economic considerations, properties of powder and its process-ability. The preparation techniques cover a diverse array of processes as is evident from the discussion below:

1.7.1 Mechano-chemical synthesis

In mechanical ball milling process a powder mixture has been placed in the ball mill to produce homogeneous material via high-energy collision from the balls. It was found that this process, named as mechanical alloying could successfully produce fine, uniform dispersions of particles. Hence, their advancement in synthesis techniques has changed the conventional methods to obtain the material which is carried out by high-temperature synthesis. The high-energy ball milling method not only synthesized the materials but also modified the conditions of reactivity of as-milled solids (higher reaction rates, lowering reaction

temperature of milled powders) or inducing the chemical reactions during milling process (mechano-chemistry) **[53]**. Many ceramic powders, alloys as well as composites have been prepared by this method.

Furthermore, high-energy milling is one of the simplest methods to produce WC nano powder by mechanical activated chemistry occurred between tungsten sources and carbon sources during milling process **[54-56]**. The mechanical activation is responsible to enlarge the surface area or to accelerate the reactions by correct mixing of the reagents for enhancing the reactivity of solids. However, the biggest problem associated with this process is to produce nanosized particles which require long processing times, contamination, and high energy expenditures **[53, 57].**

1.7.2 Spray conversion process

Spray conversion process is a continuous and scalable process dedicated for converting liquid streams (slurries, pastes or even melts, suspensions, emulsions, solutions) into dry free-flowing powders. It further enables to produce the particles with controlled size and morphological aspects, which subsequently scaled up to the production at an industrial level. Moreover, the advantages of processing the materials from chemical precursors seem to be a reduction in the production cost of novel materials having homogeneous ultrafine microstructures (nanostructures) and improved properties **[58]**. Furthermore, due to controlling of the processing parameters, the chemical and microstructural uniformity at the nanoscale has been maintained **[59]**. So, the spray conversion process allows the mixing of precursors at the molecular level which yield nano sized materials. However, the problem with this process is that it consists of three-step, which involve the formation of aqueous solution, spray drying to form an amorphous powder, and carburization with carbon containing gases to form pure WC phase **[60]**.

1.7.3 Chemical vapor phase reaction synthesis

In this method, the vapor phase precursors are brought into a hot-wall chamber under the conditions in which instead of the deposition of a film on the wall, nucleation of particles in the vapor phase occur. It is called chemical vapor synthesis or chemical vapor condensation in similar to the chemical vapor deposition (CVD) technique which is used to obtain thin solid films on surfaces. In current approach the nanoparticles has been synthesized by creating conditions where the vapor phase mixture is thermodynamically less stable as

compared to solid material prepared in the nano form **[61]**. Furthermore, in this process a chemical supersatuartion stage is included, which is thermodynamically favorable for the vapor phase molecules to react chemically and form a condensed phase **[61]**. Moreover, the reactions at vapor phase offer the advantages of getting highly pure nanopowders which have good control over the size, shape, and crystal structure as well as easy control of reaction rate. The precursors can be solid or liquid in nature but are introduced into the reactor as a gas. Normally in case of chemical vapor phase reaction synthesis, metal chloride precursors are used due to their lower volatilization temperature **[62]**. But in case of WC nano powder synthesis, different precursors like tungsten hexacarbonyl ($W(CO_6)$) **[63]**, tungsten hexafluoride **[64]**, have also been used. In the next chapter the advancement in the synthesis and electrochemical studies of tungsten carbide(s) has been given.

References:

[1]. S.T Oyama, *The chemistry of transition metal carbides and nitrides*, Blackle Academic & Professional, Glasgow NZ (1996).

[2]. H. Nowotny, *Angew. Chem. Int. Edit.* **11** (1972) 906-915.

[3]. A. I. Gusev, *Phys. Status Solidi B* **163** (1991) 17-54.

[4]. W. F. Chen, J. T. Muckerman, E. Fujit, *Chem. Commun.* **49** (2013) 8896-8909.

[5]. A. S. Kurlov, A. I. Gusev, *Tungsten Carbides: Structure, Properties and Application in Hardmetals*, Springer International Publishing, Switzerland (2013).

[6]. J. G. Chen, *Chem. Rev.* **96** (1996) 1447-1498.

[7]. J. G. Chen, J. Eng, S. P. Kelty, *Catal. Today* **43** (1998) 147-158.

[8]. J. A. Rodriguez, J. Dvorak, T. Jirsak, *J. Phys. Chem. B* **104** (2000) 11515-11521.

[9]. A. Lashtabeg, M. Smart, D. Riley, A. Gillen, J. Drennan, *J. Mater. Sci.* **48** (2013) 258-264.

[10]. J. X. Liu, Y. M. Kan, G. J. Zhang, *J. Am. Ceram. Soc.* **93** (2010) 370-373.

[11]. A. L. Giorgi, E. G. Szklarz, E. K. Storms, A. L. Bowman, B. T. Matthias, *Phys. Rev.* **125** (1962) 837-838.

[12]. R. Teghil, L. D. Alessio, G. De Maria, D. Ferro, *Appl. Surf. Sci.* **86** (1995) 190-195.

[13]. J. Kishino, H. Nomura, S. G. Shin, H. Matsubara, T. Tanase, *Int. J. Refract. Met. H.* **20** (2002) 31-40.

[14]. H. Meng, P. K. Shen, *J. Phys. Chem. B* **109** (2005) 22705-22709.

[15]. G. Jin, B. Xu, H. Wang, Q. Li, S. Wei, *Mater. Lett.* **61** (2007) 2454-2456.

[16]. D. Sivaprahasam, S. B. Chandrasekar, R. Sundaresan, *Int. J. Refract. Met. H.* **25** (2007) 144-152.

[17]. A. S. Kurlov, A. I. Gusev, A. A. Rempel, *Int. J. Refract. Met. H.* **29** (2011) 221-231.

[18]. K. Feng, J. Xiong, L. Sun, H. Fan, X. Zhou, *J. Alloy Compd.* **504** (2010) 277-283.

[19]. H. Meng, P. K. Shen, *Chem. Commun.* (2005) 4408-4410.

[20]. F. Hu, G. Cui, Z. Wei, P. K. Shen, *Electrochem. Commun.* **10** (2008) 1303-1306.

[21]. M. B. Zellner, J. G. Chen, *Catal. Today* **99** (2005) 299-307.

[22]. P. Liu, J. A. Rodriguez, *J. Chem. Phys.* **120** (2004) 5414-5423.

[23]. F. Viñes, C. Sousa, P. Liu, J. A. Rodriguez, F. Illas, *J. Chem. Phys.* **122** (2005) 174709 (1-11).

[24]. Y. Gogotsi, *Nano materials Handbook*, CRC Press, Taylor & Francis Group, Florida, USA (2006).

[25]. J. A. Rodriguez, P. Liu, Y. Takahashi, F. Viñes, L. Feria, E. Florez, K. Nakamura, F. Illas, *Catal. Today* **166** (2011) 2-9.

[26]. A. S. Kurlov, A. I. Gusev, *Inorg. Mater.* **42** (2006) 121-127.

[27]. J. Pirso, S. Letunovitš, M. Viljus, *Wear* **257** (2004) 257-265.

[28]. A. D. Thakur, M. G. Chaudhuri, G. C. Das, R. Dey, M. K. Mitra, S. Mukherjee, *Int. J. Appl. Ceram. Tech.* **11** (2014) 582-589.

[29]. L. Niu, M. Hojamberdiev, Y. Xu, *J. Mater. Process. Tech.* **210** (2010) 1986-1990.

[30]. P. Maheshwari, Z. Z. Fang, H. Y. Sohn, *Int. J. Powder Metall.* **43** (2007) 41-47.

[31]. C. M. Fernandes, A. M. R. Senos, *Int. J. Refract. Met. H.* **29** (2011) 405-418.

[32]. J. M. Ogden, M. M. Steinbugler, T. G. Kreutz, *J. Power Sources* **79** (1999) 143-168.

[33]. C. Ma, C. Xu, M. Shi, G. Song, X. Lang, *J. Power Sources* **242** (2013) 273-279.

[34]. Y. Jiao, Y. Zheng, M. Jaroniecb, S. Z. Qiao, *Chem. Soc. Rev.* **44** (2015) 2060-2086.

[35]. F. Bruijn, *Green Chem.* **7** (2005) 132-150.

[36]. C. Ma, W. Liu, M. Shi, X. Lang, Y. Chu, Z. Chen, D. Zhao, W. Lin, et al., *Electrochim. Acta* **114** (2013) 133-141.

[37]. M. K. Debe, *Nature* **486** (2012) 43-51.

[38]. L. Xiong, L. Zheng, C. Liu, L. Jin, Q. Liu, J. Xu, *J. Electrochem. Soc.* **162** (2015) F468-F473.

[39]. R. Borup, J. Meyers, B. Pivovar, Y. S. Kim, R. Mukundan, N. Garland, D. Myers, M. Wilson, et al., *Chem. Rev.* **107** (2007) 3904-3951.

[40]. H. Tang, Z. Qi, M. Ramani, J. F. Elter, *J. Power Sources* **158** (2006) 1306-1312.

[41]. H. H. Hwu, J. G. Chen, *Chem. Rev.* **105** (2004) 185-212.

[42]. W. Zhu, A. Ignaszak, C. Song, R. Baker, R. Hui, J. Zhang, F. Nan, G. Botton, et al., *Electrochim. Acta* **61** (2012) 198-206.

[43]. C. A. Ribeiro, W. R. de Souza, M. S. Crespi, J. A. G. Neto, F. L. Fertonani, *J. Therm. Anal. Calorim.* **90** (2007) 801-805.

[44]. Z. Yan, H. Meng, P. K. Shen, R. Wang, L. Wang, K. Shi, H. Fu, *J. Mater. Chem.* **22** (2012) 5072-5079.

[45]. R. B. Levy, M. Boudart, *Science* **181** (1973) 547-549.

[46]. J. Yang, Y. Xie, R. Wang, B. Jiang, C. Tian, G. Mu, J. Yin, B. Wang, et al., *ACS Appl. Mater. Interfaces* **5** (2013) 6571-6579.

[47]. F. Harnisch, G. Sievers, U. Schröder, *Appl. Catal. B-Environ.* **89** (2009) 455-458.

[48]. R. Ganesan, J. S. Lee, *Angew. Chem.* **117** (2005) 6715-6718.

[49]. H. Kuhlenbeck, S. Shaikhutdinov, H. J. Freund, *Chem. Rev.* **113** (2013) 3986-4034.

[50]. X. Sun, R. You, X. Hu, J. Mo, R. Xiong, H. Ji, X. Li, S. Cai, et al., *RSC Adv.* **5** (2015) 35524-35534.
[51]. Z. Li, Y. Kathiraser, S. Kawi, *ChemCatChem.* **7** (2015) 160-168.
[52]. Y. Liu, W. E. Mustain, *Int. J. Hydrogen Energ.* **37** (2012) 8929-8938.
[53]. C. Suryanarayana, *Prog. Mater. Sci.* **46** (2001) 1-184..
[54]. S. Bolokang, C. Banganayi, M. Phasha, *Int. J. Refract. Met. H.* **28** (2010) 211-216.
[55]. M. Razavi, M. R. Rahimipour, R. Y. Rad, *J. Alloy Compd.* **509** (2011) 6683-6688.
[56]. M. Sherif El-Eskandarany, *J. Alloy Compd.* **296** (2000) 175-182.
[57]. R. Uribe, C. Baudín, L. Mazerolles, D. Michel, *J. Mater. Sci.* 36 (2001) 5105-5113.
[58]. B. H. Kear, L. E. McCandlish, Nanostruct. Mater. **3** (1993) 19-30.
[59]. L. E. Mcchandlish, B. H. Kear, S. J. Bhatia, US patent 5352269 (19940.
[60]. G. E. Spriggs, *Int. J. Refract. Met. H.* **13** (1995) 241-255.
[61]. M. T. Swihart, *Curr. Opin. Colloid. In.* **8** (2003) 127–133.
[62]. Z. Z. Fang, X. Wang, T. Ryu, K. S. Hwang, H. Y. Sohn, *Int. J. Refract. Met. H.* **27** (2009) 288-299.
[63]. J. C. Kim, B. K. Kim, *Scripta Mater.* **50** (2004) 969-972.
[64]. M. Fitzsimmons, V. K. Sarin, *Surf. Coat. Tech.* **76-77** (1995) 250-255.

CHAPTER 2

LITERATURE REVIEW

Overview

In this chapter, the works for getting different allotropes of tungsten carbide (WC/W_2C) nano powders by different methods are presented. The entire literature describes the details of WC/W_2C nano powders synthesis from different tungsten precursors using different carbon source and reducing agents. The literature work describes all the efforts made by different group to get single phase of carbide(s) (WC/W_2C) at nano scale giving details of the synthesis conditions. The last part of the literature deals with electrochemical activity of the synthesized nanocrystalline carbide powders for its use as electrode in fuel cell applications. Apart from this, different approach for designing varieties of catalysts with improved efficiency, reliability and interaction with Pt and Pd as supporting materials has also been reviewed in this chapter.

With increased applications of WC/W_2C nanopowders, efforts are being made to prepare them at lower cost with ease of synthesis procedure. However, the applications of obtained product mainly depend upon the process and hence the reactions involved in the process by which carbide(s) is produced (carburization by liquid hydrocarbon, solid carbon, and synthesis temperature). Hence, the materials scientists are continuously working to improve the properties and performance of such materials which can be achieved by significant improvement through modifying the surface via conventional thermal, mechanical, and thermo-mechanical processing methods associated with high end applications.

2.1 Synthesis of Tungsten Carbide Nanopowder (WC/W_2C)

2.1.1 Direct carburization reactions

In this process, the metallic powders react with solid carbon in the presence of protective atmosphere (H_2 or vacuum). Such kinds of reactions are normally affected by the temperature, pressure, time and the state of initial ingredients. Moreover, depending upon the operating conditions the carbon content in the final product obtained by this method may vary significantly. Commercially tungsten carbide (WC) was also produced by direct reaction between tungsten (W) and carbon (C) at very high temperatures, typically 1400-1600 °C under vacuum or inert atmosphere **[1]**. **Koc and Kodambaka [2]** have also followed the same process of carburization using pure tungsten oxide (WO_3) as tungsten (W) source and established a reaction path for getting pure WC. In order to reduce the operating temperature, two steps method was followed by them. Firstly, the oxide powders were coated with carbon by cracking of propylene (C_3H_6) gas followed by mixing with a substantial amount of carbon black. Finally the mixture was treated at temperatures in the range of 600-1400 °C for 2 h in the presence of Ar or 10% H_2-Ar atmosphere. This process led to formation of WC directly without the formation of W_2C at higher temperature.

Hatano et al. [3] studied the solid-state reaction between W and amorphous carbon (AC) at 700, 800 and 900 °C and concluded that rate of nucleation and growth of W_2C is significantly higher than those of WC at these temperatures. **Oliveira et al. [4, 5]** studied the formation of WC and its stability by using graphite and W powders as the precursor in the controlled mole ratio in a solar furnace. In this process, synthesis temperature was achieved from the ambient temperature upto 1600 °C or 1900 °C quickly. **Li et al. [6]** used WO_3 as tungsten source and cyanamide (CN_2H_2) as a carbon source. The WC nano powder with size ~6 nm have been obtained by heating the mixture of starting precursor in molar ratio 10:1 at

1150 °C for 30 min. **Jin et al. [7]** have obtained WC nano powder by heating ammonium metatungstate (AMT) and glucose ($C_6H_{12}O_6$) at 1000 °C and discussed the formation of different phases and their microstructure during the synthesis of WC nanopowders.

Due to the process limitations of consuming higher energy and higher time reaction phenomenon for getting WC nano powder by these methods, mechanical alloying (MA) also called mechano-chemical route has been employed for the production of nano-structured WC.

2.1.2 Mechano-chemical synthesis

Mechano-chemical synthesis is a technique used to produce homogeneous material from blending of elemental powder mixtures. The powders obtained by this method have particles of uniform shape and narrow size distribution in the nano meter range **[8]**. **Le Caër et al. [9]** have employed the synthesis of carbide systems by mechano-chemical route. Subsequently, **Matteazzi and Le Caër [10]** have reported the effect of milling on atomic mixture of W and C (50:50) powders and obtained powder of particle size of the order of 20 nm. However, because of the contamination from milling media, they were unable to draw any major conclusion. **Wang et al. [11]** synthesized WC nano powder directly by milling the mixture of W and C powder in vacuum up to milling time 310 h. The tendency to obtain pure single phase WC was enhanced by subsequent heating the milled materials at 1000 °C in vacuum for 1 h.

Tan et al. [12] modified the classical high-energy milling process by the reduction of WO_3 using magnesium (Mg) containing graphite mixtures. The graphite is used as carbon source for carbide formation while the Mg as catalyst to enhance the reactive synthesis. **El-Eskandarany [13]** prepared nano crystalline WC powder of 7 nm size by ball-milling of WO_3, Mg, and C at room temperature in 48 h. **El-Eskandarany et al. [14]** have also obtained WC nanopowders of particle size 70-90 nm by high-energy ball milling of W and C powders after 71 h milling time, which further decreased to 5 nm by increasing the milling time upto 120 h. The obtained powder has better morphological features, such as homogeneous shape (spherical-like morphology) with fine and smooth surface and uniform size.

Liu et al. [15] have done mechanical alloying (MA) of new carbon source fullerene with W for 10 h and concluded that the heat of formation for carbide plays an important role in the MA process which act as a driving force for reaction to get WC (-20.64 kJ/mol). **Zhang et al. [16]** prepared nano WC powder by taking W and graphite powder with paraffin wax based macromolecule compound via wet milling for 12 h in a multi-component ball-milling organic

medium. The liquid medium in the colloidal slurry was evaporated under vacuum. Further, the carbon coated precursor was carburized in a muffle furnace with molybdenum wire as heating element at 1000 °C for 10 h under hydrogen. The final obtained powder (WC) by this approach has BET specific surface area 5.86 g/cm^3 and particle size 65.2 nm.

Ma and Zhu [17] have done the solid-state carbothermic reduction of WO_3 to obtain WC nanoparticles by calcining mechanically activated mixtures of WO_3 and graphite powder at 1215 °C under vacuum. They observed that the final product WC formed in this process via intermediates, including Magneli phases ($WO_{2.72}$ and WO_2) and W. **Bolokang et al. [18]** studied the effect of carbon amount and milling parameters on the synthesis of WC. According to them, higher carbon content takes longer milling time to form WC. Moreover, W_2C phase was also observed with higher carbon content when milled at low speed and lower ball-to-powder ratio (BPR). Consequently, in order to get carbon-deficient composition milling was done for a short time period. **Razavi et al. [19]** obtained single phase WC nano powder by milling W and C along with commercial WC powder (particle size of 1 μm) in a planetary ball mill for 100 h.

Yang et al. [20] followed a new novel method for synthesizing ceramic powders in molten salt. Unlike a traditional mechanochemical process, this is based on mechanical alloying followed by chemical reaction in liquid phase (molten salt) at 1000 °C. They have synthesized W_2C and WC powder successfully by this method. Although the milling techniques can produce powders at nano scale but contamination, long durations of processing and high-energy consumption problems are also associated with this process.

2.1.3 Spray conversion process

The spray conversion process is an advance technology for producing nanosized WC powder and has been adopted at the industrial level. Spray conversion processing has appeared as the most versatile and reproducible process. This process is normally applied for the production of nano sized composite powders. The phase uniformity is maintained in the spray drying process which gives a large, porous and flow able precursor powder. In this process the aqueous solution of precursors are subjected to spray drying. This process leads to the formation of amorphous powder which is further carburized in the presence of carbon containing gases to obtain pure WC **[21, 22]**. **Gao et al. [23]** have reported the formation of nano grained WC through this method by controlling simultaneous reduction and carburization reaction directly from the ammonium metatungstate (AMT) and gas mixture

(H_2 + CO). **Seegopaul et al. [24]** have proposed that the carbide formation is possible through a substitution of carbon for oxygen in the matrix. The authors also demonstrated a recycling process using scrap materials which is further oxidized. This is then further dissolved in a solution of NaOH and spray dried to form a precursor compound. As a carbon source, a compound such as citric acid ($C_6H_8O_7$) has been added to the prepared solution before the spray drying for the formation of WC. Furthermore, the obtained powder formed from the spray dried solution is calcined and carburized at 775 °C to form WC nano powder. **Kim et al. [25]** followed the thermochemical process by taking AMT as W source and introduced an additional mechanical milling treatment of the spray dried powder in which carbon is added intentionally to support the formation of carburizing phase. Furthermore, the milled powder is converted into nano powder by gas phase reduction and carburization at about 800 °C for 24 h.

Moreover, another change in the spray conversion process has been done by **Zhang et al. [26]**. They involve the co-precipitation of cobalt (Co) with salts of tungsten such as ammonium paratungstate (APT). The hard metal constituents are mixed at the atomic level, followed by hydrogen reduction and further carburize in the presence of different mixture of CO and CO_2. The average size of particle in the prepared powder reported was of the order of 20–50 nm. But the major problem associated with this method is the formation of large agglomerates.

2.1.4 Chemical vapor phase reaction synthesis

The chemical vapor phase reaction technique also known as chemical vapor deposition (CVD) is a process where a solid material is deposited from a vapor occurring due to a chemical reaction on or in the region of a normally heated substrate surface. The solid material can be obtained in the form of coating, powder, or as single crystals after looking the demand of WC used under severe conditions (at high temperature, high pressure and in corrosive media).

Hojo et al. [27] synthesized WC and W_2C powders by vapor phase method using WCl_6-CH_4-H_2 system at 1000–1400 °C. According to them, the particle size and yield of WC was affected by the different reaction mechanism involved in the process. The reductions at lower temperature followed by carburization at higher temperature show better result as compared to simultaneous reduction and carburization occurring at higher temperature. However, the low temperature CVD process has also been reported by authors **[28, 29].** In this process, the

coating of WC has been done onto the substrates by hydrogen reduction of tungsten hexafluoride (WF_6) in the presence of dimethyl ether. The coating comprises of mixture of the W and WC which improved the erosion property of the mechanical component. **Won et al. [30]** synthesized nanosized WC powder in a horizontal tube reactor by the CVD technique using WCl_6–C_2H_2–H_2 mixtures. The obtained product was a mixture of α-WC and β-W_2C. According to them, the particle size of product increased with the increase in volatilizer temperature of WCl_6 and decreased with the increase in H_2 flow rate. Particles of wide size range of 100-1000 nm were obtained in this work.

Fitzsimmons and Sarin [31] have studied the thermodynamics and kinetics of a desired reaction for two different coating systems WCl_6-CH_4-H_2-Ar and WF_6-CH_4-H_2-Ar. The authors have found that both systems exhibit an increasing WC phase region at lower temperature and observed the requirement of lower partial pressure of CH_4 for WF_6 than WCl_6 to produce WC. **Tang et al. [32]** reported the synthesis of WC nano powder by the vapor phase reaction of WCl_6–C_3H_8–H_2 mixtures in a downstream tube reactor. While for getting the complete transformation into WC phase, an excess amount of C_3H_8 and temperatures above 1400 °C were required. It further required a post-treatment of obtained powder by hydrogen for 1 h at 1000 °C, to remove an excess amount of carbon in the product. **Medeiros et al. [33]** synthesized very fine WC crystallites by using APT and tungsten blue oxide (TBO) as the W sources and mixture of gas CH_4 and H_2 as the carbon source and reducer respectively at temperatures ~850 °C in 2 h.

Sohn et al. [34] followed the chemical vapor synthesis (CVS) process for the production of WC nanopowder of size less than 30 nm by using WCl_6 as the precursors with H_2 and CH_4 as the reducing and carburizing agents, respectively. They observed that the formation of WC is highly dependent on the reaction temperature as well as the ratio of H_2/CH_4. However, in the absence of sufficient reaction temperature or CH_4 concentration, W_2C or even W was formed instead of WC. **Yang et al. [35]** have deposited nanocrystalline WC thin films on quartz substrates using hot-filament chemical vapor deposition (HFCVD) technique. The authors have observed the effect of temperature on the particle size as well as phase formation using Raman as well as XRD analysis.

Medeiros et al. [36] have reported the carburization of APT by CH_4 directly into WC at 800 °C in short times. The obtained carbide powder has specific surface area around 35 m^2/g. The authors have found that the overall reaction rate (reduction and carburization) can be increased by increasing temperature, gas flow, amount of CH_4 in the mixture and powder

fineness with decreasing the powder charge. This method still involves the difficulty of excess carbon coating on the produced particle which can be removed by the post-treatment with hydrogen. They have also observed that delicate balance is required between the simultaneous reduction and carburization for the synthesis of single phase of WC, when oxide is used as precursor. **Cetinkaya and Eroglu [37]** have initially obtained W powders from WO_3 by H_2 treatment. The reduced W powder was carburized at 627-827 °C in the presence of pure Ar and H_2-diluted CH_4 atmospheres to get single phase WC powder of particles size 40–65 nm in a relatively short time.

2.1.5 Thermal plasma processing

After successively synthesis of WC by CVD processing technique, a plasma processing technique has also been applied for the synthesis of nano carbide powder by **Tong and Reddy [38]**. Thermal plasma processing (TPP) provides a very high processing temperature, at which metal oxides in monatomic gaseous state and very high quenching rates strongly suppresses the growth of product for the production of nano-powders **[38]**. **Ryu et al. [39]** followed the TPP technique to obtain WC nano powder. The authors have used WCl_6 as the W source with CH_4 and H_2 gases as carburizing and reducing agent, respectively. The final product obtained by TPP technique contained the mixture of WC_{1-x} powder and small amount of WC and/or W_2C phase. The particle size of WC_{1-x} was affected by plasma torch power, the plasma gas flow rate, and the secondary plasma gas (H_2). Moreover, the obtained WC_{1-x} and W_2C phases were converted to WC phase while the excess carbon present in the product was completely removed by the hydrogen post-treatment at 900 °C. The particle size obtained by this method was found to be less than 40 nm. However, the formation of pure-phase WC powder with control amount of free carbon remained as problem which yet required to be overcome.

2.1.6 Combustion Synthesis/ Self-propagating High-temperature Synthesis

Since, the formation of carbides requires high heat of formation, which is found to be low (ΔH= -9.69 kcal/mol) in case of reaction between W and C mixture. So, the authors **[40, 41]** have proposed the combustion synthesis (CS) or self-propagating high-temperature synthesis (SHS) which exhibit high energy efficiency and attractive technology for the synthesis of carbides at nano scale. **Nersisyan et al. [42]** followed the CS technique for the production of nanostructured WC from WO_3+Mg+C+sodium salts (NaCl, Na_2CO_3) systems. Consecutively, **Nersisyan et al. [43]** obtained the nanostructured WC from WO_3 + NaN_3 + C system in the

presence of Ar gas by the same technique in which NaN_3 act as a reducing agent. In this system, the obtained powder has the particle size less than 100 nm. In another approach of CS, the reduction and carburization of WO_3 was done with Mg and mixture of carbon black with ammonium carbonate respectively. The WC nano powder obtained by this system has particle size in the range of 200 nm **[44]**.

Won et al. [45] synthesized WC nano powder having size less than 100 nm from WO_3 + 3 Mg + C system with sodium halides and carbonate. The investigations proved that small amount of carbon-containing compounds (ammonium carbonate) significantly enhance the combustion synthesis process to activate the carburization of W during the reaction. One of the approach has also been proposed by **Wang et al. [46]** in which hexagonal tungsten carbide (*h*-WC) was synthesized by heating the tungsten-sodium and supercritical carbon dioxide at moderate temperature 600 °C. The authors have found that the synthesis of WC is taken by the transformation of CO_2 into graphite by Na. While tungsten has been transformed into tungsten oxide, which carburized further by the *in-situ* formed graphite and transformed into WC.

2.1.7 Thermo-chemical process

This process consists of chemical conversion of initial ingredients into final product via, heat and pressures which helps to enhance the chemical reactions by breaking down the constituent parts. This process provides control over the size and shape of the finally obtained particle. **Reddy et al. [47]** have also adopted this method to obtain the nanostructured WC and observed the influence of precursor structure on nanostructured WC phase during reduction and carburization. The authors have concluded that the chemically obtained WO_3 after reacting with amorphous C at 1000 °C provide fraction of amorphous WC. While the commercial WO_3 after reacting with graphite as well as amorphous carbon provides W_2C and mixture of WC/W_2C phases, respectively. The average crystallite size of pure WC estimated from XRD peak profile was about 38 nm. Consecutively, the stability of nanostructured WC phases during carburization of chemically obtained WO_3 was studied by **Reddy et al. [48]**. They have given the sequence of conversion of carburization $WO_3 \rightarrow W \rightarrow WC_{1-x} \rightarrow W_2C \rightarrow$ WC. **Aravinth et al. [49]** synthesized *h*-WC nano powder by carburization of tungsten /tungsten oxide/non-stoichiometric tungsten oxide particles which was obtained from a wire explosion process with multi walled carbon nano tubes (MWCNT). The obtained WC particles are of spherical shape having geometric mean size about 19 nm.

In all the above mentioned process, the cost of production for the synthesis of carbide at nano scale is very high due to the involvement of multi-steps and high temperature. Hence, in order to enhance the reaction kinetics of carburization, the autoclave synthesis route has been employed by using Mg as reducing agent **[50]**. This is a chemically co-reduction route for the synthesis of nanostructures at relatively lower temperature (~600 °C) in which hydrocarbons and Mg are used as carbon source and reducing agent, respectively in autoclave. **Guo et al. [51]** reported the synthesis of WC nano crystal via solvothermal reaction between WO_3, Mg and anhydrous ethanol (CH_3CH_2OH) in autoclave at 600 °C for 15 h. The obtained powder consists of particle size in range between 100 to 200 nm. **Ma et al. [52]** have done the hydrothermal treatment of AMT and ammonium carbonate mixture at different temperature, followed by heating at 800 °C to obtain WC having mesopores structure. Since, the nascent carbon produced during the reaction had good reaction activity as compared to carbon black, so **Ma and Du [53]** synthesized nanocrystalline *h*-WC via co-reduction-carbonization mechanism in an autoclave at 600 °C. In this process, WCl_6 was used as W source, sodium carbonate (Na_2CO_3) and Mg were used as carbon source and reductant, respectively. The particle size of the obtained powder was about 20 nm with specific surface area of the order 14.5 m^2/g. The powder obtained from this process had good thermal stability and oxidation resistance below 500 °C in air.

Kumar et al. [54, 55] have presented the work on the synthesis of WC nano particles via solvothermal route by taking WO_3, Mg and two different carbon source (acetone and ethanol). The authors have found the conversion of WO_3 into WC and maximum yield at 800 °C in time 20 h by taking 36 mL acetone. Additionally, **Kumar et al. [56]** also reported the work on the formation of WC nano particles directly from wolframite ore with and without ball milling the W source and taking three different carbon source (methanol, ethanol, acetone) in autoclave in the presence of Mg as reductant. The authors have found WC nano powder by heating the mixture at 800 °C for 20 h in the presence of suitable solvent acetone. Moreover, the possibility of WC formation at lower synthesis time (10 h, 15 h and 20 h) increased by using milled W source in the autoclave for 36 mL acetone. The average size of obtained WC nano particle is of the order of 13 nm. **Singh and Pandey [57]** have reduced the multistep of the processing for getting WC directly from scheelite ore by milling it for 50 h. The milled ore was put in autoclave with activated charcoal and Mg. The mixture was heated at 800 °C for 20 h and found WC nano powder after removing impurities CaO and MgO.

2.2 Electrochemical study

Because of the diminishing of limited natural resources, energy crisis has become the major global concern. Therefore, extensive research has been pursued for the development of alternative energy storage and conversion systems. In this respect, the oxygen-reduction reaction (ORR)/ hydrogen-evolution reaction (HER) and hydrogen oxidation reaction (HOR)/ oxygen evolution reaction (OER) that occur at cathode and anode, respectively have become the important reactions in the field of energy conversion system **[58-62]**. These reactions are playing important role in the conversion of the chemical energy to electrical energy **[63]**. But, all these reactions are slow in nature which limits the performance of the fuel cell system and traditionally used precious metals such as platinum (Pt) and palladium (Pd) **[64]**. The high cost and shortage of the costly noble metals put limitations on the large-scale execution of these materials. Thus a need is felt to develop catalysts which can speed up the kinetics of these reactions to reach a usable level in fuel cells by either replacing them or using as support to the noble metals. Hence after the attributing of Pt like catalytic behavior of WC in 1973 by **Levy and Boudart [65]**; WC supported noble metals (Pt, Pd) catalysts are widely used for electrochemical reactions. Furthermore, depending upon its physical properties, electrochemical stability, operating potential range and requirements, scientists are using it as electrode (cathode/anode) electrocatalyst for different reactions which is discussed below:

2.2.1 Oxygen-reduction reaction (ORR)

Oxygen-reduction reaction (ORR) is a normal cathodic process to remove the electrolysis produced oxygen via oxygen reduction activity which results to enhance the performance of fuel cell and becomes the important studies of electrode reactions in different media. However, due to sluggish nature of ORR on the cathode side, it restricts the accessibility of fuel cells usage. In order to enhance it **Meng and Shen [66]** studied the Pt modified WC nano crystals as cathode electro catalyst towards ORR. The authors have also observed the influence of the concentration of methanol on activity along with shifting of onset potential for ORR towards the positive side on Pt-W_2C/C as compared to Pt/C.

Nie et al. [67] have analyzed the performance of Pt-WC/C electrocatalyst for ORR in acidic media. The results revealed the shifting of onset potential for ORR towards more positive as compared to commercial Pt/C. **Nie et al. [68]** have studied the effect of nano bimetallic (AuPd-WC/C) system on ORR. The results show that AuPd-WC/C has 70 mV higher onsets potential for ORR as compared to Pt/C with higher current density in acidic

solution. **Chhina et al. [69, 70]** have synthesized high surface area WC and performed its electrochemical testing by opting specific amount of Pt deposition for ORR. The reports confirmed that Pt/WC catalyst is electrochemically stable up to higher oxidation cycle which seems to be suitable as cathode catalyst in PEMFC in long term. **Yan et al. [71]** have loaded WC nano particles on graphitic carbon (WC/GC) to improve the ORR and found improvement in electrocatalytic activity in terms of higher kinetic current as compared to Pt/C. **Meng et al. [72]** have studied the ORR of W_2C nanocrystals on carbon (W_2C/C) and Pt deposited W_2C/C (Pt-W_2C/C) composite as electrocatalysts prepared by the intermittent microwave heating (IMH) method in the acidic media. The results revealed that Pt-W_2C/C proved to be more active for ORR by observing 100 mV shifting towards positive as compared to Pt/C. **Elezović et al. [73]** have studied the results of surface carbon free WC for ORR with and without Pt, in alkaline solution (NaOH). The authors have observed 150 mV shifting of onset potential towards positive side for ORR which is better than Pt/Vulcan.

The recently interest is to improve the catalytic activity of catalysts by obtaining mesoporous structure which can provide more active sites. **Zhu et al. [74]** have noticed the greater ORR activity of Pt deposited mesoporous modified WC (Pt-WC/C) with higher current density as compared to unmodified mesoporous carbon support. **Zhu et al. [75]** have prepared the nanocrystalline WC with a high surface area containing minimum free carbon by polymer route and observed its electrochemical stability. They have observed that this material exhibited low electrochemical stability in acidic media when subjected to potential cycling at potentials larger than 0.7 V *vs.* RHE, due to the electrooxidation of WC. They have also analyzed the ORR of 20 wt% of Pt supported on WC which was significantly lower than commercial Pt supported on carbon. **Ko et al. [76]** have reported the synthesis of mesoporous WC by hydrothermal method from W_2N at different reaction temperatures. The sample obtained at 900 °C exhibited better ORR activity in alkaline solution even after 2000 cycles which can be improved by depositing the Pd nanoparticles.

2.2.2 Hydrogen-evolution reaction (HER)

Hydrogen-evolution reaction (HER) is a cathodic process to generate the hydrogen for the minimization of energy consumption by efficient and abundant electrocatalyst. Insipte of numerous efforts and significant technological interest, it is still a challenge to develop a low cost hydrogen electrode catalyst with high activity. The efforts made in this direction to

develop a hybrid material made of Pt/Pd supported on WC as a high performance electrocatalyst for HER is described below:

Wu et al. [77] have prepared (PdPt-WC/C) as cathode electrocatalyst to determine the better performance in HER activity for the production of hydrogen as fuel in acidic media. They have observed the shifting of the onset potential on positive side with higher current density. The authors have also discussed the kinetic of HER by changing the concentration of H_2SO_4 and observed improvement in HER with the increasing sulfuric acid concentration. **Rees et al. [78]** have studied the electrocatalytic activity of WC obtained by microwave carburization method and also analyzed the effect of KCl, Ni(II), Fe(II) and Mn(II) reactants used during synthesis on the HER activity. **Hsu et al. [79]** have deposited mono layer (ML) of Pt on WC by physical vapour deposition (PVD) technique to reduce the amount of Pt and cost of prepared electrocatalyst. The prepared Pt–WC core–shell powder catalysts prepared by minimum amount of Pt (~0.85 wt%) produced HER activity better than 10 wt% Pt deposited C (Pt/C) and it even remained stable under HER conditions. **Yan et al. [80]** have reported the results of novel ternary composite of MoS_2, WC and reduced graphene oxide (RGO) (MoS_2/WC/RGO) for HER activity. In this combination, WC proved as an effective co-catalytic support for electrochemical water splitting.

Kelly et al. [81] have synthesized Pd supported WC (Pd/WC) to reduce the cost of electro catalysts for HER. The results of obtained catalysts (Pd/WC) exhibited two orders of magnitude increment in current density at overpotential of -0.1 V relative to the unmodified carbides. **Kimmel et al. [82]** have studied the effect of surface carbon on electrocatalytic activity of WC and Pt modified WC (Pt/WC) thin film through HER analysis. They have found that the HER activity of WC was relatively not affected by very small amounts of surface carbon but decreased when several MLs of surface carbon was present. On the other hand, Pt/WC without surface carbon was found to have slightly higher HER activity as compared to Pt deposited on WC with surface carbon. **García et al. [83]** have compared the electrochemical activities of different transition metal (W, Ta, Nb, Cr, Mo) carbides electrodes towards HER in concentrated phosphoric acid in a temperature range from 80 to 170 °C. The authors have observed that among all the studied carbides, WC showed the highest HER activity throughout the studied temperature range.

Nikiforov et al. [84] have investigated the electrochemical performance of WC at temperature up to 150 °C. The results proved that the HER activity of WC increases significantly with temperature and this effect is more pronounced than that of Pt. **Harnisch et**

al. [85] have analyzed the catalysts which contain different fractions of WC, W_2C, W and WO_2 and reported that the performance of the catalyst is proportional to the content of WC, whereas other impurity phase (W_2C, W and WO_2) play minor role. The relationship between WC content and electrocatalytic activity indicates that hydrogen evolution through HER seems to relate to surface sites preferentially formed on WC. **Ham et al. [86]** have prepared W_2C microsphere by carburization of AMT and resorcinol-formaldehyde resin via polymer-induced carburization method and obtained microspheres having high surface area. The prepared material has been tested for HER activity with 7.5 wt% of Pt and observed activity 2.3-3.2 times higher than Pt/C catalyst. **Zheng et al. [87]** have prepared nano crystalline WC thin film on Ni substrate by plasma enhanced CVD technique to investigate the electrocatalytic properties for HOR in alkaline solution (KOH). The results shows that the hydrogen evolution exchange current density ($4.02-4.22 \times 10^{-4}$ A/cm^2) have been obtained for WC/Ni electrode which is comparable to Pt electrode.

2.2.3 Hydrogen oxidation reaction (HOR)

Hydrogen oxidation reaction (HOR) is an anodic process to oxidize the produced hydrogen during HER into H_2O in different electrochemical environment. **Yang and Wang [88]** have proposed nanoscale WC as the anode catalyst for HOR. The authors have obtained high current density of 0.9 A/cm^2 in the presence of hydrogen/air in polymer electrolyte fuel cell (PEMFC). **Lu et al. [89]** followed the scanning electrochemical microscopy (SECM) for Pt–Ru system to investigate the response of HOR and CO tolerance in acidic electrolyte after the addition of WC. The results show that the optimum composition of ternary system $Pt_{25\pm5}Ru_{5\pm5}WC_{70\pm5}$ attributes better HOR activity as well as CO tolerance.

Hara et al. [90] have compared the HOR for the different phases of WC (α-WC>β-WC_{1-x}>β-W_2C) having high surface area obtained by carburization of nitride and sulfide, prepared from WO_3. The study on different WC phases shows better response of HOR as compared to direct carburized powder. Moreover, a small amount of Pt loading on WC phase obtained from W_2N and WS_2 attribute better utilization of Pt for the HOR. Surface chemistry of WC nano powder have been studied by **Glibin et al. [91].** After considering the fact that non-stoichiometric oxides serve as active sites for catalytic activity **[92]**, the authors have also confirmed that after insertion of oxygen atoms in the WC lattice the anodic range for HOR has been widened.

2.2.4 Methanol /Ethanol oxidation reaction ((MOR/EOR)

Since, the current strategy in accessing fuel cells has been adopted because of their high efficiency and clean energy production (no formation of SO_2, N_xO_x) **[93]**. This has been accomplished by the oxidation of liquid fuels (methanol and ethanol) at anode in fuel cells. However, the critical obstacles including lower electrocatalytic activity of anode material and high cost of Pt electrocatalysts inhibit their usage in fuel cells. So, tungsten carbide as an alternative has also been studied and proposed as an anode catalyst that allows not only the oxidation of hydrogen (HOR) but also of small molecular organic compounds such as methanol and ethanol. **Huang et al. [94]** have analyzed the ORR electrocatalytic performance of novel nanocomposites of spherical graphite-carbon (GC) encased WC (GC-WC) in alkaline medium. The results show that GC-WC has a considerable performance for ORR in the view of activity, stability and methanol tolerance and can be used as proper supports for noble-metal based ORR catalysts in alkaline fuel cell. **Zheng et al. [95]** have verified that ordered mesoporous carbon modified WC (OMC/WC) show higher activity for methanol oxidation (MOR) which is very close to Pt-based material.

Bukola et al. [96] studied the cobalt (Co) and nitrogen (N) co-doped WC catalyst for ORR and HER activity in 0.1 M KOH. The results confirmed that after the doping of Co and N, the prepared electrocatalysts exhibits good durability for both cathodic processes with excellent tolerance towards methanol oxidation. **Zhong et al. [97]** have also prepared carbon-encapsulated cobalt-WC (CoWC@C) composite, which show ORR activity comparable to Pt/C associated with higher current density response. The catalyst also showed better tolerance to CO in the presence of methanol. Moreover, due to the unique structural effect of carbon nano tube (CNT), PtWC/MWCNT as an electrocatalyst has also been analyzed for electrochemical applications in acidic media **[98, 99]**. The authors have found lower onset potential for MOR in PtWC/MCNT system which confirmed its superior electrochemical performance as compared to PtRu/C and Pt/C. **Bosco et al. [100]** have prepared three-dimensionally ordered macroporous (3DOM) WC and compared the catalytic activity of modified and unmodified 3DOM WC materials. The results demonstrated low methanol electro-oxidation activity and significant hydrogen adsorption/desorption activity of unmodified 3DOM WC. They have found substantial activity for methanol oxidation as compared to Pt supported on activated carbon after the modification of 3DOM WC with Pt.

Weigert et al. [101] studied WC as potential replacement of Pt for MOR. The results of this study have revealed that due to strong interaction between Pt and the WC substrate, no

agglomeration of Pt particles occur which helps to maintain the electrochemical activity of catalyst. **Mellinger et al. [102]** modified the WC nano structured by Pd (Pd/WC) for its use as catalyst in MOR. The studies showed that the WC surface was very active to produce a methoxy intermediate after the cleavage of the O−H bond. Although WC was observed to be less active for the C−H bond scission, but the enhancement in the scission of C−H bonds of methoxy by Pd/WC, attributes a synergistic effect of Pd-modified WC as electrocatalysts for methanol decomposition. **Zellner et al. [103]** have examined the electrochemical stability of WC and W_2C films prepared by PVD techniques. The results of the studies attributes that W_2C has been converted into W_xO_y species; while, WC film remains stable at the anode potential below 0.6 V in the electrochemical environment. The reaction of methanol decomposition has also been investigated on Pt modified WC films, which shows a promoting effect of Pt for the dissociation of intermediate methoxy (CH_3O). **Yang et al. [104]** have discussed the effect of free surface carbon at the surface of WC on the catalytic activity. The authors have prepared the carbon free WC by O_2 plasma technique and found significant improvement in the HER and MOR activities for WC foils as well as Pt/WC foils. **Hsu et al. [105]** have studied the effect of Pt particles shape (dendrites and cubic) on the electrocatalytic activity of modified WC substrate (Pt/WC). The results have revealed that the dendrites Pt shows higher electrocatalytic activity for methanol oxidation as compared to cubic shape.

Hu et al. [106] prepared WC nano particles at an average size of 20 nm by using intermittent microwave heating (IMH) technique to support the Pd nanoparticles (Pd–WC/C). It gave much better performance for the oxidation of ethanol in alkaline media as compared to that of Pd/C with the more negative onset potential and higher peak current densities. The authors have also found reduction in the activation free energy for the reaction on Pd–WC/C electrocatalyst. **Hu et al. [107]** have extended the work for ethanol oxidation by analyzing the effect of porous MWCNT as well as Pd deposition on WC (Pd-WC/MWCNT). The current density obtained from this catalyst was found to be three times higher than Pd/C at the same Pt loading. The kinetic of the catalysts has also been measured with temperature which shows the enhanced activity with temperature.

Yang et al. [108] have proposed a mechanism for the enhancement in the catalytic activity for ethanol oxidation on anode by Pd decorated WC on graphene catalyst. The analysis revealed that due to the electron transfer from WC to Pd, electron density of Pd increases which weakens the adsorption of CO and promote the higher activity. **Yan et al.**

[109] loaded WC particles on hollow carbon spheres (HCS) to prepare WC-HCS composite. The prepared composite has small WC size, hollow and spherical shape with high specific surface area and can be used to analyze overall catalytic performance after Pd dispersion (Pd/WC-HCS) especially for ethanol oxidation. The results revealed that Pd/WC-HCS as electrocatalyst has 4.6 times higher peak current density and at least 130 mV more negative onset potential than those of Pd/C for ethanol oxidation. **Xiong et al. [110]** prepared high surface area WC microspheres by the template of carbon microspheres (WC/CMS). After the dispersion of Pt nanoparticles on the surface of WC/CMS to form Pt/WC/CMS, it shows higher electrocatalytic activity and anti-poisoning ability for the electrooxidation of ethanol over Pt/C electrocatalyst. Moreover, the rate constant of ORR for Pt/WC/CMS is observed to be twice as high as that of Pt/C, which indicates the synergetic effects between the Pt and the WC support.

Although, Pt show better performance as catalyst but its high cost and shortage provide a blockage in its usage for catalytic applications. Hence, an alternative low cost and comparable highly active metal electrocatalyst is essential. Among metals, silver (Ag) is found to be most active for the catalytic activity and can be used as electrocatalyst at nano scale **[111]**. Most of the authors **[111-113]** have tried to synthesize Pt free composite (Ag-WC/C) and used them as catalyst in electrochemical study. The results of the study have confirmed that due to the cooperative effect between WC and Ag, the electrode attribute enhanced HOR/HER response as well as shift in the onset potential for ORR towards positive side which is comparable to Pt based electrocatalyst (Pt/C). In one of the report, **Meng and Shen [114]** have studied ORR activity of Pt-free, Ag-W_2C/C composite in alkaline solution (KOH). The results revealed that the overpotential for ORR was significantly reduced on the WC nanocrystals promoted Ag (Ag-W_2C/C) composite electrocatalyst, showing a synergetic effect to improve the activity for ORR. This Pt free electrocatalyst also show unique activity for alcohol containing solution.

The work on the significant improvement in catalytic activity have also been reported by synthesizing core-shell structured catalyst in which titania **[115]** and W **[116]** act as core and WC act as shell. Additionally, authors have tried to reduce the metal loading after getting a composite by decorating the WC on high surface area material like reduced graphene oxide (WC/RGO) **[117, 118]** and hollow carbon spheres (WC/HCS) **[109]**. These metal deposited composites (Pt-WC/RGO; PtRu-WC/RGO, Pd-WC/HCS) attribute higher electrochemically active surface area and better CO tolerance toward MOR.

Tungsten carbide is not only used in fuel cell but also becomes important materials for the process of refining (hydro treating) the liquid fuel for getting nitrogen and sulphur content below 10 ppm **[119]**. The work of simultaneous hydrodesulphurization (HDS) has also been done by using tungsten carbide(s) doped with Pt **[120]**. Authors have also compared the effect of Pt addition before (Pt-W_2C) and after (W_2C-Pt) the synthesis of W_2C activity and found that for contact times between 0.08 and 0.31 s no influence of Pt on the hydrodesulphurization (HDS) activity was observed. Addition of Pt after the synthesis of W_2C (W_2C-Pt), show better response in the entire range of applied contact time as compared to W_2C and Pt-W_2C. **Zheng et al. [121]** have prepared nano rod WC (NR-WC) thin film on Ni substrate by DC magnetron sputtering technique. The main component formed in this film is WC_{1-x} which showed a good electrochemical activity for nitromethane electroreduction attributing higher current of 14.9 mA/cm^2 at potential -0.89 V while the required reaction activation energy was 12.3 kJ/mol. **Li et al. [122]** have tested the electrocatalytic activity for p-nitrophenol reduction by WC/CNT composites. The results showed that prepared nanocomposite (WC/CNT) have 29.55 m^2/g specific surface area and higher current peak value of 16.37 µA in basic solution as compared to purified CNT, nano size WC and hollow globe WC with mesoporosity. So it can be concluded that the catalytic activity of WC is strongly dependent on W/C ratio; particle size and surface oxidation.

Some of the critical works giving higher response for different electrochemical reactions (ORR/HER) are given in **table 2.1**.

Table 2.1: Comparative critical review of electrocatalysts for different electrochemical reactions.

Catalyst	Reaction	Onset potential	Remarks
Pt-WC/C	ORR	1.05 V vs SHE	150 mV more positive than commercial Pt/C electrocatalyst **[67]**
Pt-W_2C/C	ORR	1.0 V vs SHE	100 mV more positive than commercial Pt/C electrocatalyst **[72]**
PtPd-WC/C	HER	0.2 V vs SHE	Pd significantly increase the activity of Pt-WC/C for HER at higher acidic concentration **[77]**
Pt/W_2C	HER	-0.005 V vs RHE	2-3 times higher active than commercial Pt/C **[86]**

2.3 Goal of the present study

The literature study has explored different synthesis routes for obtaining tungsten carbide(s) nano powder and its electrochemical activity. It was observed from the synthesis part that precursor plays a very important role in shape, size and yield of the final product. However, these parameters are also influenced by reaction temperature, time and carbon source. Although literature has highlighted sufficient work done on the synthesis of tungsten mono-carbide (WC), but it lacks in providing sufficient information about the synthesis of tungsten semi-carbide (W_2C) as well as explaining the reaction mechanism of both phase (WC/W_2C). Moreover, the electrochemical study cannot explore the effect of different carbon sources (used for the synthesis of carbide) on the electrocatalytic activity of final product. Additionally, the influence of surface carbon on the electrochemical activity of tungsten carbide system ($W_xC@C$; x=1 or 2) has not presented in detail.

The goal of the present study is to optimize the conditions for the synthesis of WC and W_2C nano powder with the variation in temperature and time using thermo-chemical reduction method by using different carbon source(s). The basic understanding of the reduction/carburization mechanism based on the experimental results has been studied in detail in the present work. Also, the effect of carbon source on the thermal and electrochemical stability of final product has been studied. The aim of the present study is also to check the suitability of the synthesized product for oxidation of methanol and ethanol.

The procedure adopted for the synthesis and characterization details of WC/W_2C nano powders are given in next chapter of this thesis (Experimental procedure).

References:

[1]. L. E. Toth, *Transition metal carbides and nitrides*, Academic Press, New York (1971).

[2]. R. Koc, S. K. Kodambaka, *J. Eur. Ceram. Soc.* **20** (2000) 1859-1869.

[3]. Y. Hatano, M. Takamori, K. Matsuda, S. Ikeno, K. Fujii, K. Watanabe, *J. Nucl. Mater.* **307/311** (2002) 1339-1343.

[4]. F. A. C. Oliveira, J. C. Fernandes, J. M. Badie, B. Granier, L. G. Rosa, N. Shohoji, *Int. J. Refract. Met. H.* **25** (2007) 101-106.

[5]. F. A. C. Oliveira, B. Granier, J. M. Badie, J. C. Fernandes, L. G. Rosa, N. Shohoji, *Int. J. Refract. Met. H.* **25** (2007) 351-357.

[6]. P.G. Li, M. Lei, W.H. Tang, *Mater. Res. Bull.* **43** (2008) 3621-3626.

[7]. Y. Jin, X. Li, D. Liu, C. Liu, R. Yang, *Powder Technol.* **217** (2012) 482-485.

[8]. C. Suryanarayana, *Prog. Mater. Sci.* **46** (2001) 1-184.

[9]. G. Le Caër, E. B. Grosse, A. Pianelli, E. Bouzy, P. Matteazzi, *J. Mater. Sci.* **25** (1990) 4726-4731.

[10]. P. Matteazzi, G. Le Caër, *J. Am. Ceram. Soc.* **74** (1991)1382-1390.

[11]. G. M. Wang, S. J. Campbell, A. Calka, W. A. Kaczmarek, *J. Mater. Sci.* **32** (1997) 1461-1467.

[12]. G. L. Tan, X. J. Wu, *Powder Metall.* **41** (1998) 300-302.

[13]. M. Sherif El-Eskandarany, *J. Alloy Compd.* **296** (2000) 175-182.

[14]. M. Sherif El-Eskandarany, A. A. Mahday, H. A. Ahmed, A. H. Amer, *J. Alloy Compd.* **312** (2000) 315-325.

[15]. Z. G. Liu, K. Tsuchiya, M. Umemoto, *J. Mater. Sci.* **37** (2002) 1229-1235.

[16]. L. Zhang, G. Liu, Gui-bin Yang, S. Chen, Bai-yun Huang, Chuan-fu Zhang, *Int. J. Refract. Met. H.* **25** (2007) 166-170.

[17]. J. Ma, S.G. Zhu, *Int. J. Refract. Met. H.* **28** (2010) 623-627.

[18]. S. Bolokang, C. Banganayi, M. Phasha, *Int. J. Refract. Met. H.* **28** (2010) 211-216.

[19]. M. Razavi, M. R. Rahimipour, R. Yazdani-Rad, *J. Alloy Compd.* **509** (2011) 6683-6688.

[20]. R. Yang, T. Xing, R. Xu, M. Li, *Int. J. Refract. Met. H.* **29** (2011) 138-140.

[21]. L. E. Mcchandlish, B. H. Kear, S. J. Bhatia, *US patent 5352269* (1994).

[22]. G. E. Spriggs, *Int. J. Refract. Met. H.* **13** (1995) 241-255.

[23]. L. Gao, B. H. Kear, P. Seegopaul, *US patent 5919428* (1999).

[24]. P. Seegopaul, L. Gao, *US patent 6524366* (2003).

[25]. B. K. Kim, G. G. Ha, Y. Woo, *US patent 6511551* (2003).

[26]. Z. Y. Zhang, S. Wahlberg, M. S. Wang, M. Muhammed, *Nanostruct. Mater.* **12** (1999) 163-166.

[27]. J. Hojo, T. Oku, A. Kato, *J. Less-Common. Met.* **59** (1978) 85-95.

[28]. D. Garg, P. N. Dyer, D. B. Dimos, S. Sunder, H. E. Hintermann, M. Maillat, *J. Am. Ceram. Soc.* **75** (1992) 1008-1011.

[29]. C. M. Kelly, *Thin Solid Films* **219** (1992) 103-108.

[30]. C. W. Won, B. S. Chun, H. Y. Sohn, *J. Mater. Res.* **8** (1993) 2702-2708.

[31]. M. Fitzsimmons, V. K. Sarin, *Surf. Coat. Tech.* **76-77** (1995) 250-255.

[32]. X. Tang, R. Haubner, B. Lux, B. Kieffer, *J. Phys. IV Colloq.* **510** (1995) 13-20.

[33]. F. F. P Medeiros, S. A. De Oliveira, C. P. De Souza, A. G. P. Da Silva, U. U. Gomes, J. F. De Souza, *Mater. Sci. Eng. A* **315** (2001) 58-62.

[34]. H. Y. Sohn, T. Ryu, J. W. Choi, K. S. Hwang, G. Han, Y. J. Choi, Z. Z. Fang, *Jom-J. Min. Met. Mat. S.* **59** (2007) 44-49.

[35]. B. Q. Yang, X. P. Wang, H. X. Zhang, Z. B. Wang, P. X. Feng, *Mater. Lett.* **62** (2008) 1547-1550.

[36]. F. F. P. de Medeiros, A. G. P. da Silva, C. P. de Souza, U. U. Gomes, *Int. J. Refract. Met. H.* **27** (2009) 43-47.

[37]. S. Cetinkaya, S. Eroglu, *Int. J. Refract. Met. H.* **29** (2011) 214-220.

[38]. L. Tong, R. G. Reddy, *Scripta Mater.* **52** (2005) 1253-1258.

[39]. T. Ryu, H. Y. Sohn, K. S. Hwang, Z. Z. Fang, *J. Mater. Sci.* **43** (2008) 5185-5192.

[40]. A. G. Merzhanov, *Ceram. Int.* **21** (1995) 371-379.

[41]. A. G. Merzhanov, *J. Mater. Chem.* **14** (2004) 1779-1786.

[42]. H. H. Nersisyan, H. I. Won, C. W. Won, *Mater. Lett.* **59** (2005) 3950-3954.

[43]. H. H. Nersisyan, H. I. Won, C. W. Won, J. H. Lee, *Mater. Chem. Phys.* **94** (2005) 153-158.

[44]. H. I. Won, H. H. Nersisyan, C. W. Won, *J. Mater. Res.* **23** (2008) 2393-2397.

[45]. H. I. Won, H. H. Nersisyan, C. W. Won, *J. Nanopart. Res.* **12** (2010) 493-500.

[46]. Q. Wang, F. Cao, Q. Chen, *Mater. Chem. Phys.* **95** (2006) 113-116.

[47]. K. M. Reddy, T. N. Rao, K. Radha, J. Joardar, *J. Alloy Compd.* **494** (2010) 404-409.

[48]. K. M. Reddy, T. N. Rao, J. Joardar, *Mater. Chem. Phys.* **128** (2011) 121-126.

[49]. S. Aravinth, B. Sankar, M. Kamaraj, S. R. Chakravarthy, R. Sarathi, *Int. J. Refract. Met. H.* **33** (2012) 53-57.

[50]. G. Xi, Y. Liu, X. Liu, X. Wang, Y. Qian, *J. Phys. Chem. B* **110** (2006) 14172-14178.

[51]. C. Guo, Y. Liu, X. Ma, Y. Qian, L. Xu, *Chem. Lett.* **35** (2006) 1210-1211.

[52]. C. A. Ma, Z. Y. Chen, W. F. Lin, F. M. Zhao, M. Q. Shi, *Micropor. Mesopor. Mat.* **149** (2012) 76-85.

[53]. J. Ma, Y. Du, *J. Alloy Compd.* **448** (2008) 215-218.

[54]. A. Kumar, K. Singh, O. P. Pandey, *Physica E* **41** (2009) 677-684.

[55]. A. Kumar, K. Singh, O. P. Pandey, *Physica E* **42** (2010) 2477-2483.

[56]. A. Kumar, K. Singh, O. P. Pandey, *Int. J. Refract. Met. H.* **29** (2011) 555-558.

[57]. H. Singh, O. P. Pandey, *Ceram. Int.* **39** (2013) 6703-6706.

[58]. T. Wang, D. Gao, J. Zhuo, Z. Zhu, P. Papakonstantinou, Y. Li, M. Li, *Chem. Eur. J.* **19** (2013) 11939-11948.

[59]. Y. Wang, Y. Nie, W. Ding, S. G. Chen, K. Xiong, X. Q. Qi, Y. Zhang, J. Wang, et al., *Chem. Commun.* **51** (2015) 8942-8945.

[60]. T. Reier, M. Oezaslan, P. Strasser, *ACS Catal.* **2** (2012) 1765-1772.

[61]. Y. Hara, N. Minami, H. Matsumoto, H. Itagaki, *Appl. Catal. A-Gen.* **332** (2007) 289-296.

[62]. V. M. Nikolic, I. M. Perovic, N. M. Gavrilov, I. A. Pašti, A. B. Saponjic, P. J. Vulic, S. D. Karic, B. M. Babic, et al., *Int. J. Hydrogen Energ.* **39** (2014) 11175-11185.

[63]. D. Merki, X. Hu, *Energy Environ. Sci.* **4** (2011) 3878-3888.

[64]. J. W. Hong, S. W. Kang, B. S. Choi, D. Kim, S. B. Lee, S. W. Han, *ACS Nano* **6** (2012) 2410-2419.

[65]. R. B. Levy, M. Boudart, *Science* **181** (1973) 547-549.

[66]. H. Meng, P. K. Shen, *Chem. Commun.* (2005) 4408-4410.

[67]. M. Nie, P. K. Shen, M. Wu, Z. Wei, H. Meng, *J. Power Sources* **162** (2006) 173-176.

[68]. M. Nie, P. K. Shen, Z. Wei, *J. Power Sources* **167** (2007) 69-73.

[69]. H. Chhina, S. Campbell, O. Kesler, *J. Power Sources* **164** (2007) 431-440.

[70]. H. Chhina, S. Campbell, O. Kesler, *J. Power Sources* **179** (2008) 50-59.

[71]. Z. Yan, G. He, M. Cai, H. Meng, P. K. Shen, *J. Power Sources* **242** (2013) 817-823.

[72]. H. Meng, P. K. Shen, *J. Phys. Chem. B* **109** (2005) 22705-22709.

[73]. N. R. Elezović, B. M. Babić, Lj. Gajić-Krstajić, P. Ercius, V. R. Radmilović, N. V. Krstajić, Lj. M. Vračar, *Electrochim. Acta* **69** (2012) 239-246.

[74]. Q. Zhu, S. Zhou, X. Wang, S. Dai, *J. Power Sources* **193** (2009) 495-500.

[75]. W. Zhu, A. Ignaszak, C. Song, R. Baker, R. Hui, J. Zhang, F. Nan, G. Botton, et al., *Electrochim. Acta* **61** (2012) 198-206.

[76]. A. R. Ko, Y. W. Lee, J. S. Moon, S. B. Han, G. Cao, K. W. Park, *Appl. Catal. A-Gen.* **477** (2014) 102-108.

[77]. M. Wu, P. K. Shen, Z. Wei, S. Song, M. Nie, *J. Power Sources* **166** (2007) 310-316.

[78]. E. J. Rees, K. Essaki, C. D. A. Brady, G. T. Burstein, *J. Power Sources* **188** (2009) 75-81.

[79]. I. J. Hsu, Y. C. Kimmel, X. Jiang, B. G. Willis, J. G. Chen, *Chem. Commun.* **48** (2012) 1063-1065.

[80]. Y. Yan, B. Xia, X. Qi, H. Wang, R. Xu, J. Y. Wang, H. Zhang, X. Wang, *Chem. Commun.* **49** (2013) 4884-4886.

[81]. T. G. Kelly, S. T. Hunt, D. V. Esposito, J. G. Chen, *Int. J. Hydrogen Energ.* **38** (2013) 5638-5644.

[82]. Y. C. Kimmel, D. V. Esposito, R. W. Birkmire, J. G. Chen, *Int. J. Hydrogen Energ.* **37** (2012) 3019-3024.

[83]. A. L. T. García, J. O. Jensen, N. J. Bjerrum, Q. Li, *Electrochim. Acta* **137** (2014) 639-646.

[84]. A. V. Nikiforov, I. M. Petrushina, E. Christensen, N. V. Alexeev, A. V. Samokhin, N. J. Bjerrum, *Int. J. Hydrogen Energ.* **37** (2012) 18591-18597.

[85]. F. Harnisch, G. Sievers, U. Schröder, *Appl. Catal. B-Environ.* **89** (2009) 455-458.

[86]. D. J. Ham, R. Ganesan, J. S. Lee, *Int. J. Hydrogen Energ.* **33** (2008) 6865-6872.

[87]. H. Zheng, J. Huang, W. Wang, C. Ma, *Electrochem. Commun.* **7** (2005) 1045-1049.

[88]. X. G. Yang, C. Y. Wang, *Appl. Phys. Lett.* **86** (2005) 224104 (1-3).

[89]. G. Lu, J. S. Cooper, P. J. McGinn, *J. Power Sources* **161** (2006) 106-114.

[90]. Y. Hara, N. Minami, H. Itagaki, *Appl. Catal. A-Gen.* **323** (2007) 86-93.

[91]. V. Glibin, L. Svirko, I. B. Kandybovich, D. Karamanev, *Surf. Sci.* **604** (2010) 500-507.

[92]. G. V. Boikova, V. Schneider, K. Wiesener, G. V. Jutaeva, M. P. Tarasevich, *Soviet J. Electrochem.* **22** (1986) 1135-1138.

[93]. F. Şen, S. Şen, G. Gökağaç, *Phys. Chem. Chem. Phys.* **13** (2011) 1676-1684.

[94]. K. Huang, K. Bi, J. C. Xu, C. Liang, S. Lin, W. J. Wang, T. Z. Yang, Y. X. Du, et al., *Electrochim. Acta* **174** (2015) 172-177.

[95]. H. Zheng, Z. Chen, Y. Li, C. Ma, *Electrochim. Acta* **108** (2013) 486-490.

[96]. S. Bukola, B. Merzougui, A. Akinpelu, M. Zeama, *Electrochim. Acta* **190** (2016) 1113-1123.

[97]. G. Zhong, H. Wang, H. Yu, F. Peng, *Fuel Cells* **13** (2013) 387-391.

[98]. Z. Zhao, X. Fang, Y. Li, Y. Wang, P. K. Shen, F. Xie, X. Zhang, *Electrochem. Commun.* **11** (2009) 290-293.

[99]. M. Rahsepar, M. Pakshir, P. Nikolaev, Y. Piao, H. Kim, *Int. J. Hydrogen Energ.* **39** (2014) 15706-15717.

[100]. J. P. Bosco, K. Sasaki, M. Sadakane, W. Ueda, J. G. Chen, *Chem. Mater.* **22** (2010) 966-973.

[101]. E. C. Weigert, A. L. Stottlemyer, M. B. Zellner, J. G. Chen, *J. Phys. Chem. C* **111** (2007) 14617-14620.

[102]. Z. J. Mellinger, T. G. Kelly, J. G. Chen, *ACS Catal.* **2** (2012) 751-758.

[103]. M. B. Zellnera, J. G. Chen, *Catal. Today* **99** (2005) 299-307.

[104]. X. Yang, Y. C. Kimmel, J. Fu, B. E. Koel, J. G. Chen, *ACS Catal.* **2** (2012) 765-769.

[105]. I. J. Hsu, D. V. Esposito, E. G. Mahoney, A. Black, J. G. Chen, *J. Power Sources* **196** (2011) 8307- 8312.

[106]. F. P. Hu, P. K. Shen, *J. Power Sources* **173** (2007) 877-881.

[107]. F. Hu, G. Cui, Z. Wei, P. K. Shen, *Electrochem. Commun.* **10** (2008) 1303-1306.

[108]. J. Yang, Y. Xie, R. Wang, B. Jiang, C. Tian, G. Mu, J. Yin, B. Wang, et al., *ACS Appl. Mater. Interfaces* **5** (2013) 6571-6579.

[109]. Z. Yan, Y. Gu, W. Wei, Z. Jiang, J. Xie, P. K. Shen, *Fuel Cells* **15** (2015) 256-261.

[110]. L. Xiong, L. Zheng, C. Liu, L. Jin, Q. Liu, J. Xu, *J. Electrochem. Soc.* **162** (2015) F468-F473.

[111]. H. Bunazawa, Y. Yamazaki, *J. Power Sources* **182** (2008) 48-51.

[112]. C. D. A. Brady, E. J. Rees, G. T. Burstein, *J. Power Sources* **179** (2008) 17-26.

[113]. X. B. Gong, S. J. You, X. H. Wang, Y. Gan, R. N. Zhang, N. Q. Ren, *J. Power Sources* **225** (2013) 330-337.

[114]. H. Meng, P. K. Shen, *Electrochem. Commun.* **8** (2006) 588-594.

[115]. S. Hu, B. Shi, G. Yao, G. Li, C. Ma, *Mater. Res. Bull.* **46** (2011) 1738-1745.

[116]. M. D. Obradović, B. M. Babić, V. R. Radmilović, N. V. Krstajić, S. Lj. Gojković, *Int. J. Hydrogen Energ.* **37** (2012) 10671-10679.

[117]. C. Ma, W. Liu, M. Shi, X. Lang, Y. Chu, Z. Chen, D. Zhao, W. Lin, et al., *Electrochim. Acta* **114** (2013) 133-141.

[118]. M. Shi, W. Zhang, D. Zhao, Y. Chu, C. Ma, *Electrochim. Acta* **143** (2014) 222-231.

[119]. E. Furimsky, *Appl. Catal. A-Gen.* **240** (2003) 1-28.

[120]. M. Lewandowski, P. Da Costa, D. Benichou, C. Sayag, *Appl. Catal. B-Environ.* **93** (2010) 241-249.

[121]. H. Zheng, C. Ma, W. Wang, J. Huang, *Electrochem. Commun.* **8** (2006) 977-981.
[122]. G. Li, C. Ma, J. Tang, J. Sheng, *Electrochim. Acta* **52** (2007) 2018-2023.

CHAPTER 3

EXPERIMENTAL PROCEDURE

Overview

The detail of experimental procedure followed for the synthesis of WC and W_2C nanopowders from WO_3 is presented in this chapter. Different techniques like X-ray diffraction (XRD), Thermal analysis (DSC/TGA/DTG), Transmission electron microscopy (TEM), Raman spectroscopy, BET analysis used for the characterization of prepared nano powders have also been given in this chapter. The feasibility to use the synthesized powders for catalytic application has been analyzed by electrochemical measurements. For this, the details of samples preparation and their testing have been given at the end of this chapter.

3.1 Carbide powder synthesis (WC/W_2C)

3.1.1 Precursors

For the synthesis of carbide nano particles, tungsten trioxide (99.9%, Loba Chemie), magnesium (99.9 %, Loba Chemie), ethanol (99%, Merck, Germany), acetone (99%, Merck, Germany), hexane (99% Merck, Germany) activated charcoal (99%, S.D. Fine Chemicals), HCl (99%, S.D. Fine Chemicals) are used as per their requirement without any further purification.

3.1.2 Methodology

The synthesis route followed has been categorized in two-part viz wet synthesis and dry synthesis. In case of wet synthesis, the known amount of WO_3 and Mg powders are mixed properly in an agate mortar pestle for 5 min. The mixture is then put into a specially designed stainless steel autoclave along with the source of carbon in the liquid form (acetone and hexane). Similarly in case of dry synthesis, the known amount of WO_3, Mg and activated charcoal as a carbon source after mixing properly for 5 min in an agate mortar pestle were charged in the autoclave. The autoclave was sealed and then put inside the electric furnace at room temperature. The temperature of the furnace was raised from room temperature to desired temperature with the heating rate 5 °C/min and then maintained at that temperature for different time period. After that the autoclave was allowed to cool to room temperature normally inside the furnace for the synthesis of tungsten mono-carbide (WC) nano powder. While for getting the product tungsten semi-carbide (W_2C) nano powder the air quenching of the autoclave has been done. The resultant product was collected and washed by dilute HCl (1:1) to remove MgO and other by products. After leaching, the powder was washed with distilled water several times to remove HCl. Finally, the obtained product was washed with acetone and then dried in vacuum at 100 °C. The details of experimental procedure are given in **figure 3.1** as flow chart.

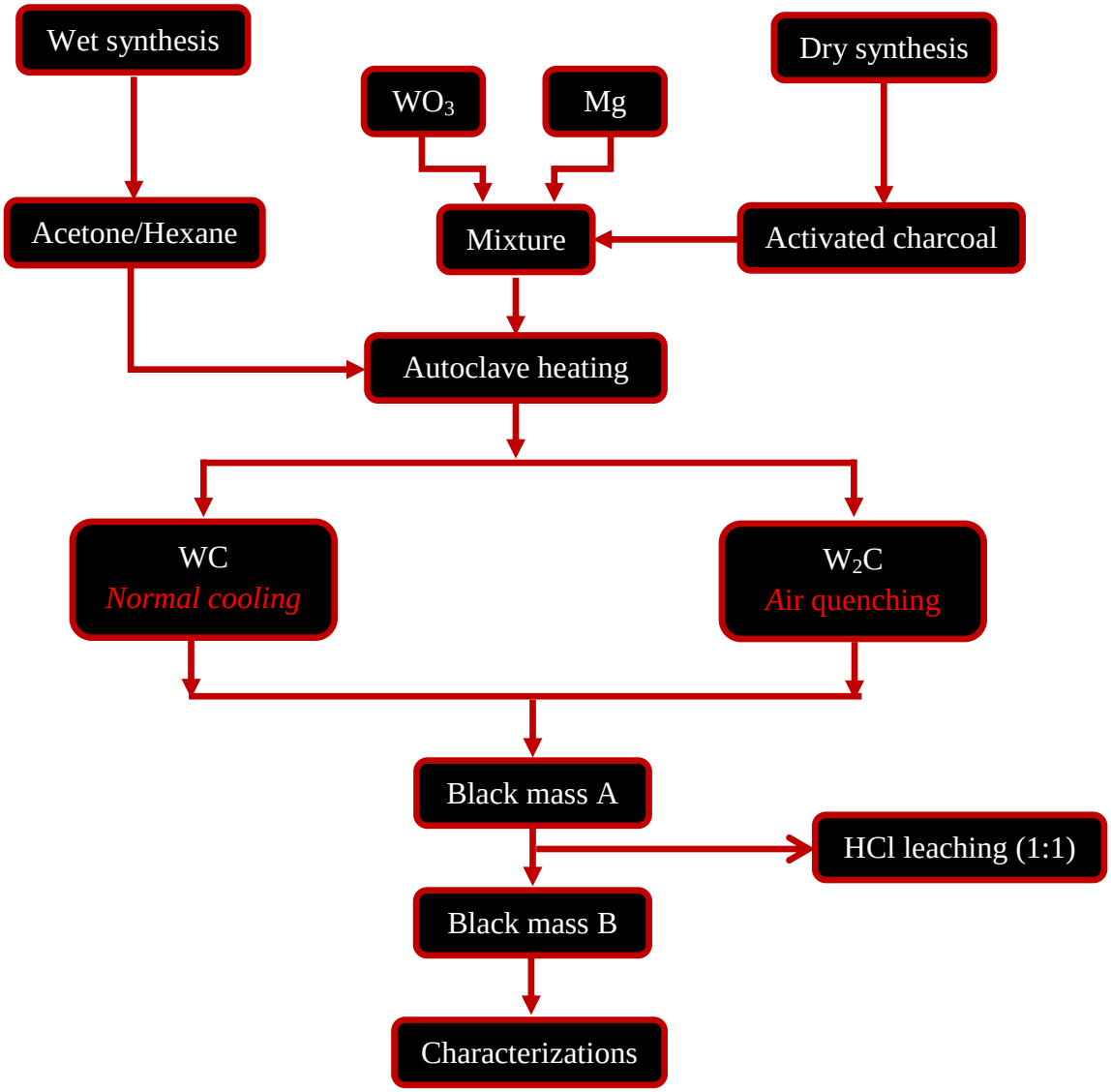

Figure 3.1: Flow chart of WC/W_2C nano powder synthesis.

3.2 Materials characterization

The obtained powders were characterized using different techniques; the technical details of these are given below.

3.2.1 X-ray diffraction study (XRD)

X-ray diffraction (XRD) is a technique, which is most commonly used to determine the crystal structure of synthesized materials. In this technique the intensity of the scattered X-ray is measured as a function of the angle between X-ray source and the sample, wavelength as expressed according to Bragg´s law [**1**]:

$$n\lambda = 2d\,Sin\theta \quad (3.1)$$

where n is an order of reflection, λ is wavelength of the incident X-ray, d is the spacing between the lattice planes, and θ is the angle between the incident ray and set of parallel atomic planes.

In the current work, the XRD of the samples was performed using PANalytical Xpert-Pro with CuKα radiation (λ = 1.54 Å) obtained from the copper target using an inbuilt Ni filter. The X-ray powder diffraction data were collected for all samples at room temperature between $20° \leq 2\theta \leq 80°$ with a step size of 0.0130° (2θ). Moreover, before the XRD analysis, the grinding of powder samples was done in an agate mortar pestle for uniform particle size distribution. Crystallite size of the synthesized samples was determined by XRD profile technique. All the peaks in the XRD pattern are indexed by International Centre for Diffraction Data (ICDD) data base.

3.2.2 Raman spectroscopy

Raman spectroscopy is based on the inelastic scattering of light emitted from a monochromatic source of light i.e. laser source. It represents a spectral fingerprint, by which molecular units can be recognized. The Raman technique provides both qualitative and quantitative information for multi-component mixtures to study solid, liquid and gaseous samples. In this work, Raman spectroscopy was used to determine the type of carbon in the synthesized carbide nano powder. The Raman measurements of the powders were collected at room temperature in the range of 400 cm^{-1}–2000 cm^{-1} using Renishaw via Raman spectrometer. Argon ion laser of wavelength 514.5 nm was used for excitation with 20 mW output. All samples were deposited on a glass plate in powder form without using any solvent.

3.2.3 N_2 Physisorption

The surface area and porosity (texture properties) of any solid materials are considered by two main important physical properties that impact the quality and utility of solid phase. Hence, textural properties of materials plays major role in the processing, blending of chemical products, purification and their stability. Gas physisorption is generally used for the measurements of surface area and porosity of sample. This involves exposing solid materials to gases at a specific conditions and evaluating either the weight uptake or the sample volume [**2**]. Among all the readily available gases and vapours, nitrogen gas has been used as

adsorption/desorption to determine the specific surface areas and pore volumes of porous materials. The adsorption/desorption isotherm represents the changes of adsorbed gas volume at a fixed temperature as a function of pressure. However, its shape gives direct information about the porosity, total pore volume, and pore size distribution and layer-by-layer adsorption. Referring to the IUPAC conventions [**3**], porous materials can be described by 6 different isotherm types, shown in **figure 3.2**. The type I isotherm is attributed to microporous solids, while type II isotherm represents non-restricted monolayer-multilayer adsorption for non-porous or macroporous adsorbents [**4**]. The type III and V isotherms are uncommon; in those cases, the adsorbent-adsorbate interactions are rather weak.

The type IV isotherm, with a distinct hysteresis loop governed by capillary condensation, and is characteristic for mesoporous materials. The type VI isotherm is associated with multistep layer-on-layer adsorption on a non-porous surface. Specific surface areas (SSAs) are determined by the Brunauer-Emmett-Teller (BET) method [**5**]. Pore-size distributions are commonly obtained using the Barrett-Joyner-Halenda (BJH) method [**6**]. The N_2 sorption studies for surface analysis of synthesized samples were conducted using a Tristar 3000 (Micromeritics) to determine the Brunauer–Emmett–Teller (BET) surface area, the pore size, and the pore volume at 77 K by degassing the sample at 150 °C for 2 h.

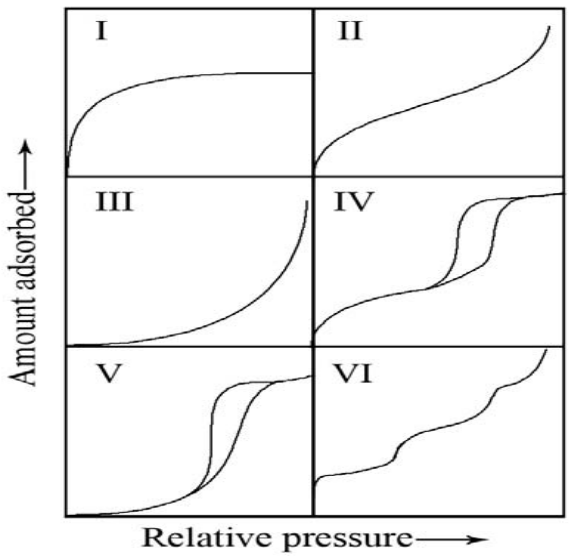

Figure 3.2: Types of sorption isotherms **[3].**

3.2.4 Transmission Electron Microscopy (TEM)

Transmission Electron Microscopy (TEM) is used to study the structure of specimens below the atomic level [**7**]. For TEM analysis, the specimen must be thin enough (<100 nm) to transmit the electron. This facilitates to increase the spatial resolution in imaging (down to individual atoms) as well as the possibility of carrying out diffraction from nano-sized volumes. Moreover, high resolution transmission electron microscopy (HRTEM) provides information about the structural defects, interfaces as well as individual grains having diameter of a few nanometres and lattice spacing. The microstructural features of the synthesized powder samples were analyzed with JEOL 2100F operating at 200 kV. For TEM analysis, the powder samples were dispersed in ethanol by ultrasonication for 20 min. One drop of the suspension was dropped on the carbon coated copper TEM grid and allowed to evaporate the ethanol at room temperature.

3.2.5 Thermal analysis

Thermal analysis is a technique which observes the changes in properties of material with temperature. In this technique, the sample specimen is handled with a controlled temperature program in a controlled atmosphere. In thermal analysis, thermo gravimetric analysis (TGA) is a technique which determines thermal stability of a specimen by monitoring the changes in mass of the specimen as a function of temperature or time. This technique is commonly employed to determine the change in mass of composite materials, degradation temperatures of polymers, and the amount of solvent residues [**8**]. In addition to weight changes, the heat flow into the specimen compared to that of the reference can also be recorded via differential scanning calorimetry (DSC). In this case, the temperature should be the same until two thermal events (exothermic and endothermic) occur. The area under the endotherm or exotherm peak is also related to the enthalpy (ΔH) of the thermal event **[9]**. Moreover, in order to understand the kinetics of samples oxidation first derivative of TG curve has been taken and analyzed under derivative thermogravimetry (DTG). The TGA/DSC analysis of the synthesized powder samples was done at heating rate of 5 °C/min in the temperature range 50-900 °C in air atmosphere by NETZSCH STA 449F3 using alumina crucible.

3.2.6 Electrochemical measurements

The electrochemical measurements of the synthesized sample normally use *cyclic voltammetry technique (CV).* It is a reversible technique generally used to acquire qualitative

information about electrochemical properties of redox active species displaying a reversible wave within a specified wide potential range. It can be used to get kinetic information about the electrode reaction which usually involves electron-transfer reaction. It is influenced by electrode potential. It provides a direct estimation of electrode reversibility, because the potentials at which oxidation and reduction occur are observed directly [**10**]. In a typical experiment, the working electrode´s potential is controlled relative to a reference electrode (RE) such as a saturated calomel electrode (SCE) or a silver/silver chloride electrode (Ag/AgCl) and cycled linearly between two potential values at which the oxidation and the reduction occur. Actual current flow is scanned between the working electrode (WE) and the counter electrode (CE) resulting in a potential-current cyclic voltammogram. A CV curve is acquired by measuring the current at the working electrode during the potential scan. Such kind of technique can be widely used in numerous applications, such as understanding redox and mechanistic behavior in chemical reactions.

3.2.6.1 Deposition of Pt

In order to measure the electrochemical properties of the synthesized powders, Pt nano particles were deposited on synthesized powder by dispersing 40 mg powder in 20 ml of ethanol in ultrasonic bath and then 100 µL hexachloroplatinic acid (H_2PtCl_6) aqueous solution was added to ultrasonicated solution. In the mixture of metal salt and synthesized powder support, appropriate amount of 0.05 M NaOH/ethanol was added to maintain the pH~10. The precipitate was washed with high purity water and then dried at 80 °C.

3.2.6.2 Electrode fabrication

The top surface of glassy carbon electrode (GCE) rod having 3 mm diameter was pre cleaned with emery paper. Typically 4 mg powder sample with and without Pt loadings was mixed with 1mL of ethanol. The mixture was treated ultrasonically for 20 min for uniform dispersion. 10 µL of mixture was then dropped onto the surface of GCE. Finally a drop of 10 µL of Nafion® 117 solution (Sigma Aldrich) was dropped onto the top surface and left in air for overnight drying.

In current work, the electrochemical measurements were performed at Bio-Logic EC Lab SP300 by standard three compartment electrochemical cell. For CV measurements GCE with an area of 0.07065 cm^2 used as working electrode, Pt wire as the counter electrode and saturated calomel electrode (SCE) as the reference electrode. For electrochemical stability,

the electrodes were immersed in 0.5 mol/L H_2SO_4 solution and CV curves were recorded at room temperature from -0.2 V and 1.2 V with a scan rate of 30 mV/s. Thereafter, the methanol and ethanol electrolyte was added and CV curves were recorded at room temperature for methanol oxidation reaction (MOR) and ethanol oxidation reactions (EOR) separately from -0.2 to 1.2 V at a scan rate of 30 mV/s. The influence of methanol and ethanol concentration on the catalyst catalytic performance was tested with concentrations 0.5, 0.7 and 0.9 mol/L.

References:

[1]. B. D. Cullity, *Elements of X-ray Diffraction*, Addison-Wesley Publishing Company: USA (1956).

[2]. K. Sing, *Colloid. Surface A* **187-188** (2001) 3-9.

[3]. J. B. Condon, *Surface Area and Porosity Determinations by Physisorption Measurements and Theory*, Elsevier Amsterdam, Netherlands (2006).

[4]. X. H. Lin, S. F. Y. Li, *Appl. Catal. B-Environ.* **170-171** (2015) 263-272.

[5]. P. H. Emmett, S. Brunauer, *J. Am. Chem. Soc.* **59** (1937) 1553-1564.

[6]. E. P. Barrett, L. G. Joyner, P. H. Halenda, *J. Am. Chem. Soc.* **73** (1951) 373-380.

[7]. D. B. Williams, C. B. Carter, *Transmission Electron Microscopy: A Textbook for Materials Science*, Springer, New York (2009).

[8]. B. Wunderlich, *Thermal analysis of Polymeric Materials*, Springer Berlin Heidelberg, New York (2005).

[9]. I. M. Hodge, *J. Non-Cryst. Solids* **169** (1994) 211-266.

[10]. R. S. Nicholson, *Anal. Chem.* **37** (1965) 1351-1355.

CHAPTER 4

RESULTS AND DISCUSSION-I

(SYNTHESIS OF TUNGSTEN CARBIDES NANO POWDERS)

Overview

This chapter comprises of two sections. In the first section the synthesis of tungsten mono-carbide (WC) nano powder and in the second section the formation of tungsten semi-carbide (W_2C) nano powders by using three different carbon sources has been presented. XRD results of all the synthesized samples have been analyzed and discussed. Based on XRD results and thermodynamics parameters, the formation mechanism of these nano particles has been described. From the thermal analysis results, the stability of the synthesized powders over different range of temperature(s) has been evaluated. Raman analysis has been done to ascribe the amorphous and crystalline behavior of the synthesized samples. Surface area and pore size distribution of the synthesized samples has been analyzed by BET technique. TEM results have been presented and discussed to analyze the microstructure of the synthesized powders to confirm the crystal structure of product phase by measuring the lattice spacing using HRTEM.

In this chapter, the work on synthesis of WC and W_2C nano particles using different carbon sources are presented. In the first part of this chapter, the details of the synthesis of WC nano powder have been presented and discussed. The synthesis has been done by taking magnesium (Mg) metal powder as reducing agent and different carbon sources viz acetone, activated charcoal and hexane along with tungsten oxide (WO_3). The reaction kinetics of these carbon sources for the single- phase formation of WC have been analyzed and is presented.

4.1 Synthesis of tungsten mono-carbide (WC)

4.1.1 X-ray diffraction analysis (XRD)

4.1.1.1 Acetone as carburizing agent

In order to obtain the pure phase of WC nano powder, WO_3 (2.314 g), Mg (2.304 g) and acetone (30 mL) have been used as metal oxide, reducing agent and carburizing agent, respectively. The samples obtained at different reaction temperature and times are designated as *AT-t* where *A*, *T* and *t* corresponds to acetone, reaction temperature (°C) and reaction time (h), respectively.

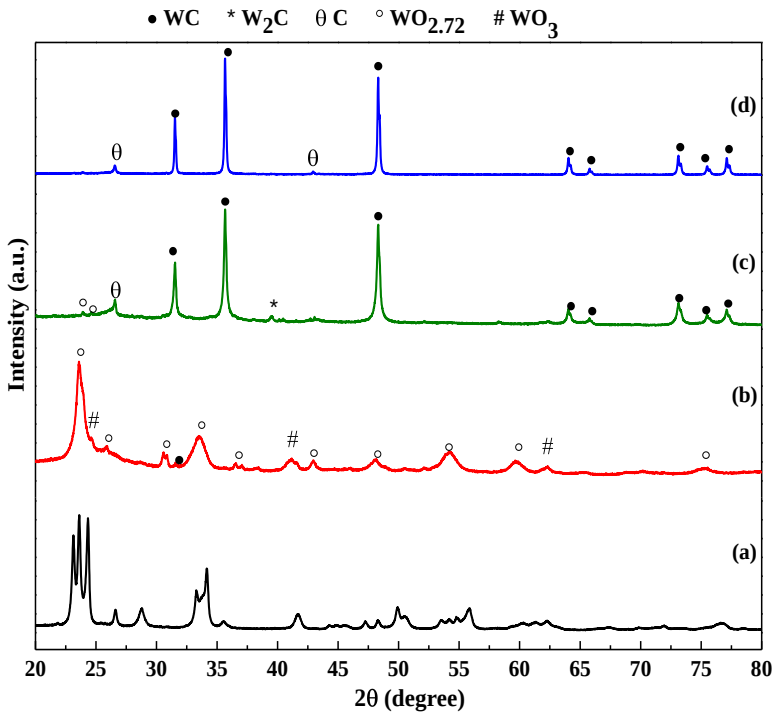

Figure 4.1: XRD patterns of **(a)** pure WO_3 **(b)** A600-01 **(c)** A600-02 and **(d)** A600-10.

Figure 4.1 shows the XRD patterns after acid treatment of samples obtained at 600 °C for different holding time by using acetone as carbon source. Tungsten-containing phases are identified using reference XRD patterns as WC (ICDD reference number 01-072-0097); W_2C (ICDD reference number 00-020-1315) and $WO_{2.72}$ (ICDD reference number 01-071-2450). The effect of reaction time on the reduction/carburization of WO_3 has been observed clearly in **figure 4.1**.

It is evident from **figure 4.1(b)** that precursor WO_3 reduced to $WO_{2.72}$ and partially carburized after 1 h in sample A600-01. But the appearance of small peak of WC phase along with oxide ($WO_{2.72}$) signifies the lack of sufficient time for the reduction/carburization. The appearance of $WO_{2.72}$ clearly indicates that such kind of reduction will be very fast and occurred in multi-step. However, a significant change has been revealed in the XRD pattern with the increase in reaction time to 2 h with the appearance of WC and W_2C peaks in **figure 4.1(c))**. It seems that the percentage of WC has been increased with the increase in synthesis time from 1 to 2 h. After considering this fact, the reaction time has been increased to 10 h and observed that the lower oxide $WO_{2.72}$ and semi carbide (W_2C) phases have been fully converted into WC (**figure 4.1(d))**. **Figure 4.2** shows the Rietveld refined XRD pattern of acid treated sample A600-10, which confirms the formation of WC phase (hexagonal; *P-6m2*, χ^2 =1.83).

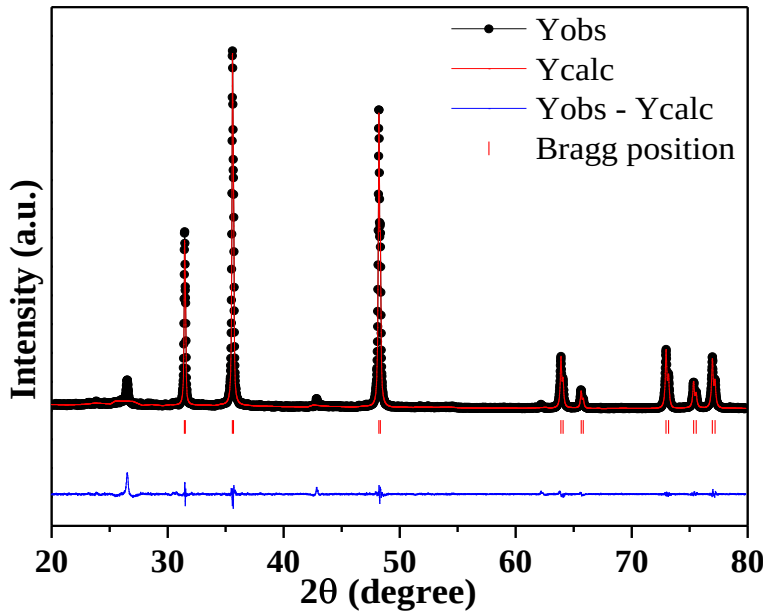

Figure 4.2: Typical Rietveld refined profile with difference plot for the XRD pattern showing WC phase of sample A600-10.

4.1.1.2 Mechanism for the synthesis of WC

In order to obtain the reaction mechanism for the formation of WC, it becomes essential to consider the various reactions that eventually take place while heating the autoclave at specified temperature. After heating the mixture of WO_3, Mg and acetone to a certain temperature, there are several reactions that occur during the reduction/carburization of oxide. During the reduction reactions, lower tungsten oxide phase(s) as intermediate products formed before the final tungsten (W) phase is obtained. The path followed by the reduction of WO_3 through intermediates products has been reported by many authors **[1-4]**.

Initially, the kinetics of the carburization process, mainly involves the decomposition of acetone (C_3H_6O) into carbon and diffusion of carbon atoms into the reduced W particles. Magnesium (Mg) being highly reactive substance, absorbs oxygen from the autoclave atmosphere and converts into MgO as a byproduct. It is well reported that MgO is the most active catalyst for the decomposition of acetone [**5**]. So, it facilitates the decomposition of acetone at lower temperature. The acetone gets decomposed into C-containing intermediate complex species and hydrogen with homogeneous reactions. But, it is difficult to say about the formed intermediate product at such a low temperature range. Since, the overall reaction is taking place in the presence of air inside the autoclave, so the reaction will be exothermic and the internally generated act as endothermic heat for the breaking of C-C and C-H bond.

Hydrogen being the smallest molecule has higher diffusion coefficient and diffused through the surface of WO_3. This diffused hydrogen reacts with oxygen of WO_3 and creates steam, which causes the stresses at the surface of WO_3 and at a later stage; it leads to the fragmentation of WO_3 powders [**6**]. This fragmentation process enhanced the reaction rate due to produced higher surface area of WO_3. Once a critical crystal size of fragmented WO_3 is reached, the reaction becomes self-propagating with either unreacted Mg or *in-situ* produced carbon to form W via the formation of lower oxide ($WO_3 \rightarrow W_xO_y(WO_{2.72}) \rightarrow W$). Hence, the kinetic of this reduction is clearly favored by increasing the surface energy of metal oxide(s) because of the newly generated surfaces of fragmented WO_3 and favoring the intimate contact with the reductant(s). The formation of the intermediate Magneli phase ($WO_{2.72}$) shown in **figure 4.1(b)** also play an important role in reducing the synthesis temperature of carbide phase [**7**].

Since, the entire system is under significant pressure of gasses, so lower tungsten oxides $WO_{2.72}$ at 600 °C has relatively high vapor pressure [**8**]. **Li et al.** [**9**] have also observed that a

derivative sub-oxide or possibly defective sub-oxide, acts as a preferential nucleation site for the carbide formation. However, the process of carburization begins only when the solid is reduced to an overall stoichiometry lower than WO_1 [**10**]. Hence, in subsequent *in situ* process, the reduced lower tungsten oxide ($WO_{2.72}$) encapsulated by the fresh carbon layer also leads to its reduction to W. Because of higher affinity between fresh C and W atoms [**11**], diffusion and carburization process occur simultaneously in single step through unreacted W core [**12**] and results to form single phase of WC. The presence of lower tungsten carbide (W_2C) in spite of the presence of excess carbon in sample A600-02 (**figure 4.1(c)**) may be due to the C accumulation in the surface layer of the particles. It also signifies the lack of reaction time for the carburization reactions to take place. However, the disappearance of W_2C peak with the increase in reaction time in sample A600-10 (**figure 4.1(d)**) indicates that the final WC products might have transformed from W_2C ($W_2C+C \rightarrow 2WC$). Hence, the reduction and carburization of WO_3 at temperature 600 °C may occur through the reaction path ($WO_3 \rightarrow WO_{2.72} \rightarrow WO_2 \rightarrow W \rightarrow W_2C \rightarrow WC$). This path has also been reported by many authors with the appearance of some extra lower oxide(s) as intermediate products [**4, 13-15**]. The overall possible reactions that take place in the WO_3-C_3H_6O-Mg system can be proposed as follows:

$$3WO_3 + C_3H_6O + 5Mg \rightarrow WC + W_2C + 5MgO + CO_2 + 3H_2O \quad \text{(i)}$$

ΔH_{298} = -1548.32 kJ/mol, ΔG_{298} = -1567.76 kJ/mol

$$3WO_3 + C_3H_6O + 6Mg \rightarrow WC + W_2C + 6MgO + CO + 3H_2O \quad \text{(ii)}$$

ΔH_{298} = -1866.92 kJ/mol, ΔG_{298} = -1879.86 kJ/mol

According to free energy calculations, the *in-situ* reduction as well as carburization in reaction (ii) is thermodynamically spontaneous and highly exothermic. So, this reaction generates a lot of heat and results to increase the local temperature, which favors the whole reaction. Also, this indicates that theoretically at least, WC obtained through reaction (ii) is more stable as compared to reaction (i) and the gas product during reduction will be CO. The production of CO gas enhances the reduction as well as carburization rate of WO_3 [**4**], which leads to the formation of carbon coated WC (WC@C) nano composites. The entire mechanism of WC@C composite formation is illustrated in **figure 4.3**.

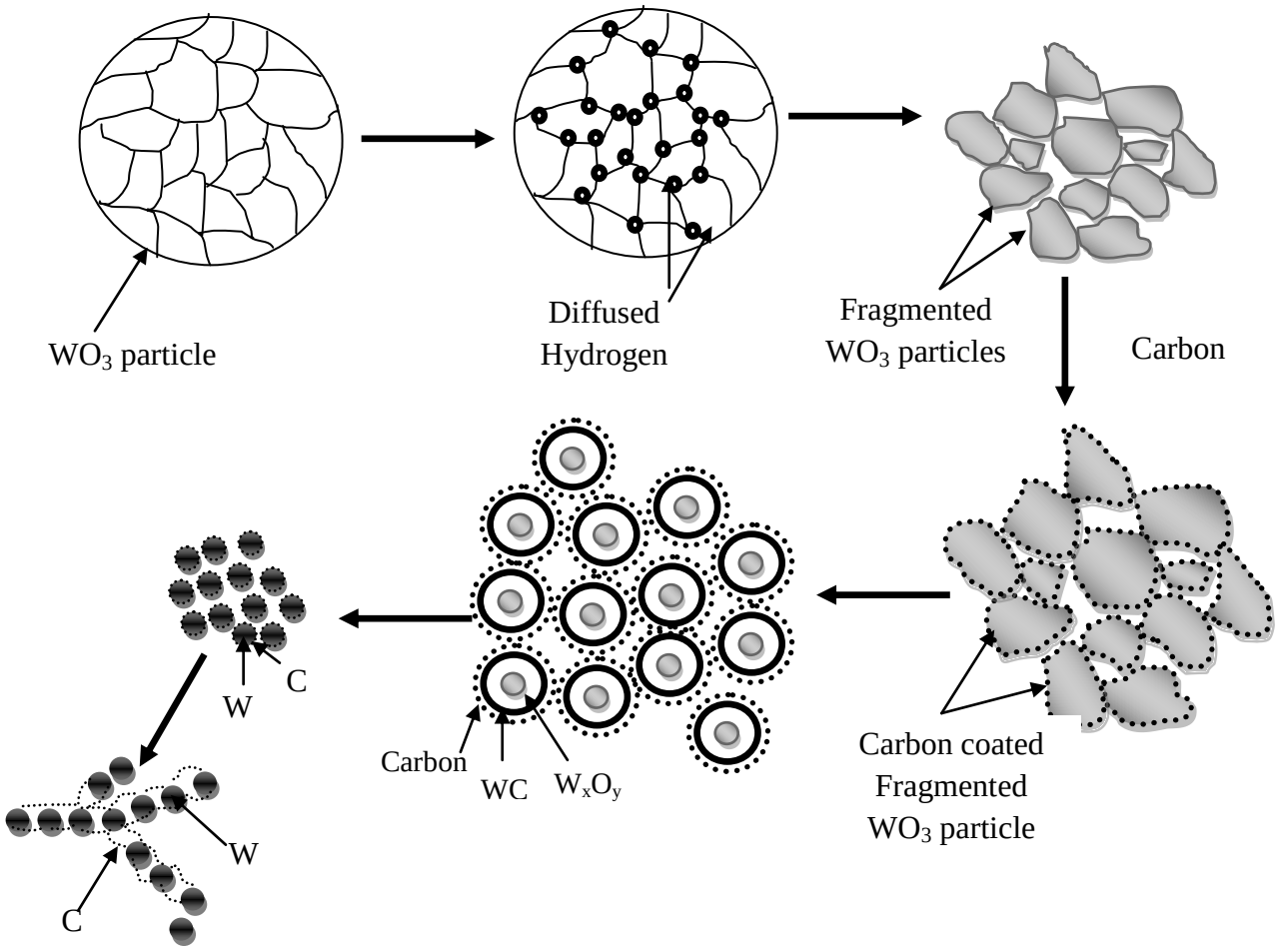

Figure 4.3: Schematic mechanism of WC@C nanoparticles formation.

4.1.1.3 Activated charcoal as carburizing agent

In further study of WC nano particle synthesis the activated charcoal in solid-state has been used as carburizing agent in this experiment. The mixture of WO_3 (1.157 g), Mg (2 g) and activated charcoal (2 g) were added into the autoclave. The samples obtained at different temperature and time are denoted as *CT-t*; where *C*, *T* and *t* corresponds to activated charcoal, reaction temperature (°C) and time (h).

Figure 4.4 shows the XRD patterns of the product phase(s) obtained at different temperatures and reaction time after acid leaching the samples. Tungsten-containing phases are identified using reference XRD patterns as WC (ICDD reference number 01-072-0097); W_2C (ICDD reference number 00-020-1315); W (ICDD reference number 00-001-1204), WO_2 (ICDD reference number 01-082-0728) and $WO_{2.72}$ (ICDD reference number 01-071-2450). The effect of time and temperature on the reduction/carburization of WO_3 via solid-state reactions has been observed clearly in **figure 4.4**. In order to understand the kinetics of

reduction as well carburization of WO_3 in the presence of solid carbon source, the reaction has been initiated at lower temperature (500 °C) for 10 h. **Figure 4.4(a)** display the peaks of WO_3, $WO_{2.72}$, WO_2 and W in the XRD pattern of sample C500-10, which gives a path way for the reduction of WO_3 as ($WO_3 \rightarrow WO_{2.72} \rightarrow WO_2 \rightarrow W$).

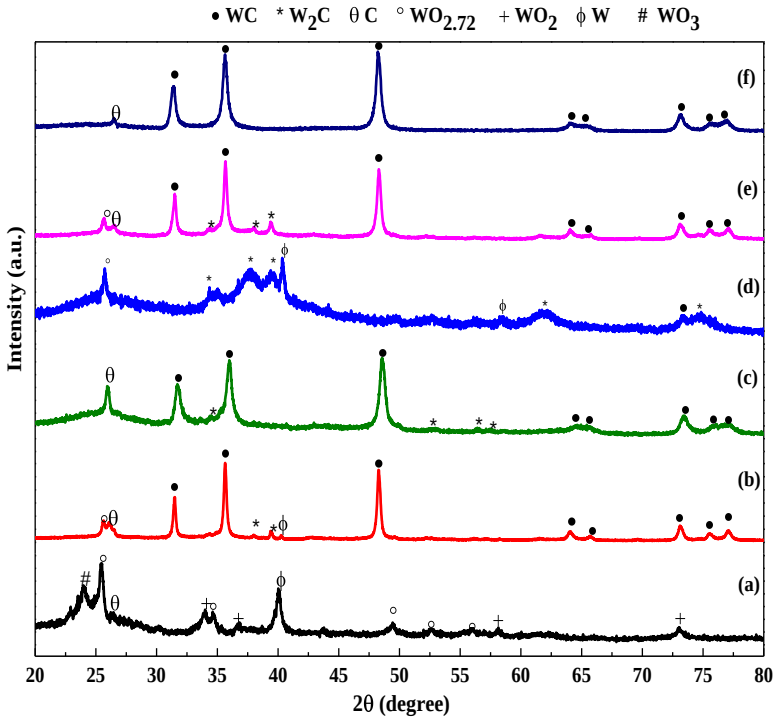

Figure 4.4: XRD patterns of synthesized samples **(a)** C500-10 **(b)** C600-02 **(c)** C600-10 **(d)** C600-15 **(e)** C700-10 and **(f)** C800-10.

As discussed earlier, the formation of intermediate lower oxides $WO_{2.72}$ and WO_2 attributes that such kind of metal oxide reduction will be very fast and occur in multi-step **[7]**. Further heating the mixture of ingredients at higher reaction temperature (600 °C) for short time 2 h reveals the complete reduction of WO_3 into lower oxide ($WO_{2.72}$) as well as the formation of higher content of WC phase as shown in **figure 4.4(b)**. This result shows that minimum temperature 600 °C is required for the initiation of carburization of WO_3 via solid-state reaction. With the increase in the reaction time to 10 h in sample C600-10 the minor peak of W_2C as impurity phase appeared in **figure 4.4(c)** due to the consistently reduction of $WO_{2.72}$ into W followed by carburization. In order to completely remove this impurity phase the reaction time has been increased to 15 h at the same temperature 600 °C. It results to display the peaks of lower oxide $WO_{2.72}$, W_2C and W in XRD pattern of sample C600-15 as shown in **figure 4.4(d)**. It is due to the occurrence of reversibility of carburization process at higher reaction time. So, to avoid the reversibility of carburization (decarburization) process

at higher reaction time, the reaction temperature has been increased to 700 and 800 °C at constant reaction time of 10 h. The XRD pattern of sample C700-10 as shown in **figure 4.4(e),** displays that the peak intensity of the impurity phases $WO_{2.72}$, W_2C and W got decreased. The peaks corresponding to these phases finally disappeared in sample C800-10 (**figure 4.4(f)**) and show the formation of single phase WC nano powder. Hence, it is clear that the pure phase of WC nano powder can be obtained at 800 °C with the holding time of 10 h via solid-state reaction in autoclave.

4.1.1.4 Thermodynamic analysis on series of reduction and carburization reactions

Generally, the change in Gibbs-free energy (ΔG) gives an idea for the spontaneous direction of the reduction/carburization process. After heating the mixture of tungsten oxide, magnesium and activated charcoal to certain temperature, several reactions will occur during the reduction as well as carburization. Hence, in order to analyze these transformations, the heat of reaction associated with each reaction is to be considered for calculating ΔG for respective reaction by the following equation:

$$\Delta G_T = \Delta H_{T_0} + \int_{T_0}^{T} C_P \, dT - T[\Delta S_{T_0} + \int_{T_0}^{T} \frac{C_P}{T} \, dT] \quad (4.1)$$

where $C_P = a + bT + cT^{-2} + dT^{-0.5}$ (4.2)

where C_p is specific heat capacity and *a*, *b*, *c* and *d* are the thermodynamic data of reactants and products at the standard state.

During the reduction of WO_3, it is reported by many authors **[2-4]** that different phases of tungsten oxide will form as an intermediate product before the final W phase obtained. Thermodynamically different solid-state reactions may occur during reactions of WO_3 with C and Mg as the temperature is increased. The corresponding most probable reactions associated with reduction of WO_3 to W and then carburization are given below:

$WO_3 + 0.28C \rightarrow WO_{2.72} + 0.28CO$ (iii)

$WO_3 + 0.14C \rightarrow WO_{2.72} + 0.14CO_2$ (iv)

$WO_3 + 0.28Mg \rightarrow WO_{2.72} + 0.28MgO$ (v)

$WO_{2.72} + 0.72C \rightarrow WO_2 + 0.72CO$ (vi)

$WO_{2.72} + 0.36C \rightarrow WO_2 + 0.36CO_2$ (vii)

$WO_{2.72} + 0.72Mg \rightarrow WO_2 + 0.72MgO$ (viii)

$$WO_2 + 2C \rightarrow W + 2CO \quad \text{(ix)}$$

$$WO_2 + C \rightarrow W + CO_2 \quad \text{(x)}$$

$$WO_2 + Mg \rightarrow W + 2MgO \quad \text{(xi)}$$

$$2W + C \rightarrow W_2C \quad \text{(xii)}$$

$$W_2C + C \rightarrow 2WC \quad \text{(xiii)}$$

$$W + C \rightarrow WC \quad \text{(xiv)}$$

The values of ΔG for all the above possible reactions can be calculated with the help of equation (4.1) at different temperatures by using the thermodynamic values mentioned in Ref. **[16]**. Most of the authors **[2, 4]** have reported the reduction of WO_3 by carbon at higher temperature range (600-900 °C). But magnesium being a highly reactive substance, also reacts with WO_3 to yield lower intermediate tungsten oxide phases as a solid-state reaction product(s). Because of lower ΔG (ΔG<0) value of reactions (v, viii, xi) through Mg reactant as compared to carbon reducing reactions, it acts as a best catalyst to enhance the reduction rate at lower temperature range (500 °C). The thermodynamic analysis of magnesium reduced tungsten oxide reactions is shown in **figure 4.5(a-c).** From thermodynamic study, it is clear that at 500 °C both magnesium (Mg) as well as carbon (C) play vital role in the reduction of WO_3 into lower intermediate oxide ($WO_{2.72}$) in 10 h reaction time as shown in **figure 4.4(a).** The formation of this oxide phase helps to decrease the reduction temperature as compared to temperature reported by **Koc and Kodambaka [2].** Because of higher ΔG value of all carbon reduced reactions at 600 °C in **figure 4.4(b & c)**, magnesium induced reduction process will dominate, which leads to reduce intermediate oxide ($WO_{2.72}$) into pure tungsten (W) through the formation of WO_2.

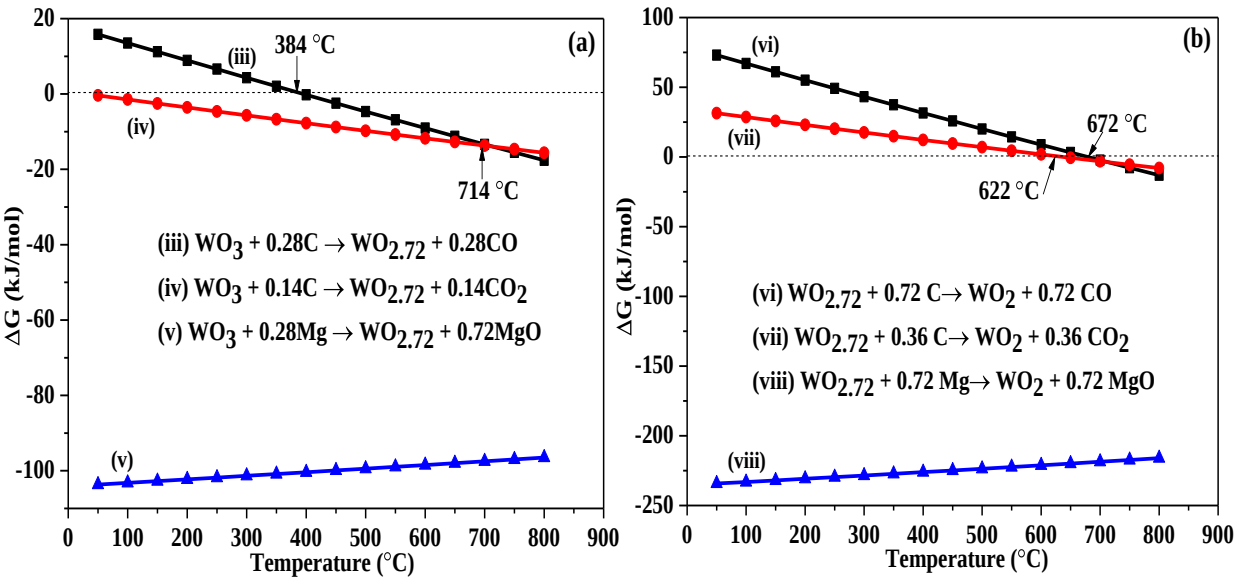

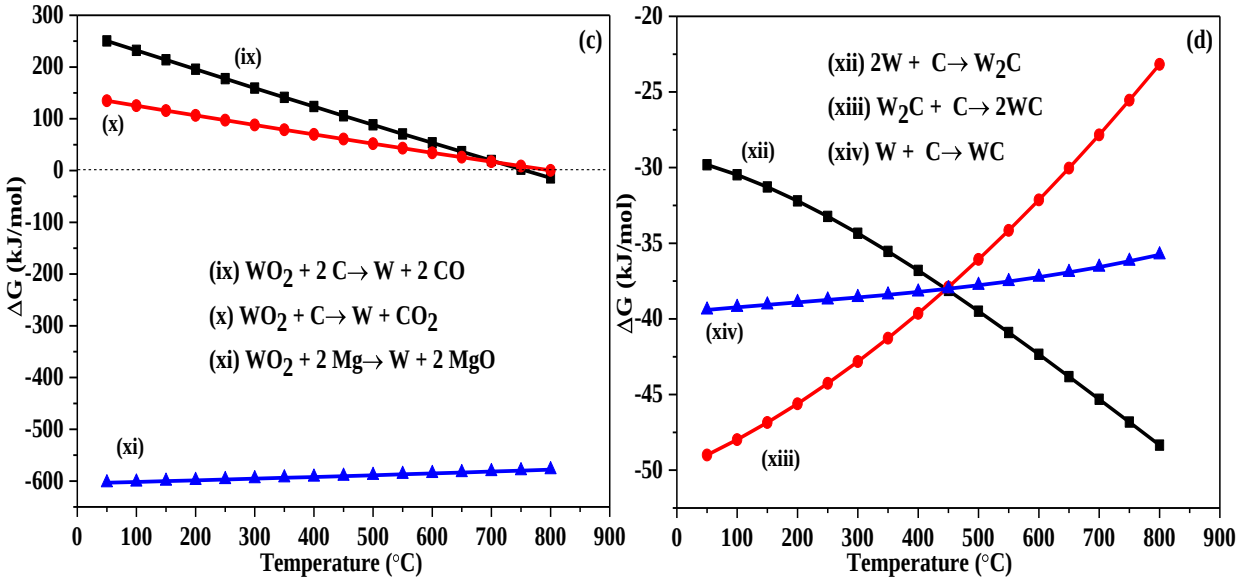

Figure 4.5: Change of ΔG with temperature of tungsten oxides of **(a)** WO_3 **(b)** $WO_{2.72}$ **(c)** WO_2 when reacting with carbon and magnesium and **(d)** change of ΔG during carbonization reactions.

Due to the greater affinity of C with the *in-situ* produced fresh W atoms, it will diffuse at faster rate through unreacted W core at 600 °C and form W_2C phase. Such kind of activity is confirmed by observing the lower ΔG value of reaction (xii) as compared to reaction (xiv) at 600 °C. While, on the other hand, the lower value of ΔG in reaction (xiv) as compared to reaction (xiii) attributes that freshly prepared W also reacts with carbon atoms and carburized directly into WC. One of the aspects has also been observed from the ΔG-T curve (**figure 4.5(b & c)**) that at synthesis temperature 700 and 800 °C, carbon also reacts with the metal oxide(s) and formed metallic phase (W) with the emission of CO_2 and CO gases as byproduct. This process has been confirmed by observing the lower value of ΔG at these temperatures (**figure 4.5(b & c)**).

From ΔG-T curve it has been observed that at temperature ~700 °C, the gas product for carbon reduced reactions will be CO_2 which transforms to CO with the increase in temperature up to 800 °C. It means that at distinct reaction temperatures, the same reactants can have different byproducts **[17]**. However, the ratio of CO and CO_2 play a very important role to decide the direction of carburization process. Hence, as compared to sample C600-10 a decrease in reaction rate for carburization has been observed in sample C700-10, which attributes that the reaction moves backward with the formation of W_2C phase. Moreover, the reoxidation can even takes place at a specific temperature in CO_2 rich reaction (CO_2/CO>0.1) **[4, 18]**. Hence, the appearance of $WO_{2.72}$ in XRD pattern of sample C700-10 (**figure 4.4(e)**)

indicates that the reaction at 700 °C occurs in the presence of CO_2 rich gas. With further increase in temperature, the ratio of CO_2/CO is going to decrease, because of which the reduction/carburization reaction goes in forward direction at 800 °C and increase the ratio of WC/W_2C. From thermodynamic analysis, it is clear that the reduction of WO_3 by magnesium corresponds to rise in *ΔG-T* curve with temperature, which may lead to the production of lower intermediate oxides and these oxides proved to be unstable at higher temperatures and react easily.

From the above discussion, it can be said that, all three tungsten oxides (WO_3, $WO_{2.72}$ and WO_2) can be reduced by magnesium as well as carbon at the temperature range of (500-800 °C) giving rise to the byproducts MgO, CO and CO_2 at different temperatures. All the above-mentioned reactions generate a lot of heat and results to an increase in the local temperature as indicated by lower calculated *ΔG* values with temperature. So, based on XRD and thermodynamic analysis, the route of reduction as well as carburization of WO_3 will be $WO_3 \rightarrow WO_{2.72} \rightarrow WO_2 \rightarrow W \rightarrow W_2C \rightarrow WC$ that may occur in a wide range of temperatures.

4.1.1.5 Hexane as carburizing agent

In this set of experiments, the reaction kinetics for the formation of pure phase of WC has been studied by using another hydrocarbon, (hexane) as carburizing agent. The mixture of WO_3 (2.314 g), Mg (2.304 g) and hexane (30 mL) have been used as reactants in the autoclave. The samples obtained at different reaction temperature and time are denoted as *HT-t* where *H*, *T* and *t* corresponds to hexane, reaction temperature (°C) and time (h), respectively.

Figure 4.6 shows the XRD patterns obtained after acid treatment of samples synthesized at temperature range of 500-800 °C. It shows the peaks of tungsten-containing phases identified using reference XRD patterns as WC (ICDD reference number 01-072-0097); W_2C (ICDD reference number 00-020-1315); W (ICDD reference number 00-001-1204), WO_2 (ICDD reference number 01-082-0728), $WO_{2.72}$ (ICDD reference number 01-071-2450), $WO_{2.625}$ (ICDD reference number 01-077-0810) and $WO_{2.76}$ (ICDD reference number 01-079-0171).

The presence of intermediate lower oxides $WO_{2.76}$, $WO_{2.72}$, $WO_{2.625}$ and WO_2 in **figure 4.6(a)** for sample H500-10 indicates the reduction of WO_3 into its lower oxides. As discussed earlier, such kind of reduction will be fast and multi-step, so with the increase in temperature to 600 °C for 2 h, the appearance of WC peaks was observed in **figure 4.6(b)**. But the

presence of minor peaks of oxide(s) in sample H600-02 attribute incomplete reduction/carburization process at this condition. Therefore, the synthesis time has been increased to 10 h by keeping the temperature constant (600 °C). The results obtained at this condition show the disappearance of $WO_{2.76}$ and $WO_{2.72}$ phase in **figure 4.6(c).** But still the presence of negligible peak intensity of $WO_{2.625}$ phase has been observed, which support the consistent reduction at this condition.

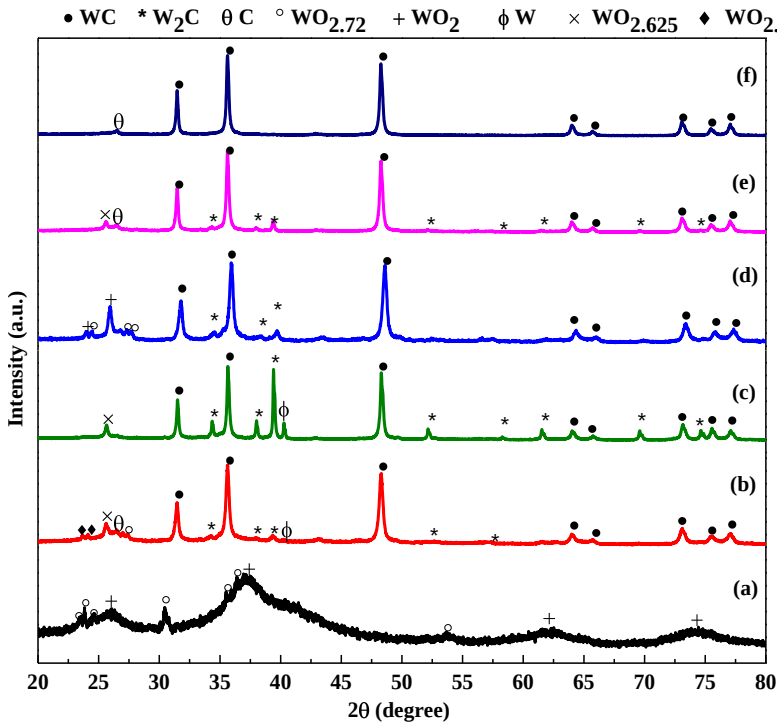

Figure 4.6: XRD patterns of synthesized samples **(a)** H500-10 **(b)** H600-02 **(c)** H600-10 **(d)** H600-15 **(e)** H700-10 and **(f)** H800-10.

By keeping this result in view the reaction time has been increased to 15 h. The XRD profile for this shows the appearance of $WO_{2.72}$ and WO_2 peak in **figure 4.6(d)**. This result attributes that at higher reaction time, due to the reversibility of reduction/carburization process the complete formation of WC could not take place. Hence, in order to avoid the reversibility, the reaction temperature has been increased to 700 °C for 10 h. The XRD profile under this condition for sample H700-10 is shown in **figure 4.6(e).** The presence of oxygen deficient tungsten oxide $WO_{2.625}$ phase in XRD profile for sample H700-10 attributes the favorable conditions of reduction. Finally the disappearance of all lower oxides as well as lower carbide phases at higher synthesis temperature of 800 °C in sample H800-10 (**figure 4.6(f)**) confirms the formation of pure phase of WC. Hence, the appearance of different peaks in XRD patterns gives a path way for the reduction as well as carburization of WO_3 as ($WO_3 \rightarrow WO_{2.76} \rightarrow WO_{2.72} \rightarrow WO_{2.625} \rightarrow WO_2 \rightarrow W \rightarrow W_2C \rightarrow WC$).

As discussed earlier, the kinetics of the carburization process essentially involves the decomposition of hydrocarbon and diffusion of carbon atoms into the reduced metallic phase (W). The Magnesium (Mg) being highly active element absorb oxygen from the autoclave atmosphere and convert into MgO. Moreover, the reaction inside the autoclave will be exothermic and the internally generated heats act as endothermic heat for the breaking of C-C and C-H bond. According to **Boyadjian et al. [19]**, the presence of MgO as a catalyst enhances the decomposition of hexane (C_6H_{14}) and breaking of C-C and C-H bond at relatively lower temperature. By assuming the homogeneous decomposition process of hexane, the possible formed species may be the C-containing intermediate complex compounds and different hydrocarbon gases like Methane (CH_4), Ethane (C_2H_6), Ethylene (C_2H_4) and Butane (C_4H_{10}) **[20]**.

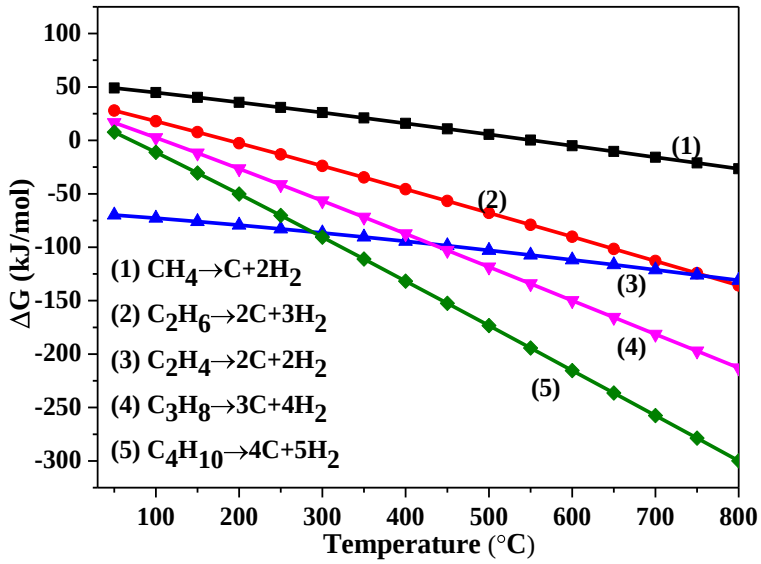

Figure 4.7: Change of ΔG with temperature during decomposition of hydrocarbon gases.

To analyze the decomposition of hydrocarbon(s) into lower species (C and H), ΔG for each probable reaction has been calculated at different temperatures by using equation (4.1) and (4.2) and plotted in **figure 4.7**. However, the ΔG-T curve shown in **figure 4.7** attributes lower ΔG value (ΔG<0) for the decomposition of C_2H_4 and C_4H_{10} gases. This result represent that the hexane may break initially into C_2H_4 and C_4H_{10}, which further decomposed into carbon and hydrogen. This *in situ* produced hydrogen and carbon further help to reduce and carburize WO_3 whose detailed mechanism is discussed earlier.

On comparing the results of XRD obtained by two different liquid hydrocarbon (C_3H_6O and C_6H_{14}), it is clear that both the reductant species (C and H) after the decomposition of hydrocarbon help to reduce as well as carburize the WO_3 easily. But the higher amount of carbon produced after the decomposition of hexane may delay the whole process of reduction/carburization due to the formation of thick carbon coating around the induced particles. The occurrence of fast reduction in case of acetone has also been confirmed from the appearance of lesser number of intermediates oxide(s) products as compared to hexane.

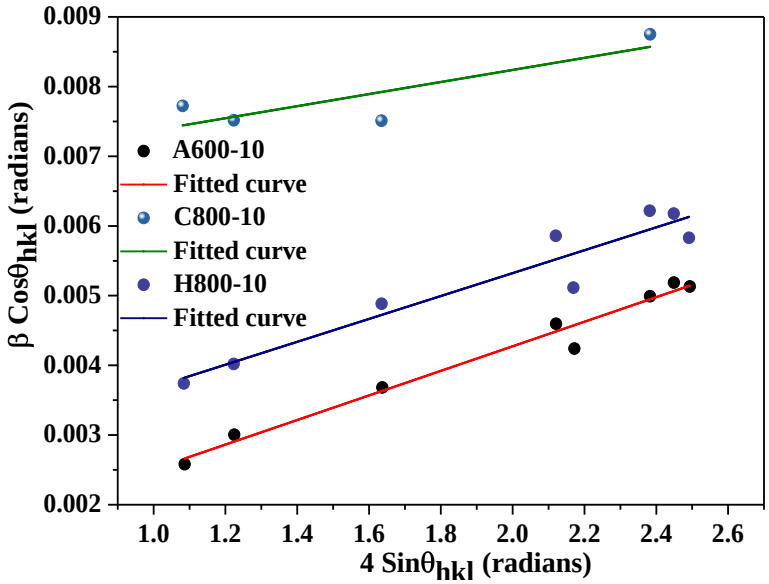

Figure 4.8: Williamson–Hall plot of samples **(a)** A600-10 **(b)** C800-10 and **(c)** H800-10 by assuming UDM.

From the broadened nature of XRD peaks, the strain and crystallite size for samples synthesized at different reaction conditions have been obtained by using Williamson-Hall's (W-H) equation (4.3) by plotting the value of $\beta_{hkl}\, Cos\theta_{hkl}$ as a function of $4Sin\theta_{hkl}$. The value of strain (ε) and the crystallite size (D) are estimated from the slope of the line as well as from the intersection with the vertical axis, respectively.

$$\beta_{hkl} Cos\theta_{hkl} = [K\lambda/D] + [4\epsilon Sin\theta_{hkl}] \qquad (4.3)$$

where β (2θ) is the full width at half maximum (FWHM), λ is the X-ray wavelength, D is the crystallite mean size and ε is strain. The peak position (2θ), integrated intensity, the peak maximum position and the peak width of the individual reflections is obtained through fitted Gaussian function. The above equation (4.3) represents the uniform deformation model (UDM) in which strain is assumed to be uniform in all crystallographic directions by considering the isotropic nature of the crystal.

The W-H plot by assuming UDM for the samples are shown in **figure 4.8** and the values obtained from this plot corresponding to strain and crystallite size are given in **table 4.1**. However, all the above discussions have been done after considering uniform strain in all directions of isotropic crystal. But, in most of the cases, the assumption of the homogeneity and isotropy is not fulfilled, so Uniform Stress Deformation Model (USDM) and Uniform Deformation Energy-Density Model (UDEDM) have been taken by assuming the cause of anisotropic micro strain ε_{hkl} to be uniform deformation stress σ. The generalized Hooke's law refers to the strain by keeping only the linear proportionality between deformation stress and strain as given by $\sigma = \varepsilon_{hkl}E_{hkl}$, where σ is the deformation stress of the crystal and E_{hkl} is modulus of elasticity.

This equation is just an approximation and is valid only for significantly small strain. With a further increase in strain, the particles deviate from this linear proportionality [**21**]. By considering this approach, the W-H equation (4.3) has the form:

$$\beta_{hkl}Cos\theta = \left(\frac{K\lambda}{D}\right) + \left(\frac{4\sigma Sin\theta}{E_{hkl}}\right) \tag{4.4}$$

where E_{hkl} is Young's modulus in the direction perpendicular to the set of planes (*hkl*). The uniform stress can be calculated from the slope line plotted between $4Sin\theta/E_{hkl}$ and $\beta_{hkl}Cos\theta$, and the crystallite size (D) from the intercept if E_{hkl} of hexagonal WC nanoparticles is known. For a sample with hexagonal crystal phase, Young's modulus E_{hkl} is given by the following relation [**22-24**]:

$$E_{hkl} = \frac{\left(h^2 + \frac{(h+2k)^2}{3} + \left(\frac{al}{c}\right)^2\right)^2}{s_{11}\left(h^2 + \frac{(h+2k)^2}{3}\right)^2 + s_{33}\left(\frac{al}{c}\right)^4 + (2s_{13} + s_{44})\left(\left(h^2 + \frac{(h+2k)^2}{3}\right)\left(\frac{al}{c}\right)^2\right)} \tag{4.5}$$

where s_{11}, s_{13}, s_{33}, s_{44} are the elastic compliances of tungsten carbide (WC) with values of 1.55×10^{-3}, 0.191×10^{-3}, 1.087×10^{-3} and 3.25×10^{-3} GPa^{-1} respectively [**25**].

Young's modulus E for hexagonal tungsten carbide (WC) is calculated as ~791 GPa, which is in close approximation as reported earlier by **El-Eskandarany** [**26**]. The W-H plot assuming USDM is shown in **figure 4.9**. Since in many cases, the assumption of homogeneity and isotropic is not fully justified so there is another model UDEDM, that has been taken into account. It assumes the cause of lattice strain to be density of deformation energy u (energy per unit volume).

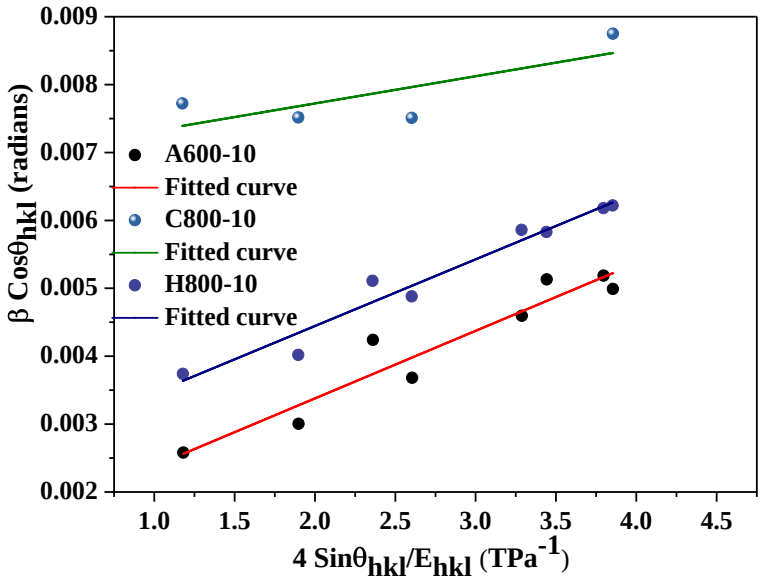

Figure 4.9: The modified form of W–H analysis assuming USDM for samples **(a)** A600-10 **(b)** C800-10 and **(c)** H800-10.

According to Hooke's law the energy density can be calculated by using a relation $u = (\varepsilon^2 E_{hkl})/2$. So, equation (4.4) can be written as

$$\beta_{hkl} Cos\theta = \left(\frac{K\lambda}{D}\right) + \left(4Sin\theta\left(\frac{2u}{E_{hkl}}\right)^{1/2}\right) \qquad (4.6)$$

The anisotropic energy density u and crystallite size (D) is estimated form the slope and intercept of fitted line between $\beta_{hkl} Cos\theta_{hkl}$ and $4Sin\theta(2u/E_{hkl})^{1/2}$ as shown in **figure 4.10**.

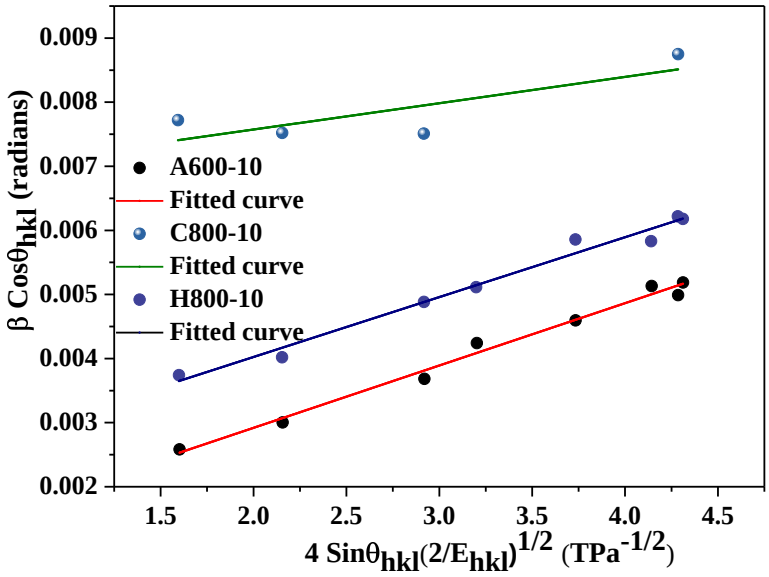

Figure 4.10: The modified form of W–H analysis assuming USEDM for samples **(a)** A600-10 **(b)** C800-10 and **(c)** H800-10.

The deformation stress and deformation energy density are related as $u = \sigma^2/2E_{hkl}$. So, clearly both the equations (4.4) and (4.6) are considering the anisotropic nature of elastic constant, so they are essentially different. Hence, W-H plots using equation (4.4) and (4.6) for a given sample may result different value of lattice strain and crystallite size. The results obtained from USDM and UDEDM are summarized in **table 4.1**.

From the calculated value of ε, it is clear that the synthesized samples are in the strained form. The positive value of strain clearly indicates the existence of tensile strain, which results to induce lattice expansion in the samples [**27**]. It may arise due to the transformation of lower ionic radii ion (0.6 nm) W^{6+} to higher ionic radii (0.66 nm) W^{4+} during the formation of WC nano powder. Since, the lattice strain in any material indicates the disorderness in the system so, it is responsible for its higher activity. Moreover, **Lewin et al.** [**28**] also correlated the crystallite size with lattice parameter of unit cells. According to them, the decrement in the crystallite size leads to increase in the electron deficiency per metallic (Me)-atom and results to gradually weakens the Me-C bonds. It leads to an increased lattice parameter which results to an increase in the lattice volume with reduced crystallite size which is also observed in respective samples. For the evaluation of unit cell volume, the lattice parameters are calculated by using (001) and (100) peaks in the XRD patterns.

Table 4.1: The data obtained from XRD analysis of the samples A600-10, C800-10 and H800-10.

		A600-10	C800-10	H800-10
UDM	$\varepsilon\times10^{-3}$	1.79	1.05	1.76
	D (nm)	59	17	41
USDM	$\varepsilon\times10^{-3}$	1.39	0.55	1.37
	D (nm)	98	19	55
	σ (GPa)	0.995	0.400	0.981
UDEDM	$\varepsilon\times10^{-3}$	1.62	0.68	1.56
	D (nm)	141	20	63
	σ (GPa)	1.165	0.491	1.119
	$u\times10^3$ (kJ/m^3)	0.945	0.168	0.872
Volume of unit cell (Å^3)		20.72	20.84	20.80

Moreover, from the observed USDM and UDEDM, it has been concluded that after considering non uniformity in the crystal of the samples, the strain is minimum in WC lattice of sample C800-10 as compared samples A600-10 and H800-10. It may be due to the distortion arising in the system during the defragmentation of WO_3 due to *in-situ* produced hydrogen gas in liquid hydrocarbon source. While in case of sample C800-10, no such kind of activity occur for the reduction of WO_3 due to which the strain is minimum in this sample. Moreover, due to the interaction of hydrogen with metallic oxide after the decomposition of hydrocarbon, the induced steam inside the metallic oxide is highly responsible for the crystallinity in the samples A600-10 and H800-10 and results to increase the crystallite size.

4.1.2 Thermal Analysis

Among all the synthesized samples using different carbon sources and synthesis conditions, the thermal analysis has been done only for selected samples in which pure phase of WC was obtained. It is clear from the TGA plot (**figure 4.11)** that for all the selected powder samples the weight decreases continuously during heating. The rate of weight loss observed to be quite low below ~425 °C and high above 500 °C. However, the loss of weight slows down beyond the temperature 700 °C for all samples. The reduction in weight below 425 °C may be due to the presence of moisture and some functional group available on the surface of carbon **[29]**. Afterwards, the oxidation of free carbon and carbon coated WC nano particles begin, which transforms WC into WO_3. However, the plateau after ~700 °C indicates that all carbon and carbon coated WC (WC@C) nano particles have been oxidized leaving only stable WO_3. This kind of behavior in TG curve has also been observed by many authors in their own systems **[30, 31]**.

Further, the sample composition is also calculated from the final mass change by assuming the presence of WC and freshly prepared elemental carbon in the sample **[29]**. The fraction of carbon present in the final synthesized powder is calculated as follows:

$$Free\ C\ (\%) = 100 \times \left(1 - \frac{m_f}{m_i} \times \frac{MW_{WC}}{MW_{WO_3}}\right) \quad (4.7)$$

where m_i and m_f are the initial and final masses observed from the TGA experiment, respectively; MW_{WC} and MW_{WO3} are the molecular weights of WC and WO_3, respectively. The results obtained from the calculation are summarized in **table 4.2**:

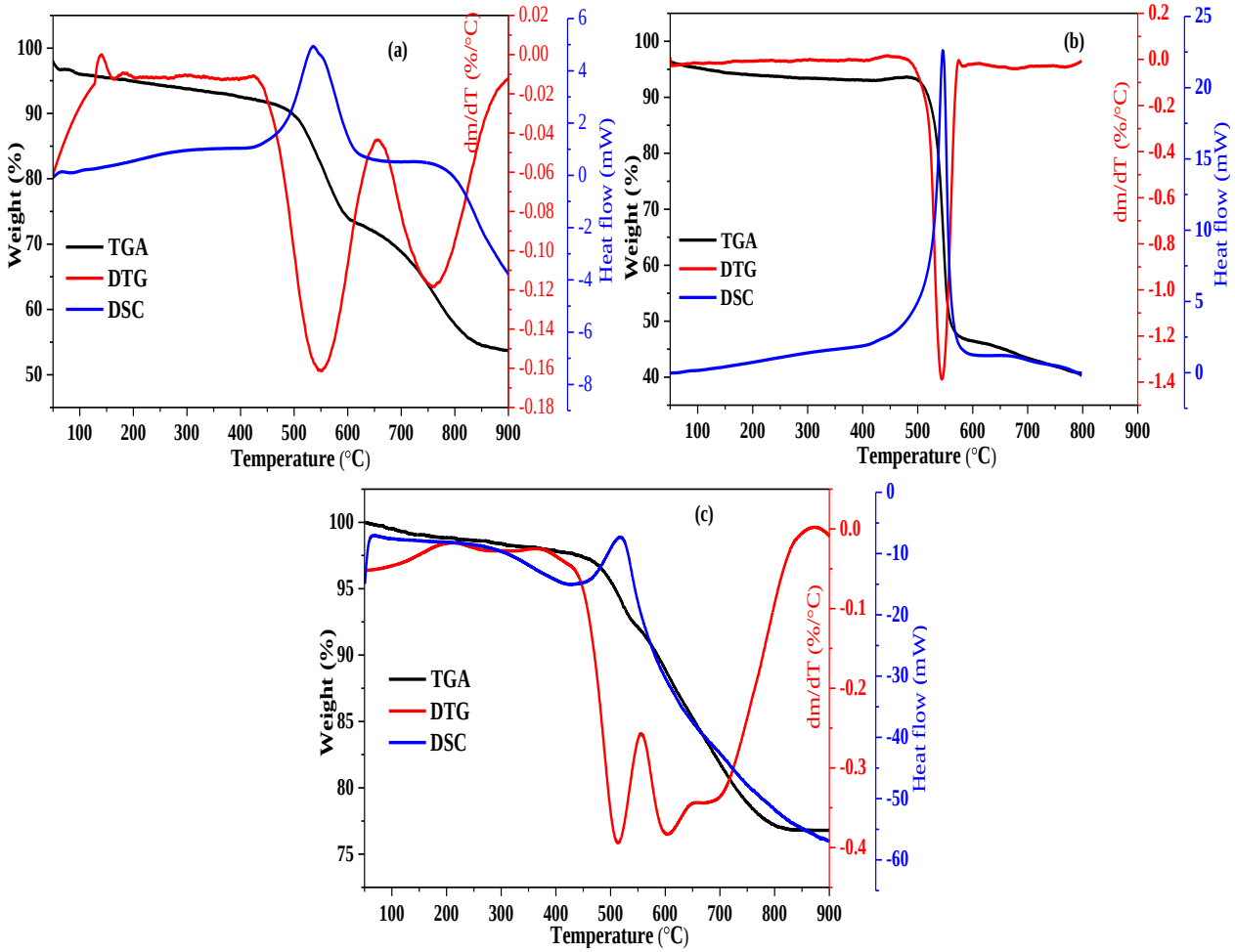

Figure 4.11: TG, DSC and DTG results of samples **(a)** A600-10 **(b)** C800-10 and **(c)** H800-10.

Furthermore, the starting of weight loss is an indication of carbide oxidation with the formation of CO_x (x=1, 2). So, the TG curves in **figure 4.11** reflects the stability of the carbon coated carbide nano particles, by observing the shifting of onset temperature for oxidation on the higher side for the sample C800-10. It may be due to either strong Me-C bonding or the presence of oxide/carbon content on the particle surface in the form of thick/thin layer, which restricts the further oxidation and delaying the oxidation process. Moreover, the presence of higher value of strain (**table 4.1)** in samples obtained by liquid hydrocarbon (A600-10 and H800-10) also initiates their oxidation earlier with temperature. The absence of sharp weight loss in TG curves for samples A600-10 and H800-10 indicates the formation of oxide layer during heating, which may act as a protective layer against further oxidation.

Table 4.2: Data obtained from TGA thermo-gram of the synthesized samples.

Sample	DSC peak (°C)	Free C (%)	WC content (%)	ΔH (kJ/g)
A600-10	534	56	44	-3.32
C800-10	546	65	35	-7.81
H800-10	516	35	65	-2.56

Moreover, the presence of peaks in DSC curve in the temperature range 500-550 °C attributes the onset temperature for the oxidation of powder samples. The appearance of peaks confirms that the process of oxidation is highly exothermic. It generates a lot of heat which can be calculated from the total area enclosed by the thermal analysis of DSC peak and the results of obtained ΔH corresponding to area has been mentioned in **table 4.2**. The higher value of ΔH for sample C800-10 attributes the complete combustion of carboneous elements at specific temperature, which also support to the sharpness in the peak. In contrary, the results of ΔH for samples obtained by liquid carbon source reveals that the carboneous elements take some time to oxidize which is reflected from the broadness of exothermic peak. Moreover, the shifting in the peaks also depends on the amount of free carbon present in the final product. Hence, the exothermic peak at higher temperature for sample C800-10 reveals the presence of higher amount of carbon in the obtained sample as mentioned in the **table 4.2**. While the sharp peak in the samples attributes the presence of fine size of carbon powder in the product.

All the process occurred with thermal treatment have also been confirmed by the appearance of multiple peaks in derivative thermo-gravimetric (DTG) analysis. The presence of DTG peaks **(figure 4.11)** at 550, 543 and 510 °C corresponding to samples A600-10, C800-10 and H800-10, respectively designates the oxidation of carbide. The appearance of peaks at these temperatures attributes the maximum weight loss due to the removal of carbon. Further, the appearance of the DTG peak at temperature 760 °C and 600 °C for samples A600-10 and H800-10 respectively indicates the delay in weight loss due to the formation of oxide layer during heating on the surface of product. The single step oxidation process has been designated by the sharp weight loss supported by single DTG peak in sample C800-10 as shown in **figure 4.11(c)**. Moreover, the resultant loading of WC in all the obtained samples

by this analysis is observed to be higher than the WC@C nano composites as reported by Yan et al. **[31]**.

4.1.3 BET surface area analysis

Since the catalytic activity of any material depends upon surface area and its pore texture [**32**], so the N_2 adsorption–desorption technique has been used to determine textural properties of the synthesized powder samples. As per our earlier discussion, the samples are synthesized in the presence of *in-situ* produced CO gas, so it will provide an excess carbon layer on WC nano particles **[33, 34]**.

Due to the presence of carbon layers on carbide nano particles, samples may have suitable porous structure and high surface area due to which the N_2 adsorption/desorption isotherm of samples exhibit typical IV curve in **figure 4.12**. These curves designate the characteristics of materials, which contain mesoporosity and attain high energy of adsorption (type IV) [**35**]. The isotherms observed in the N_2 adsorption/desorption isotherm (**figure 4.12**) for the synthesized samples revealed a distinct hysteresis loop of H3 type. This hysteresis are usually found for the solids consisting of aggregates or agglomerates of particles forming slit shaped pores with non-uniform size and/or shapes [**36**]. As observed from **figure 4.12,** the increment in the adsorption curve at relative pressure lowers than 0.1 attributes the presence of micropores in sample C800-10.

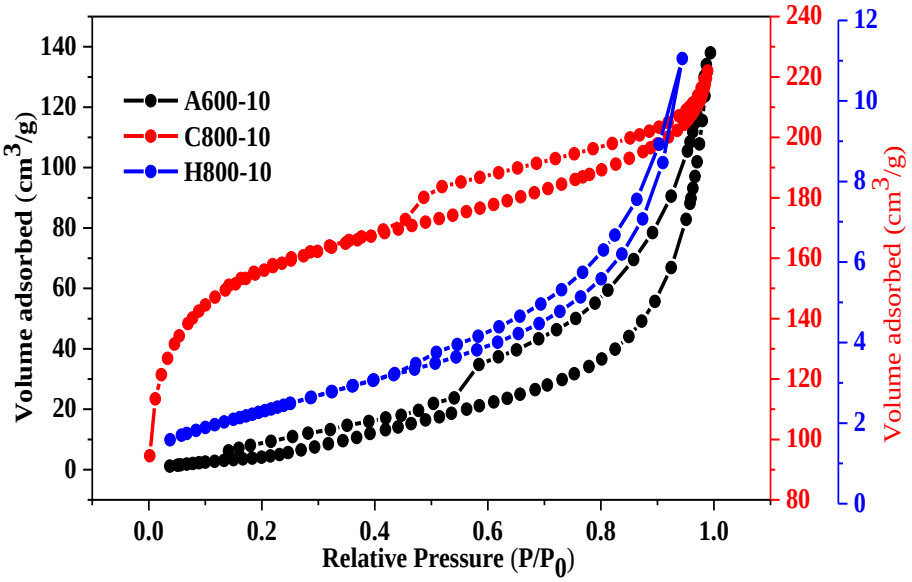

Figure 4.12: N_2 sorption isotherms of samples **(a)** A600-10 **(b)** C800-10 and **(c)** H800-10.

The observed value of BET specific surface area for all samples seems to be higher than that of estimated from particle size analysis, which is also observed by **Liu et al. [37]**. This is attributed due to the combined effect of morphology and porous structure of outer carbon layer on WC nanoparticles which significantly increases the specific surface area of WC@C **[38]**. The BET surface area of WC@C powder sample obtained from current synthesis method is comparable to value as reported by other methods **[39, 40]**, which makes it suitable material for electrochemical applications. **Figure 4.13** shows the typical pore size distribution curves of the synthesized samples. This shows that the samples have narrow pore size distribution in the range of 3 to 5 nm. The presence of pore size less than 2 nm is also showing the presence of micropores in the sample C800-10. The pore size, specific surface areas and pore volumes of the synthesized nano samples from N_2 adsorptions are mentioned in **table 4.3**. In the pore size distribution curve, the peak around pore diameter 4 nm shows the presence of mesopores in the samples. Its existence may be due to the stabilization in the outer surface of the synthesized samples. As shown in the **table 4.3**, the sample synthesized by solid carbon source (C800-10) has higher specific surface area and larger pore volume. But, in the case of samples synthesized by liquid carbon source (A600-10 and H800-10) the graphitization of outer carbon layer tends to decrease the micropores and mesoporous which results to decrease the surface area and pore volume **[41, 42]**.

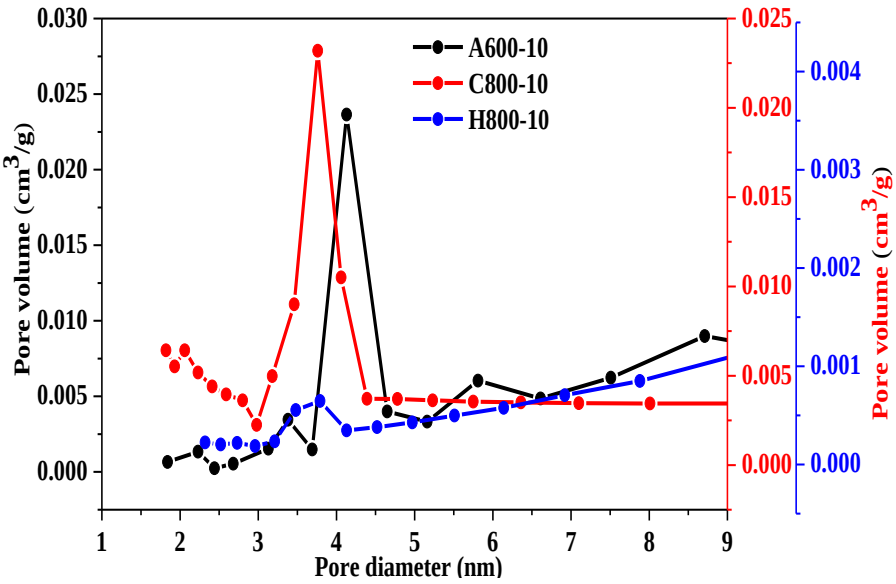

Figure 4.13: Pore size distribution of samples **(a)** A600-10 **(b)** C800-10 and **(c)** H800-10.

Table 4.3: Structure parameters of samples obtained from N_2 sorption isotherms.

Sample	A600-10	C800-10	H800-10
BET (m^2/g)	22.4	522.5	8.4
Total pore volume (cm^3/g)	0.213	0.343	0.017
Average pore diameter (nm)	10.5	2.6	8.4

4.1.4 Raman analysis

Figure 4.14 shows the Raman spectra for the synthesized nano powder A600-10, C800-10 and H800-10 to investigate the degree of graphitization and content of defects in the carbon materials present in the synthesized samples. The most common and important bands appearing in samples are D-band around 1350 cm^{-1} and G-band around 1580-1600 cm^{-1} **[43, 44]**. According to **Ferrari and Robertson [44],** the D-band is often attributed to disorder scattering, and this mode remains absent in perfect graphite. Whereas the G-band is associated with the I^{st} order scattering of E_{2g} mode of graphite. Both G and D-bands undergo significant changes upon amorphization of graphite as amorphous carbon contains a certain fraction of sp^3 carbons [**44**]. A universal observation is that higher disorder in graphite leads to a broader G-band, as well as to broad D-band of higher relative intensity compared to that of the G-band. The position of G-band at 1601 cm^{-1} in case of A600-10 (**figure 4.14(a)**) is related to the tangential stretching mode of all pairs of sp^2 atoms [**45**] and the D-band at 1342 cm^{-1} are associated with the structural defects and impurities.

It has been observed that the shifting of G-band from 1601 to 1585 cm^{-1} for samples C800-10 and H800-10 attributes defects/disordering in the graphitic cluster [**46**]. The data obtained from peaks fitting are summarized in **table 4.4**. The transition of ordering for sample A600-10 to disorder in sp^2-C phase for sample C800-10 and H800-10 indicates the ordering in the shrinking core with increased distortion in the outer layer **[44]**. This effect also enhances the reactivity of outer carbon layer with atmosphere that tends to react with oxygen easily to oxidize, which is also confirmed from the lower oxidation onset value of H800-10 (**table 4.2**).

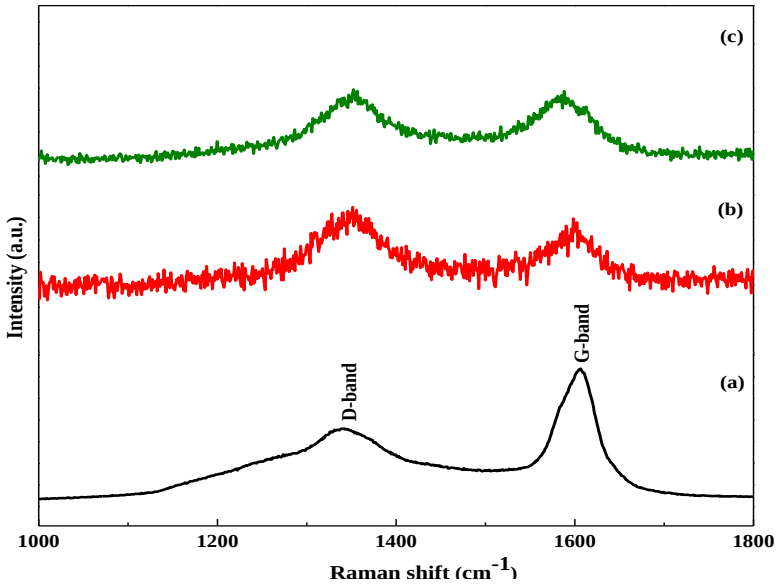

Figure 4.14: Raman spectra results of samples **(a)** A600-10 **(b)** C800-10 and **(c)** H800-10.

It designates that ordered sp^2-C graphitic phase cluster exists around the WC nano particles in sample A600-10 and it became thermodynamically stable as compared to H800-10. Moreover, ordered sp^2-C phase in the form of layered structured also assembles to the onion like structure in sample A600-10 whose discussion will be done in microstructure analysis section [**47**]. The presence of such kind of structure (onion structure) in sample A600-10, results to maximum weight loss at higher temperature (550 °C) which has been discussed in TGA analysis earlier [**47**]. Moreover, the existence of G-band position at higher wave number (1601 cm^{-1}) also supports to the formation of graphitic sheets around the WC nano particles in sample A600-10 [**46**] which is shown in TEM images which are discussed later. Since, the level of graphitization has decided the resistance against oxidation which is minimum for amorphous carbon. So, the idea about this feature has been determined by the intensity ratio between the D-band and G-band (I_D/I_G), which also provides information about the structural ordering of sp^2-phase [**47**].

The lower value of I_D/I_G for sample A600-10 ascribed the formation of higher graphitization among the obtained samples. While, on the other hand, the higher value of I_D/I_G in sample C800-10 and H800-10 designates the appearance of more defects, which results to lower the graphitization in the sample on changing the carburizing agents. Hence, this may be the reason of shifting of peak corresponding to maximum weight loss in DTG curve in **figure 4.11 (b & c)** towards lower side for sample C800-10 and H800-10.

Table 4.4: Raman characteristics of samples obtained from different carbon sources.

Sample	A600-10	C800-10	H800-10
D-band (cm^{-1})	1342	1348	1350
G-band (cm^{-1})	1601	1596	1585
I_D/I_G	0.32	1.40	0.79

4.1.5 Microstructure analysis

Morphological characteristics of the samples were analyzed by TEM/HRTEM analysis. The TEM images in **figure 4.15(a & c)** shows the carbon coated carbide nano particles in the form of core-shell morphology which has been observed by many authors in their work for the carbide systems **[48, 49].** These synthesized nano particles are composed of internal core with dark shade and external layer with light shade. This outer layer with light shade of the prepared sample is of carbon as has been also observed by **Zhong et al.** [**48**]. Further HRTEM of samples especially synthesized with liquid hydrocarbons also reveals that the outer layer is of graphitic carbon, which is also confirmed by the *d*-spacing between the carbon layers. This graphitic carbon layer in the form of onion type is clearly visible in the inset of **figure 4.15(a)** formed due to the ordering of carbon as discussed in Raman analysis.

The lattice spacing of WC in the inner core of synthesized samples observed from HRTEM can be clearly seen and the *d*-spacing value of 0.18, 0.28 and 0.25 nm belongs to the (101), (001) and (100) reflections of WC phase, respectively. Hence, it is evident that the outer nano chains are made of graphitic carbon except for sample synthesized by activated charcoal. So it is clear that sphere like nano particles are not uniformly dispersed but arranged into chainlike nanostructure. These nanochains consist of two parts; the interior WC nanoparticles encapsulated by outer carbon layer (graphitic carbon/amorphous carbon) namely core-sheath nanostructures. According to **Xi et al.** [**50**] there are two factors which are responsible for such kind of core-sheath nanostructures. One is the template effect of the tungsten carbide nanoparticles and the other is the activated effect of intermediary formed magnesium oxide nanoparticles. Further, on comparing the TEM obtained from two different liquid hydrocarbons it is clear that particle attained spherical shape for acetone and cubic shape for hexane. Such kind of change in the morphology in carbide particles on changing the hydrocarbon has also been observed by **Grove et al. [51]** in their system. As observed from

TEM images in different direction the average size of the prepared WC nano particles is in the range of 21 nm, 70 nm and 75 nm for samples obtained from acetone, activated charcoal and hexane as carbon source respectively. The effect of fragmentation of particles due to hydrogen diffusion seems dominating factor for the lower size of obtained particles by using acetone as carburizing agent. While on the other hand the observed higher size of WC nano particles obtained in sample H800-10 may be due to the influence of higher synthesis temperature.

The SAED patterns has been obtained for the samples (A600-10 and C800-10) containing WC nano particles having hexagonal structure and shown in **figure 4.15(g & h)**. The spots in the diffraction patterns for samples A600-10 and C800-10 show the reflections of crystalline phase of WC which is in agreement with XRD result.

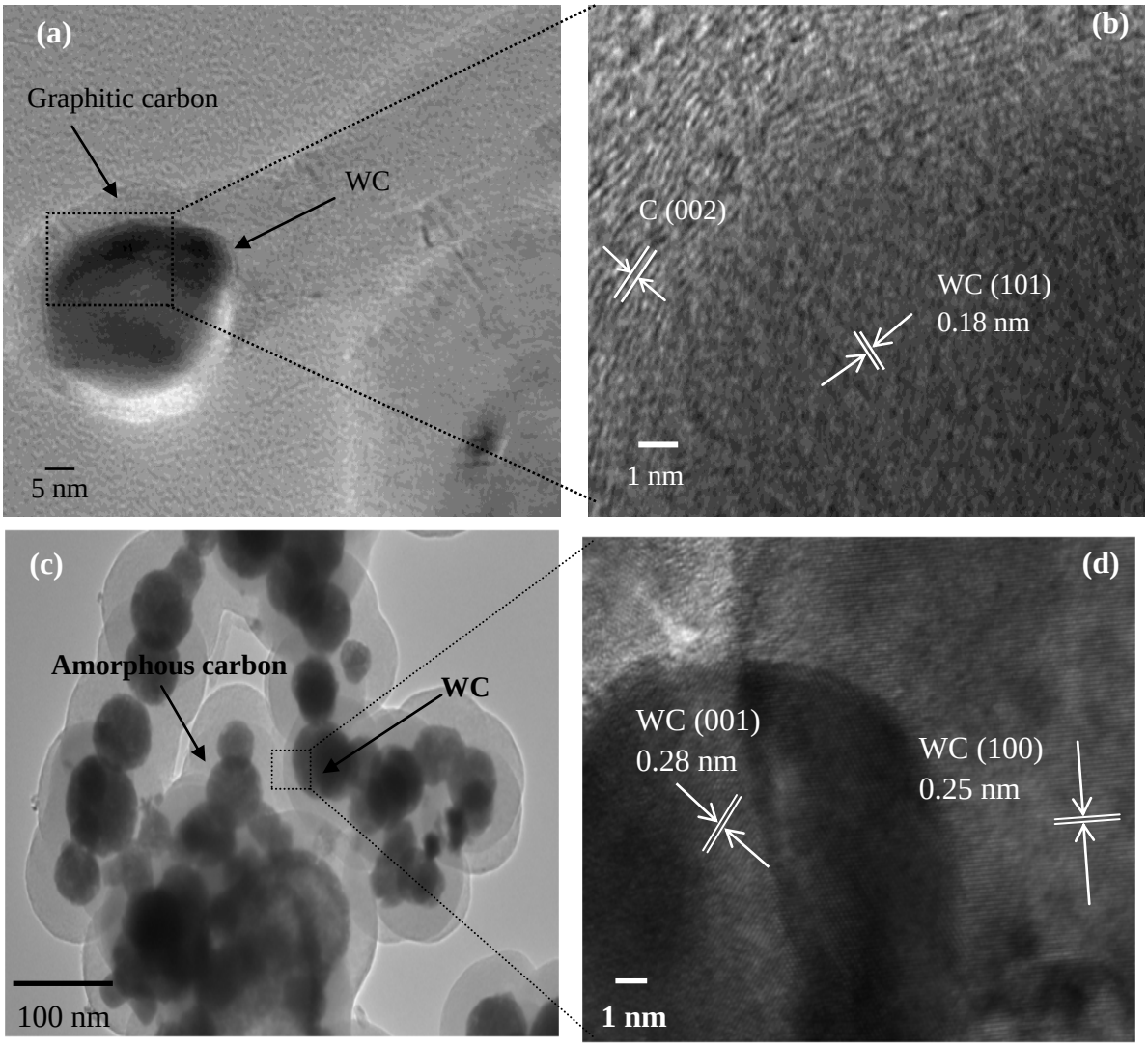

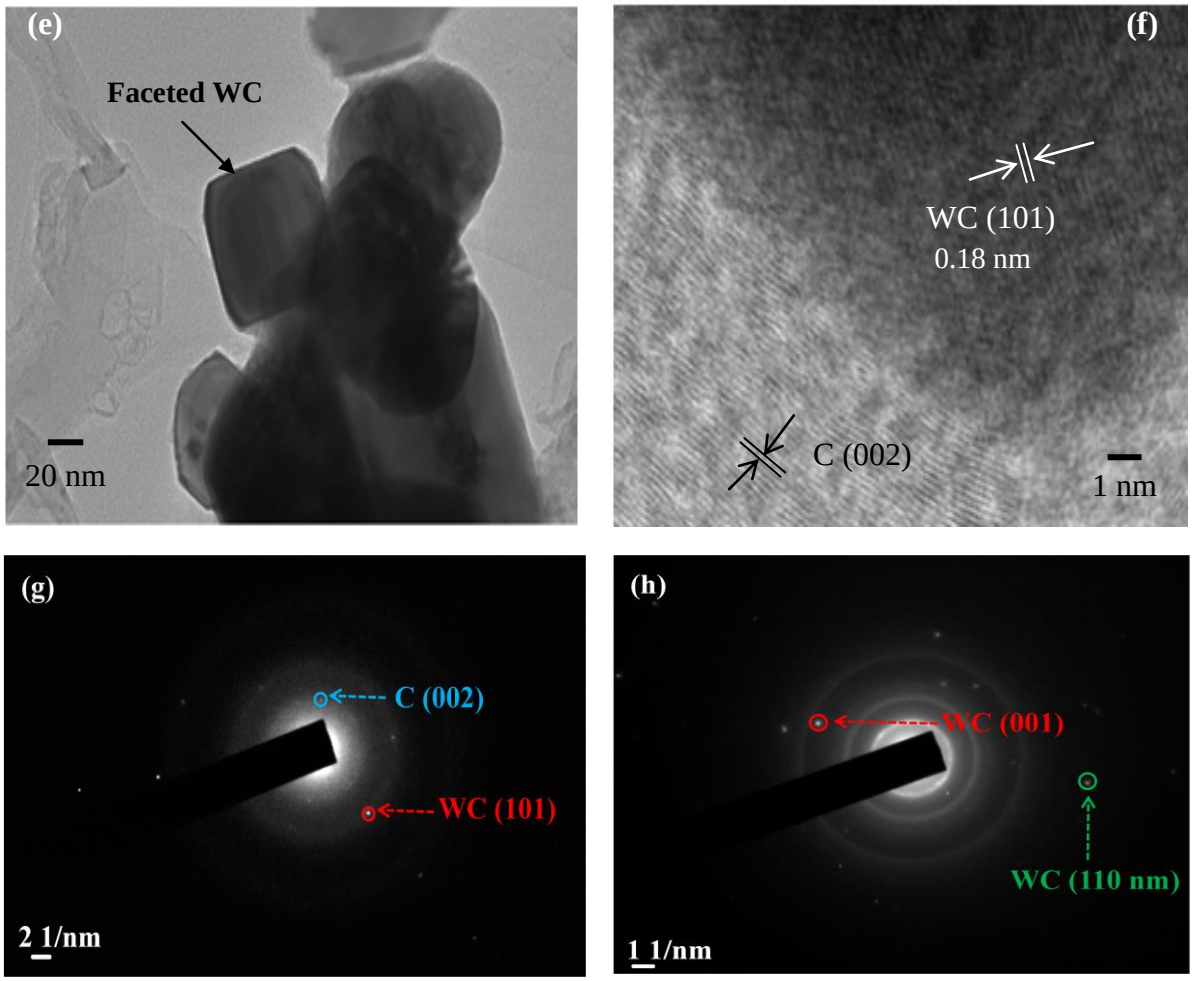

Figure 4.15: TEM/HRTEM images of WC@C samples **(a,b)** A600-10 **(c,d)** C800-10 **(e,f)** H800-10; SAED patterns of **(g)** A600-10 and **(h)** C800-10.

In the earlier part, extensive studies have been performed on the synthesis and characterization of tungsten mono-carbide (WC) nano powder. Since not much work is reported on the synthesis of tungsten semi-carbide (W_2C) so, in the successive part, we will focus on the reduction and carburization of metal oxide into the tungsten semi-carbide (W_2C). In this work, magnesium (Mg) metal powder is used as reducing agent, with three different carbon sources acetone, activated charcoal and hexane. In ordered to obtain tungsten semi-carbide (W_2C), initially the optimization of temperature, time and carbon amount has been done by taking acetone and activated charcoal as a carbon source. The samples obtained at different temperatures, different time and carbon source amount were denoted as *A/C/HT-t-a*, where *A*, *C* and *H* corresponds to acetone, activated charcoal and hexane carbon source respectively; *T*, *t* and *a* corresponds to temperature, time and amount of carbon source. However, the whole experiments have been carried out with air quenching the autoclave to provide less time for the diffusivity of carbon atoms. The results of different characterizations obtained by using different carbon sources are discussed below:

4.2 Synthesis of tungsten semi-carbide (W_2C)

4.2.1 X-ray diffraction analysis (XRD)

4.2.1.1 Acetone as carburizing agent

Figure 4.16 shows the X-ray diffraction patterns after acid treatment of the samples A575-2-10, A600-2-10, A615-2-10, A625-2-10 and A700-2-10, which were obtained by taking 10 mL of acetone at different temperatures for 2 h holding time. The three most intense peaks of patterns with 2θ values at 31.5°, 35.7°, 48.4° correspond to the plane of WC (001), (100) and (101) respectively according to ICDD reference number 01-072-0097. However, the diffraction peaks obtained with 2θ values at 34.4°, 38.1° and 39.5° could be assigned to the planes of W_2C (002), (200) and (102) respectively according to ICDD reference number 00-020-1315. A minor peak with *2θ* value of 40.4°, indicates the presence of pure W (ICDD reference number 00-001-1204) nano crystalline phase produced during the reduction of WO_3.

The presence of peak at 2θ~26.45° corresponds to the graphitic carbon (GC), which represents its crystalline nature. However, some amorphous carbon (AC) is also present in the obtained samples whose existence is revealed by the appearance of peak at *2θ*~25.75° **[52]**. It

appears due to the fast quenching of the autoclave which provides it less time to attain crystalline behavior.

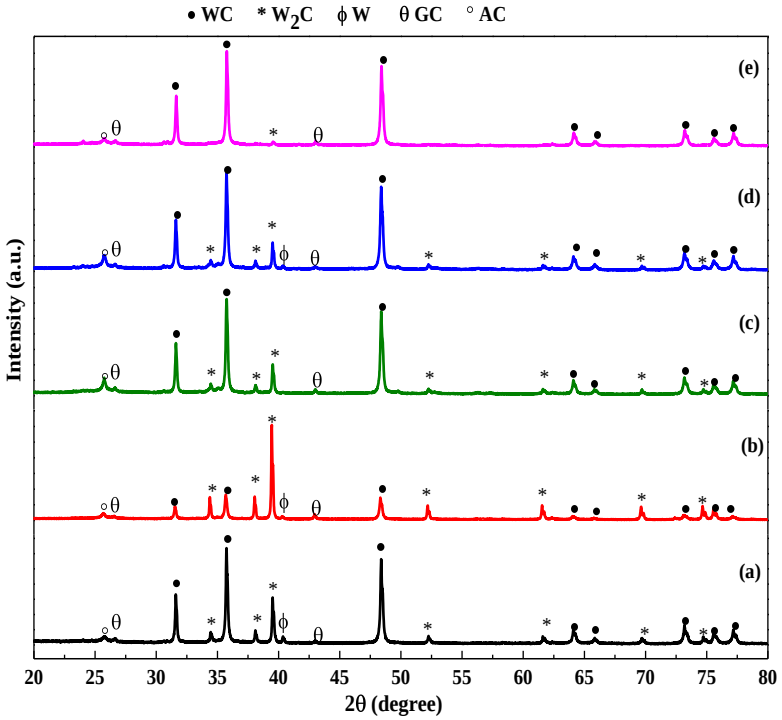

Figure 4.16: XRD patterns of samples **(a)** A575-2-10 **(b)** A600-2-10 **(c)** A615-2-10 **(d)** A625-2-10 and **(e)** A700-2-10 synthesized by acetone (10 mL) for reaction time of 2 h at reaction temperature 575 °C, 600 °C, 615 °C, 625 °C and 700 °C.

The appearance of peaks corresponding to W, W_2C and WC phase in **figure 4.16(a)** indicates the complete reduction of WO_3 into W at temperature 575 °C, which further continue to carburize. The molar fractions "*m*" of each phase(s) in a W_2C-WC-W mixture was calculated from XRD using equation (4.8) and is listed in **table 4.5 [53].**

$$m = \frac{h_1}{h_1 + h_2 + h_3} \tag{4.8}$$

where h_1, h_2 and h_3 are the peak heights of the most intense reflections of W_2C, WC and W, respectively. The tabular data clearly revealed that higher content of WC is obtained at temperature 575 °C, which decreased with the increase in reaction temperature to 600 °C. However, the increment in the % age of W_2C at this temperature displays the reversibility of carburization process. While, with the further increase in the reaction temperature upto 700 °C, the consistent increase in the content of WC attributes that the carburization process again moves in the forward direction with the diffusivity of more carbon in W_2C (W_2C + C→2WC).

Table 4.5: Comparison of phase(s) percentage obtained in W_2C–WC–W mixture at different temperatures and constant holding time 2 h.

Sample	Temperature (°C)	% age of phase(s)		
		WC	W_2C	W
A575-2-10	575	64	31	5
A600-2-10	600	20	77	3
A615-2-10	615	74	23	3
A625-2-10	625	77	21	2
A700-2-10	700	95	5	-

As mentioned in our earlier discussions, the freshly prepared W phase reacts with *in-situ* produced nascent C atoms and results to form WC nano particles. Hence, the synthesis temperature 600 °C for reaction time 2 h has been decided the optimum synthesis temperature for getting higher amount of W_2C phase with 10 mL acetone. Furthermore, in order to obtain the higher amount of W_2C at this reaction temperature, the next variation has been done in the reaction time from 1 to 3 h. The XRD patterns with the variation in reaction time at constant temperature (600 °C) and acetone amount (10 mL) is shown in **figure 4.17.** The observed fraction of all the phase(s) present in **figure 4.17** has been given in **table 4.6**. The tabular data clearly indicates that, the higher content of WC has been found at lower time 1 h in the sample A600-1-10 due to the fast diffusion of carbon.

With the increase in time to 2 h, the content of WC is decreased due to the reversibility of the carburization process which results in increase in the content of W_2C phase in the obtained sample A600-2-10. However, the increment in both the content of WC and W observed at higher reaction time 2.5 h, attributes the eutectoid decomposition of W_2C ($W_2C \rightarrow WC + W$) which occur below 1300 °C **[54]**. But the reaction between W and C at the reaction time of 3 h contributes in the increment of W_2C and WC content. So, based on these results, the reaction time of 2 h has been observed suitable for getting higher content of W_2C phase. Afterwards, the influence of acetone amount on the percentage of W_2C phase has been analyzed at 600 °C for 2 h holding time in the next set of experiments.

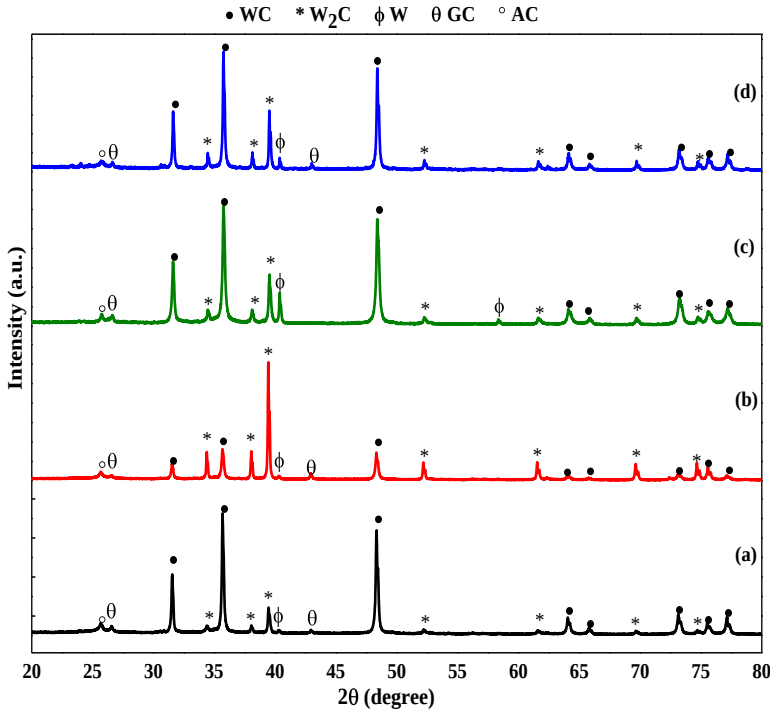

Figure 4.17: XRD patterns of samples **(a)** A600-1-10, **(b)** A600-2-10, **(c)** A600-2.5-10 and **(d)** A600-3-10 synthesized by acetone (10 mL) and reaction temperature 600 °C at reaction time 1 h, 2 h, 2.5 h and 3 h.

Table 4.6: Comparison of phase(s) percentage obtained in W_2C–WC–W mixture at different reaction time and constant temperature 600 °C.

Sample	Reaction time (h)	% age of phase(s)		
		WC	W_2C	W
A600-1-10	1	79	17	4
A600-2-10	2	20	77	3
A600-2.5-10	2.5	59	26	15
A600-3-10	3	62	31	7

A typical XRD pattern of the synthesized black powder with the variation in the acetone amount is shown in **figure 4.18.** The details of the fraction of phase(s) appeared in **figure 4.18** have been summarized in **table 4.7**. The higher content of W_2C phase obtained in sample A600-2-2.5 indicates that reduced WO_3 is not carburized completely into WC either due to lower carbon concentration gradient or fast quenching of autoclave. With the further increase in the acetone amount due to the higher amount of *in-situ* produced carbon, it starts

to diffuse inside reduced W/W_2C phase, which results to form tungsten mono-carbide (WC) on the expense of W_2C ($W_2C + C \rightarrow 2WC$) and W ($W+C \rightarrow WC$). But higher carburizing agent amount in sample A600-2-10 also restricts further diffusion of carbon, which results to increase the content of W_2C again. In all this process, the content of W phase decreases consistently which supports the carburization reaction to move in the forward direction. However, on the further increase in acetone amount (20 mL), it has been observed that the content of WC increase with the consumption of W_2C phase (data not shown). So, it is worthwhile to point out that higher content of W_2C by using acetone as a carbon source could be obtained at specific synthesis conditions which have been followed in sample A600-2-10.

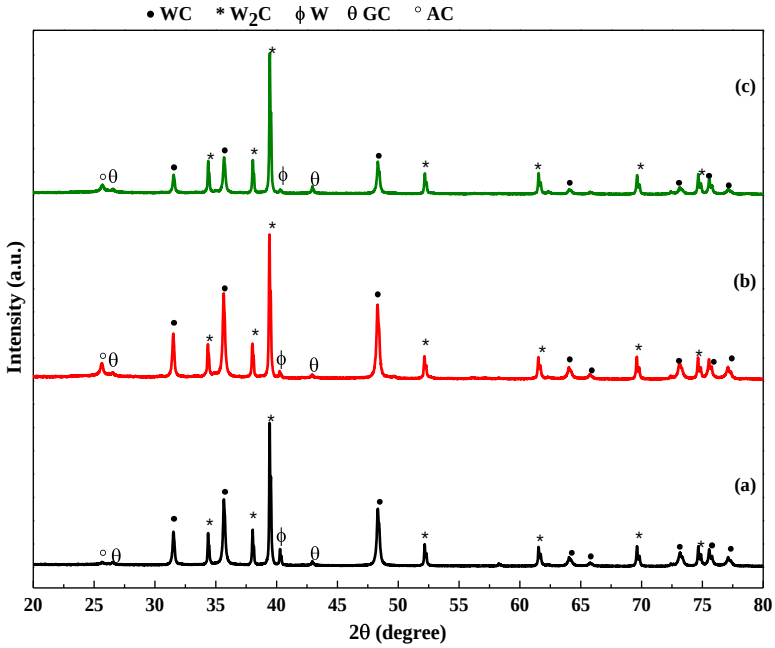

Figure 4.18: XRD patterns of samples **(a)** A600-2-2.5 **(b)** A600-2-5 and **(c)** A600-2-10 synthesized by using acetone as carburizing agent at constant reaction temperature 600 °C and reaction time 2 h after varying acetone amount 2.5 mL, 5 mL and 10 mL.

Table 4.7: Comparison of phase(s) percentage obtained in W_2C–WC–W mixture by varying acetone amount at constant temperature 600 °C and holding time 2 h.

Sample	Acetone amount (mL)	% age of phase(s)		
		WC	W_2C	W
A600-2-2.5	2.5	26	65	9
A600-2-5	5	33	62	5
A600-2-10	10	20	77	3

4.2.1.2 Activated charcoal as carburizing agent

In this set of experiments**, figure 4.19** shows the XRD patterns after acid leaching of samples C600-1.25-0.5, C600-1.5-0.5, C600-2-0.5, C600-2.25-0.5, C600-3.5-0.5, C700-2-0.5 obtained by using activated charcoal as a carbon source. The influence of reaction time on the % age of phase(s) within the prepared materials has been investigated at constant temperature 600 °C by taking 0.5 g activated charcoal.

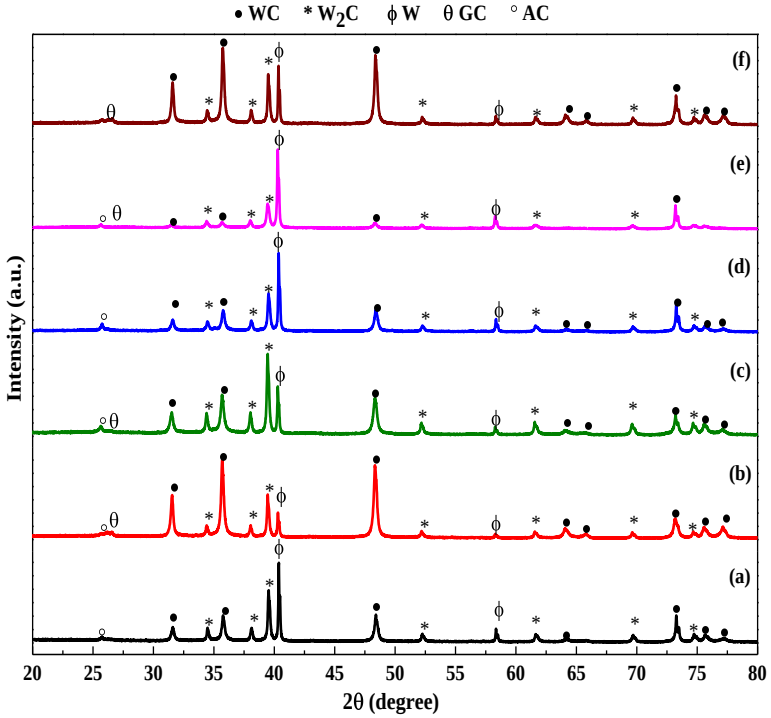

Figure 4.19: XRD patterns of samples **(a)** C600-1.25-0.5 **(b)** C600-1.5-0.5 **(c)** C600-2-0.5 **(d)** C600-2.25-0.5 **(e)** C600-3.5-0.5 and **(f)** C700-2-0.5 synthesized by using activated charcoal as carbon source with constant amount 0.5 g.

The details of phase % age with the variation in reaction time are summarized in **table 4.8**. It is worth noting from the XRD pattern (**figure 4.19(a)**) and **table 4.8**, that at lower reaction time (1.25 h), content of W is on the higher side due to the lack of time for the carbon diffusivity in the freshly prepared W phase. With the increase in the reaction time to 1.5 h, the carbon atoms have sufficient time for diffusion inside the W and results to increase the content of WC abruptly (**table 4.8**). With the further increase in reaction time to 2 h for sample C600-2-0.5, the content of W_2C and W increased, which shows the reversibility of carburizing reaction (decarburization). Moreover, with the increase in the reaction time after 2 h the rate of decarburization seems to be increased. It results to decrease the content of both carbides phase especially WC which is represented by reaction $2WC \leftrightarrow W_2C+C \leftrightarrow W+C$.

Hence, the reaction time of 2 h has been observed as the time for the initiation of reversibility of carburization process.

Table 4.8: Comparison of phase(s) percentage obtained in W_2C–WC–W mixture at different reaction time and temperature 600 °C/700 °C.

Sample	Reaction time (h)	% age of phase(s)		
		WC	W_2C	W
C600-1.25-0.5	1.25	17	33	50
C600-1.5-0.5	1.5	53	30	17
C600-2-0.5	2	24	47	29
C600-2.25-0.5	2.25	16	28	56
C600-3.5-0.5	3.5	7	23	70
C700-2-0.5	2	41	27	32

However, on comparing the results obtained by varying the reaction temperature from 600 °C to 700 °C at constant reaction time 2 h, the content of W_2C decreases. That may be due to the eutectoid decomposition of W_2C into W and WC ($W_2C \rightarrow W+WC$) which could exist below 1300 °C **[54]**, and results to increase the contents of both WC and W phase.

Hence, by observing the higher amount of W_2C in the sample C600-2-0.5, next set of experiments was planned by varying the amount of activated charcoal to carburize 29% unreacted W phase. In this case, at lower amount of activated charcoal (0.25 g) the obtained product has been visualized oxide, so the amount of activated charcoal has been varied in between 0.5 to 2 g for getting W_2C nano powder enriched phase in the prepared powder samples. The XRD patterns at these conditions is shown in **figure 4.20** and the variation in % age of phase(s) evaluates from this patterns has been mentioned in **table 4.9**. From the XRD results and data shown in **table 4.9**, it is clear that with the increase in the amount of carburizing agent, the carburization of W has taken place, which also activates the carburization of W_2C and results to increase in the content of WC. It occurs due to the higher concentration gradient of carbon in the outer region of the reduced nano particles and enhances the carburization process which results to decrease the W_2C and W content consistently.

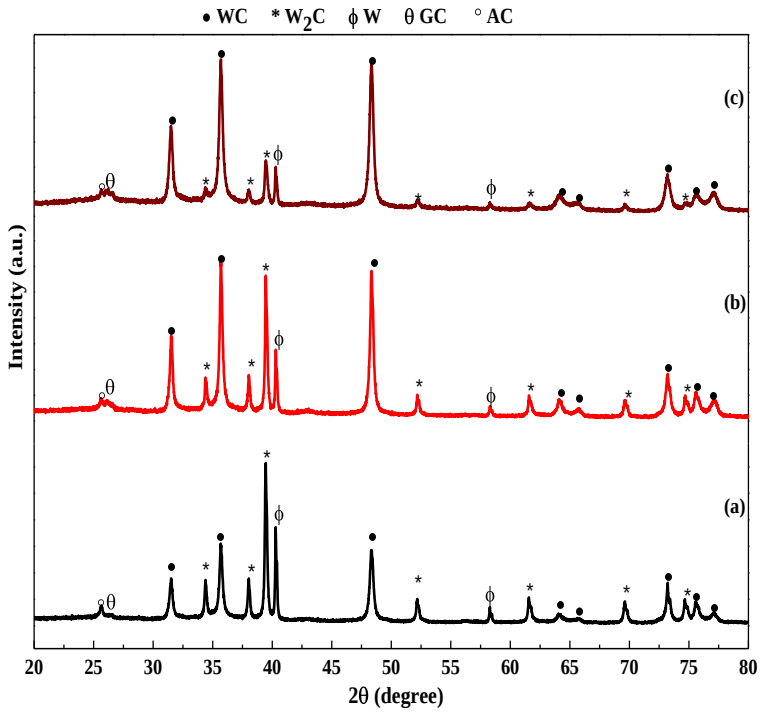

Figure 4.20: XRD patterns of samples **(a)** C600-2-0.5 **(b)** C600-2-1 and **(c)** C600-2-2 synthesized by using activated charcoal as carburizing agent at constant reaction temperature 600 °C and reaction time 2 h after varying activated charcoal amount 0.5 g, 1.0 g and 2.0 g.

Table 4.9: Comparison of phase(s) percentage obtained in W_2C–WC–W mixture by varying charcoal amount at constant temperature 600 °C and holding time 2 h.

Sample	Amount of activated charcoal (g)	% age of phase(s)		
		WC	W_2C	W
C600-2-0.5	0.5	24	47	29
C600-2-1	1.0	38	40	22
C600-2-2	2.0	57	22	21

4.2.1.3 Hexane as carburizing agent

In order to understand the kinetic of W_2C formation, one of the hydrocarbon source (hexane) having higher amount of carbon is also used in this study. But due to the higher number of carbon atoms in hexane (C_6H_6) as compared to acetone (C_3H_6O), only the amount of hexane has been optimized to get the W_2C enriched phase in the obtained black powder. It is evident from the XRD results of samples obtained from acetone and activated charcoal that the 2 h reaction time at 600 °C is optimum and is the best synthesis conditions for getting higher content of W_2C. So in this set of experiment, these conditions are used in order to

observe the influence of hexane amount on the content of W_2C. The XRD patterns of samples synthesized by using different amount of hexane have been plotted in **figure 4.21**. The fraction of phase(s) with the variation in the amount of carburizing agent (C_6H_6) has been mentioned in **table 4.10**. The XRD patterns of samples H600-2-2.5 and H600-2-5 in **figure 4.21(a & b)** shows that with the lower amount of hexane (2.5 and 5 mL), the reduction as well as carburization of metal oxide (WO_3) has not been accomplished completely.

However, the presence of lower oxide (WO_2) in **figure 4.21(a & b)** clearly indicates that the reduction as well as carburization process would be very fast with the change in synthesis conditions. This effect has been confirmed by the XRD pattern of sample H600-2-10 in **figure 4.21(c),** which is obtained at higher hexane amount (10 mL). It shows the existence of both phases WC and W_2C at this synthesis condition, which is due to the higher concentration gradient of *in-situ* produced carbon in the system. This enhances the carburization rate and results to decrease WO_2 content. In order to understand the kinetic of carburization at higher amount of hexane, the XRD pattern showing monoclinic WO_3 (ICDD reference number 01-088-0550), monoclinic WO_2 (ICDD reference number 00-032-1393) and W with minor appearance of W_2C at lower amount of hexane needs to be analyzed with the help of thermodynamic study. The peaks corresponding to these phases (WO_3, WO_2 and W) in **figure 4.21** are so broad that the pattern appears more like that from an amorphous nature than the crystalline.

According to **Li et al.** [**9**] a derivative sub-oxide or possibly defective sub-oxide, acts as a preferential nucleation site for carbide formation. But the carburization process begins only when the solid is reduced to an overall stoichiometry lower than WO_1 [**10**]. So, it is assumed that due to lower crystallite size of WO_2 (~3.6 nm) calculated by Scherrer equation, it becomes highly reactive and tends to convert into W easily through the most probable reaction (xi). Hence, the constant content of W_2C at higher hexane amount (**table 4.10**) and lower value of ΔG for reaction (xiv) as compared to (xiii) at 600 °C attributes that W phase after successfully reduction carburized directly into WC. Moreover, due to the defragmentation of metal oxide into smaller size due to H_2 gas arising during the decomposition of liquid hydrocarbon; the content of carbide seems to be on higher side as compared to samples obtained by using activated charcoal. The detail of reduction as well as carburization in terms of schematic mechanism has already been discussed in our earlier part.

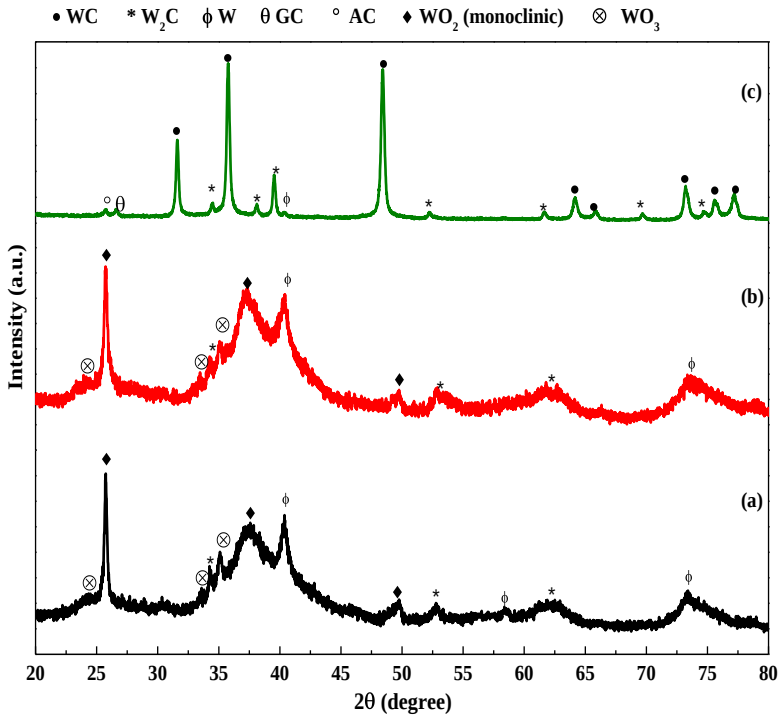

Figure 4.21: XRD patterns of samples **(a)** H600-2-2.5, **(b)** H600-2-5 and **(c)** H600-2-10 synthesized by using hexane as carburizing agent at constant reaction temperature 600 °C and reaction time 2 h after using hexane amount 2.5 mL, 5 mL and 10 mL.

Table 4.10: Comparison of phase(s) percentage obtained in W_2C–WC–W mixture by varying hexane amount at constant temperature 600 °C and holding time 2 h.

Sample	Amount of hexane (mL)	% age of phase(s)				
		WO_3	WO_2	WC	W_2C	W
H600-2-2.5	2.5	11	35	-	22	32
H600-2-5	5.0	5	38	-	22	35
H600-2-10	10	-	6	68	21	5

From the above focused experiments, it can be concluded that it is difficult to produce single phase W_2C from this method. However, under optimized condition W_2C- rich carbide phase can be obtained. Most of the authors have also obtained carbide nano powder by adopting different methods and found mixed phases (WC/W_2C) with W_2C main phase [**55-57**].

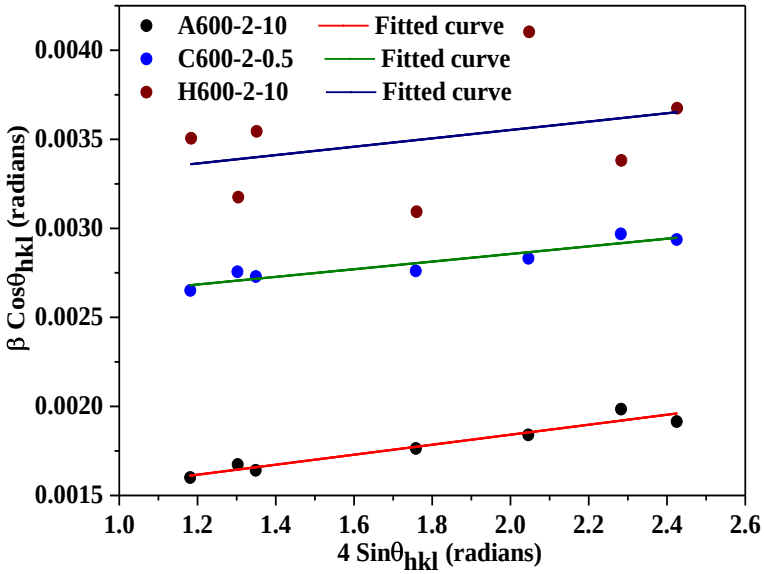

Figure 4.22: Williamson–Hall plot of samples **(a)** A600-2-10 **(b)** C600-2-0.5 and **(c)** H600-2-10 by assuming UDM.

From the broadened nature of XRD peaks of obtained W_2C phase, the strain (ε) and crystallite size (D) has been obtained by using W-H equation (4.3) by plotting the value of $\beta_{hkl}Cos\theta_{hkl}$ as a function of $4Sin\theta_{hkl}$ especially, for samples A600-2-10, C600-2-0.5, H600-2-10 having higher content of W_2C in **figure 4.22**. The peak position (2θ), integrated intensity, the peak maximum position and the peak width of the individual reflections was obtained through fitted Gaussian function. The values of ε and D are estimated from the slope of the line as well as from the intersection with the vertical axis, respectively and are given in **table 4.11**. As discussed earlier, the equation (4.3) represents the UDM in which strain was assumed to be uniform in all crystallographic directions by considering the isotropic nature of the crystal.

However, all the above calculations have been done after considering uniform strain in all directions of the isotropic crystal. But, in most of the cases, the assumption of the homogeneity and isotropy is not fulfilled so USDM and UDEDM have been taken by assuming the cause of anisotropic micro strain ε_{hkl} to be uniform deformation stress σ. After considering the Hooke's law which refers to the strain by keeping only the linear proportionality between deformation stress and strain as given by $\sigma = \varepsilon_{hkl}E_{hkl}$, where σ is the deformation stress of the crystal and E_{hkl} is modulus of elasticity.

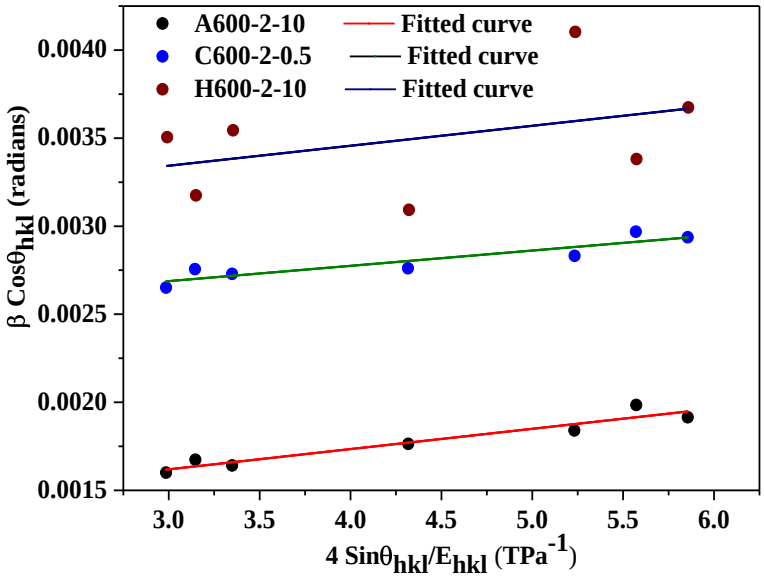

Figure 4.23: The modified form of W–H analysis assuming USDM for samples **(a)** A600-2-10 **(b)** C600-2-0.5 and **(c)** H600-2-10.

For a sample with hexagonal crystal phase (W_2C), Young's modulus E_{hkl} is given by the equation (4.5). The value of elastic compliances (s_{11}=2.415 ×10^{-3} GPa^{-1}, s_{13}=0.947 × 10^{-3} GPa^{-1}, s_{33}=2.77 × 10^{-3} GPa^{-1} and s_{44}=4.61 ×10^{-3} GPa^{-1}) used in this equation for W_2C has been calculated from elastic constant by using relations between them [**58, 59**]. The results obtained from USDM and UDEDM corresponding to equations (4.4) and (4.6) are plotted in **figure 4.23** and **figure 4.24** respectively. The data obtained from these figures are summarized in **table 4.11**. From the calculated value of ε, it is clear that the synthesized samples are in the strained form. It arises due to the transformation of lower ionic radii ion (0.6 nm) W^{6+} to higher ionic radii (0.66 nm) W^{4+} during the formation of W_2C nano powder. The positive value of strain clearly indicates the presence of tensile strain in the system, which results to induce lattice expansion [**27**].

As observed from **table 4.11**, the higher value of strain for samples obtained from liquid hydrocarbon (A600-2-10, H600-2-10) might be because of the distortion that arises in the system during the fragmentation of WO_3 via *in-situ* produced hydrogen gas in liquid hydrocarbon source. Due to the smaller size of these fragmented oxide particles; the carburization occurs rapidly and results to more distortion in the system **[60]**. While, in case of sample C600-2-0.5, no such kind of activity occur for the reduction of WO_3 due to which the strain is minimum in this sample. The unit cell volume has also been evaluated by calculating the lattice parameters using (100) and (002) peaks in the XRD patterns.

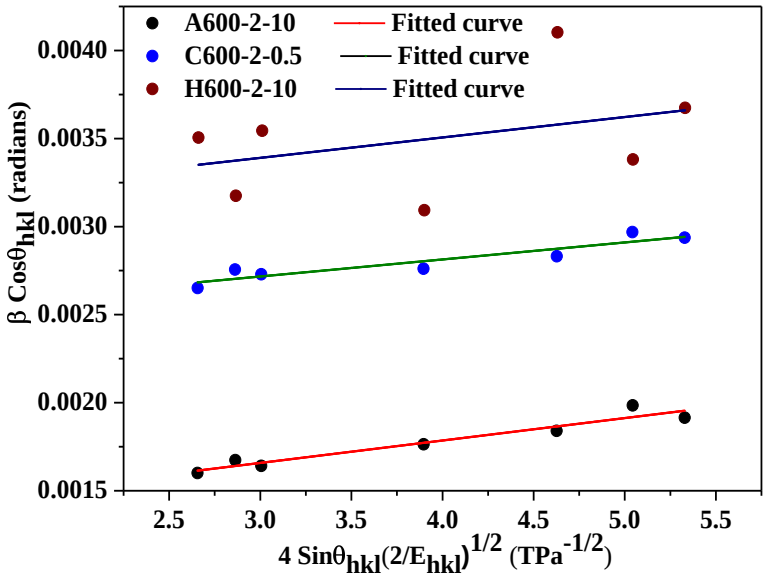

Figure 4.24: The modified form of W–H analysis assuming USEDM for samples **(a)** A600-2-10 **(b)** C600-2-0.5 and **(c)** H600-2-10.

Table 4.11: The data obtained from XRD analysis of the samples obtained at temperature 600 °C for 2 h with varying carbon amount.

			A600-2-10	C600-2-0.5	H600-2-10
W_2C	UDM	$\varepsilon \times 10^{-3}$	0.280	0.214	0.235
		D (nm)	108	57	45
	USDM	$\varepsilon \times 10^{-3}$	0.280	0.214	0.235
		D (nm)	107	56	45
		σ (GPa)	0.115	0.086	0.113
	UDEDM	$\varepsilon \times 10^{-3}$	0.282	0.214	0.257
		D (nm)	107	56	45
		σ (GPa)	0.114	0.086	0.104
		$u \times 10^3$ (kJ/m^3)	0.016	0.009	0.013
	Volume of unit cell (Å^3)		37.11	37.10	36.90

Moreover, the interaction of hydrogen with metallic oxide after the decomposition of hydrocarbon, is highly responsible for the crystallinity in the samples A600-2-10 and H600-2-10 and increases the crystallite size (D) of A600-2-10 sample, especially. While, the lower crystallite size in sample H600-2-10 may be due the disordering in the system that arise as a result of fast diffusion of carbon to carburize into WC. The correlation between crystallite size and lattice parameter as discussed earlier in the synthesis of WC has been reversed in this

case. The current trend attributes that in carbon deficient system, with the decrease in the crystallite size, the Me-C bond seems to be strong which decreases the lattice parameter and hence, lattice volume of the crystal.

Due to the deficiency of carbon atom in W_2C, the order of strain obtained in W_2C nano particles is lower as compared to WC which is shown in **table 4.1**. Hence, it is confirmed that the diffusion of carbon in the reduced transition metal (W) play an important role to enhance the distortion in the system in terms of inducing strain. Since, the lattice strain in any materials indicates disorderness in the system so; it is responsible for its higher activity. Moreover, from the observed USDM and UDEDM, it has been concluded that the lower value of deformation stress and deformation energy density in the carbide phase W_2C synthesized by activated charcoal corresponds to lower distortion in the lattice due to the lower interaction of amorphous solid carbon with metal oxide (WO_3). It creates little internal stress in the synthesized sample due to which the strain is also lower among all synthesized samples.

4.2.2 Thermal Analysis

Figure 4.25 shows the thermal analysis of selected samples (A600-2-10, C600-2-0.5 and H600-2-10) synthesized by using different carbon sources under the effect of fast cooling of autoclave which have higher content of W_2C phase. It is clear from the TGA plot that for all the samples, weight loss (2-7 %) occurs continuously during heating upto ~400 °C. The reduction in weight below 400 °C may be due to the presence of moisture and some functional group available on the surface of carbon [**29**]. Afterwards, the oxidation of free carbon and carbon coated obtained nano particles (mixture of oxide, carbide and metallic (W) phase) begin and results to leave stable WO_3 at higher temperature which is represented by the plateau after ~700 °C. Such kind of behavior in nano carbide samples has already been observed by many authors in their own systems **[30, 31]**. The rate of weight loss is quite low below ~400 °C and high loss rate occurs above 500 °C especially for sample A600-2-10.

Moreover, the behavior of TG curve for sample C600-2-0.5 attributes the increment in weight at 450 °C due to the presence of higher content of W (29%) phase in the sample as given in **table 4.9.** The appearance of metallic phase (W) in the product initiates the oxidation process in terms of weight gain earlier. Also, the small hump of weight gain at temperature ~350 °C for sample H600-2-10 corresponds to the oxidation of lower oxide/defective oxide (WO_2) present in the product which has more tendencies to get oxidized.

Furthermore, the peak corresponding to weight gain due to the oxidation of carbides content in sample H600-2-10 appeared at higher temperature ~600 °C. As discussed earlier, the initiation of weight loss/gain in TG curves of carbide samples correspond to their oxidation with the formation of CO_x (x=1, 2) and is an indicator of stability of the obtained product. The higher thermal stability of synthesized samples is also influenced by the strong Me-C bonding or the presence of oxide/carbon content on the particle surface in the form of thick/thin layer.

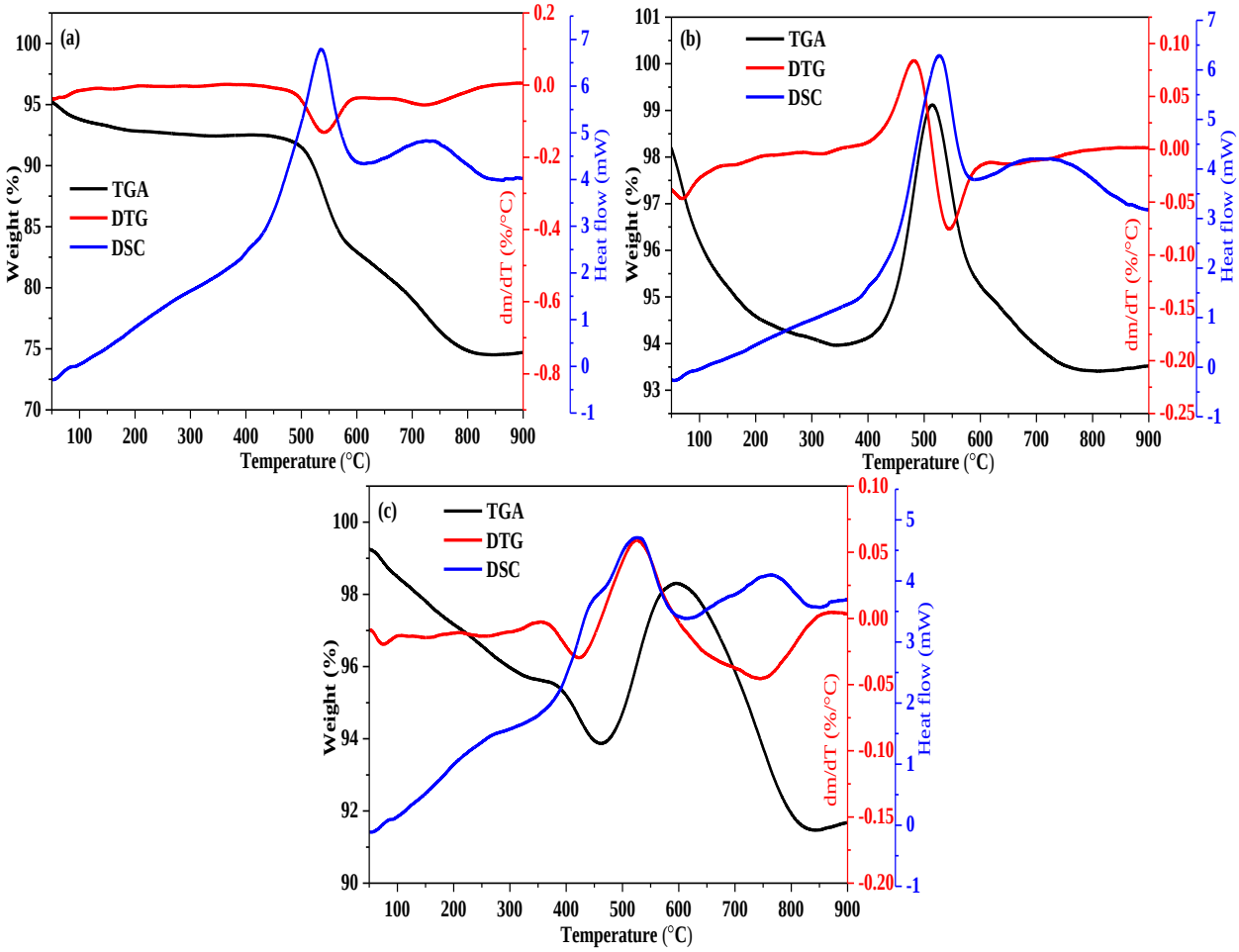

Figure 4.25: TG, DSC and DTG results of powder samples **(a)** A600-2-10 **(b)** C600-2-0.5 and **(c)** H600-2-10.

These layers restrict the further oxidation and delay the oxidation process. The fraction of carbon present in the final synthesized powder is calculated by using equation given below **[29]**.

$$\text{Free C (\%)} = 100 \times \left(1 - \frac{m_f}{m_i} \times \frac{MW_{WC} + MW_{W2C}}{3 \times MW_{WO_3}}\right) \quad (4.10)$$

However, the presence of peaks in DSC curve in the temperature range 525-550 °C attributes the onset temperature for the oxidation of powder samples. The appearance of these peaks confirms that the process of oxidation is highly exothermic. The amount of heat generated during exothermic process is calculated from the total area enclosed by the thermal analysis DSC peak and the results of obtained ΔH corresponding to that area has been mentioned in **table 4.12**. The higher value of ΔH corresponds to the presence of higher amount of carboneous elements in the samples which has been confirmed from **table 4.12**. Moreover, the samples which contain higher amount of free carbon also display the shifting in the exothermic peak towards higher temperature. Hence, the value of ΔH and shifting in the DSC peaks are correlated with the presence of carboneous amount in the product which affect the thermal stability.

Table 4.12: The data obtained from TGA thermo-gram analysis of the synthesized samples.

Sample	DSC peak (°C)	Free C (%)	Carbides content (%)	ΔH (kJ/g)
A600-2-10	535	39	61	-2.79
C600-2-0.5	527	25	75	-2.70
H600-2-10	525	24	76	-2.45

As mentioned earlier, the oxidation process of carbide sample has also been discussed by DTG analysis. The appearance of multiple peaks designates the multi step process of oxidation. The DTG peak at temperature 483 °C attributes to maximum weight gain in sample C600-2-0.5 corresponding to the oxidation of W phase present in the obtained powder sample. While, the oxidation of lower oxide contents (WO_2) in sample H600-2-10 is also revealed by the DTG peak at 350 °C. But the presence of DTG peaks **(figure 4.25)** at 541, 543 and 423 °C corresponding to samples A600-2-10, C600-2-0.5 and H600-2-10, respectively designates the oxidation of carbide. The appearance of peaks at these temperatures attributes the maximum weight loss due to removal of carbon from the sample. The DTG peak appeared at temperature ~750 °C for samples A600-2-10 and H600-2-10 indicates the delay in weight loss due to the formation of oxide layer during heating on the surface of obtained product.

4.2.3 Raman analysis

Figure 4.26 shows the Raman spectra for samples A600-2-10, C600-2-0.5 and H600-2-10 obtained by using different carbon sources at temperature 600 °C. The most common and important bands appearing in Raman spectra of samples are D and G-band around 1350-1375 cm^{-1} and 1580-1600 cm^{-1}, respectively **[43, 44]**. According to **Ferrari and Robertson [44],** the D-band is often attributed to disorder scattering, and this mode remains absent in perfect graphite.

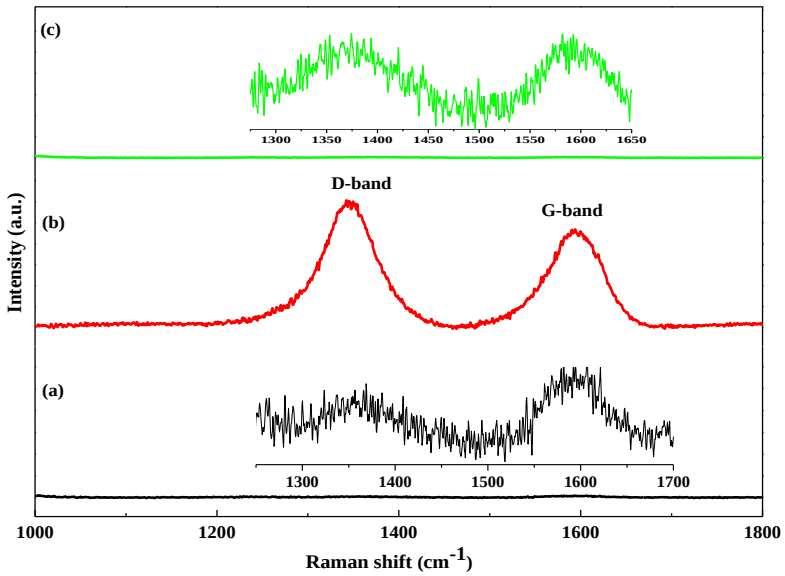

Figure 4.26: Raman results of samples **(a)** A600-2-10 **(b)** C600-2-0.5 and **(c)** H600-2-10.

While, the position of G-band is related to the tangential stretching mode of all pairs of sp^2-C atoms present in the system [**45**]. The shifting of G-band position from 1592 cm^{-1} to lower wave number has been observed when the carbon source(s) is changed (**table 4.13**). It attributes the defects/disordering in the graphitic cluster within the system [**46**]. The data obtained from peaks fitting are summarized in **table 4.13**. This transition from ordering to disordering enhances the reactivity of outer carbon layer which tends to react with oxygen easily. Hence, due to this fact, the onset temperature corresponding to oxidation for samples C600-2-0.5 and H600-2-10 shifts to lower temperature in TGA curve. Moreover, due to the ordered sp^2-C phase in sample A600-2-10, it assembles in the form of layered onion like structure whose appearance has also been confirmed in microstructure of the respective sample discussed later [**47**].

Table 4.13: Raman characteristics of samples obtained from different carbon sources.

Sample	A600-2-10	C600-2-0.5	H600-2-10
D-band (cm^{-1})	1355	1344	1374
G-band (cm^{-1})	1592	1587	1589
I_D/I_G	0.77	1.25	0.82

The intensity ratio between the D-band and G-band (I_D/I_G) provides information about the structural ordering of sp^2 phase (degree of graphitization) [**47**]. The lower value of I_D/I_G for sample A600-2-10 also ascribed to the higher degree of graphitization among the discussed samples. While, on the other hand, the higher value of I_D/I_G (>1) in sample C800-2-10 designates the appearance of more defects, which results to lower graphitization in the sample on changing the carburizing agents.

4.2.4 BET surface area analysis

In order to determine the effect of carbon source(s) as well as the effect of fast cooling on the texture properties of prepared samples, N_2 adsorption–desorption isotherm analysis has been done. As, it has been discussed in our earlier section of WC@C synthesis, that in the current method, the formed carbide samples attain an excess carbon layer on carbides nano particles. These carbon layers may have suitable porous structure and high surface area, which exhibit typical type IV curve for all samples. Hence, these curves designate the characteristics of materials, which contain mesoporosity and attain high energy adsorption [**35**]. As per our earlier discussion, the N_2 adsorption/desorption isotherm shown in **figure 4.27** displays distinct hysteresis loop of H3 type. This hysteresis is usually found for the solids consisting of aggregates or agglomerates of particles forming slit-shaped pores with non-uniform size and/or shapes [**36**].

Figure 4.28 shows the pore size distribution curves of the samples in the range of 3 to 5 nm. In the pore size distribution curve, the peak around pore diameter 4 nm shows the presence of mesopores in the samples. Its existence may be due to the stabilization in the outer surface of the synthesized samples. The pore size, specific surface area and pore volume of the synthesized samples from N_2 adsorptions are listed in **table 4.14**. As shown in the **table 4.14**, the sample synthesized by solid carbon source (C600-2-10) has higher specific

surface area. It may be due to the lower graphitization in the respective sample which promote to its higher surface area which is also observed in the Raman analysis. The variation in the surface area and pore distribution among samples obtained by liquid carbon sources arises due to the collapse of pores/filling the pores by excess carbon in H600-2-10. These two effects contribute simultaneously and decrease the micropores and mesoporous and surface area.

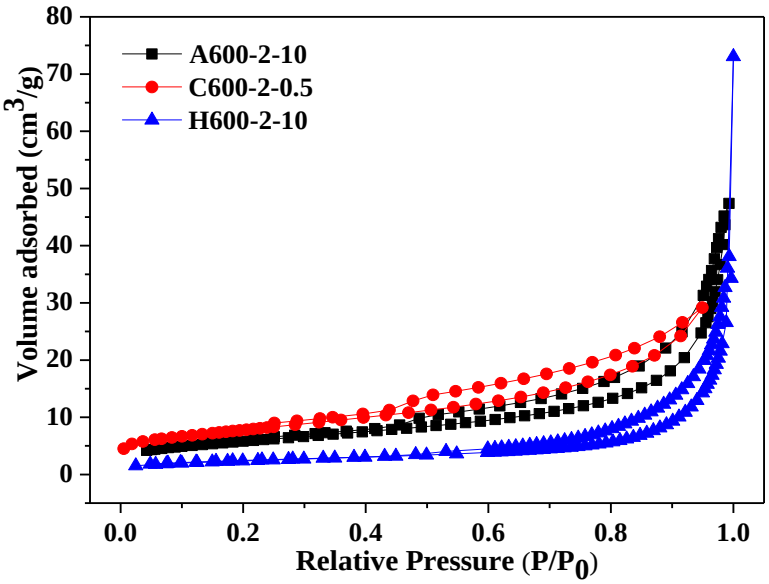

Figure 4.27: N_2 sorption isotherms of samples **(a)** A600-2-10 **(b)** C600-2-0.5 and **(c)** H600-2-10.

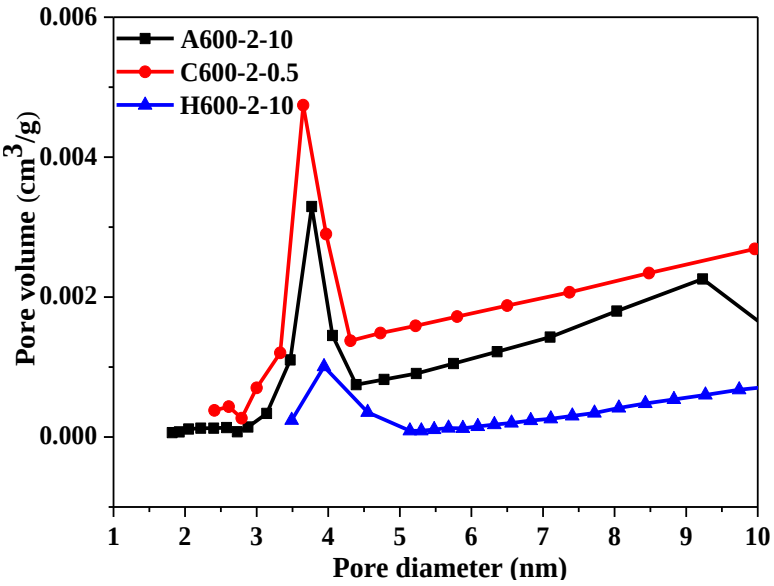

Figure 4.28: Pore size distribution of samples **(a)** A600-2-10 **(b)** C600-2-0.5 and **(c)** H600-2-10.

Table 4.14: Structure parameters of samples obtained from N_2 sorption isotherms.

Sample	A600-2-10	C600-2-0.5	H600-2-10
BET (m^2/g)	20.8	27.7	8.5
Total pore volume (cm^3/g)	0.072	0.037	0.059
Average pore diameter (nm)	13.2	6.1	23.1

4.2.5 Microstructure analysis

The microstructure analysis was done for the selected samples (A600-2-10, C600-2-0.5 and H600-2-10) in which WC/W_2C was present. The TEM images (**figure 4.29(a, c and e)**) clearly show that most of the prepared nano particles have core-shell morphology which is also observed earlier in the synthesis of tungsten mono-carbide (WC) and also observed by the other authors in their work **[48, 49]**. The details of the formation mechanism of core-shell structure are discussed in our earlier discussion. These synthesized nano particles are composed of an internal core with dark shade (WC/W_2C nano particle) and external shell with light shade (carbon). However, the TEM images obtained for the synthesized powder samples clearly show the faceted morphology with uniform distribution as shown in **figure 4.29(e)**. With respect to charcoal and hexane, the samples obtained by acetone as a carbon source, the outer carbon reveals in the TEM images are of graphitic nature. However, the amorphous carbon around the obtained particles was also seen in the TEM images of sample C600-2-0.5.

Moreover, the free carbon in the form of rings having onion type layer structure has also been seen in the TEM images of A600-2-10 and H600-2-10. Further, HRTEM of samples synthesized by carbon sources, especially liquid hydrocarbons also reveals that the outer layer is of graphitic carbon. The d-spacing value of 0.26 and 0.28 nm belongs to the (100) and (001) plane for the WC phase respectively. Moreover, the d-spacing value of 0.24 nm and 0.22 nm belongs to (200) and (102) which correspond to W_2C phase. Moreover, the results of TEM images (**figure 4.29(a & e)**) obtained for samples A600-2-10 and H600-2-10 attributes that particles attained different morphology. Such kind of change in the morphology in carbide particles may be due to the change in the source of hydrocarbon, which has also been observed by Grove et al. **[51]** in their system. The TEM result of sample H600-2-10 also shows the hexagonal type morphology of synthesized nano particles. The

SAED patterns has been obtained for the samples A600-2-10 and C600-2-0.5 containing WC and W_2C nano particles having hexagonal structure and are shown in **figure 4.29(g & h)**. The spots in the diffraction patterns for samples A600-2-10 and C600-2-0.5 confirms that sample is well crystalline.

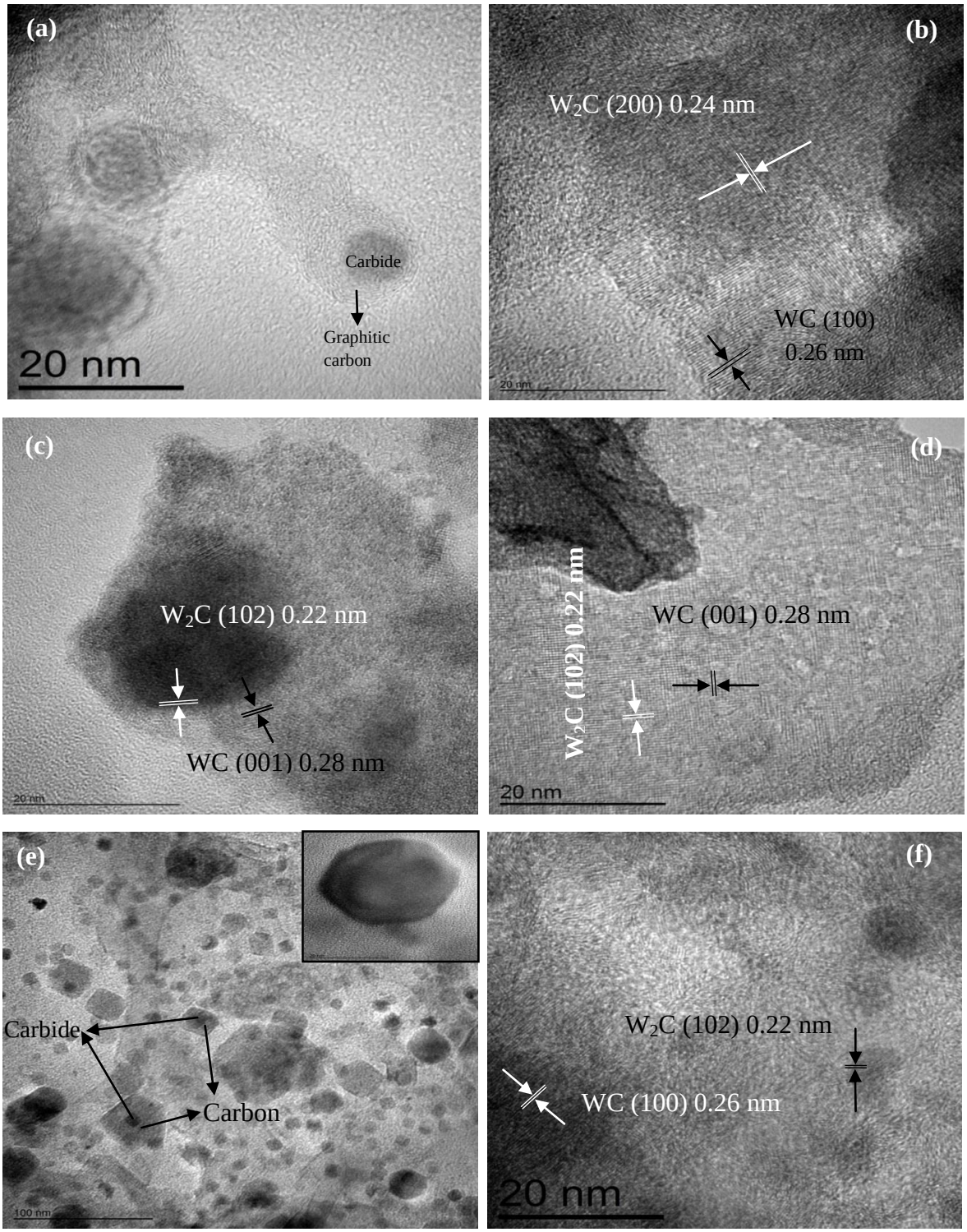

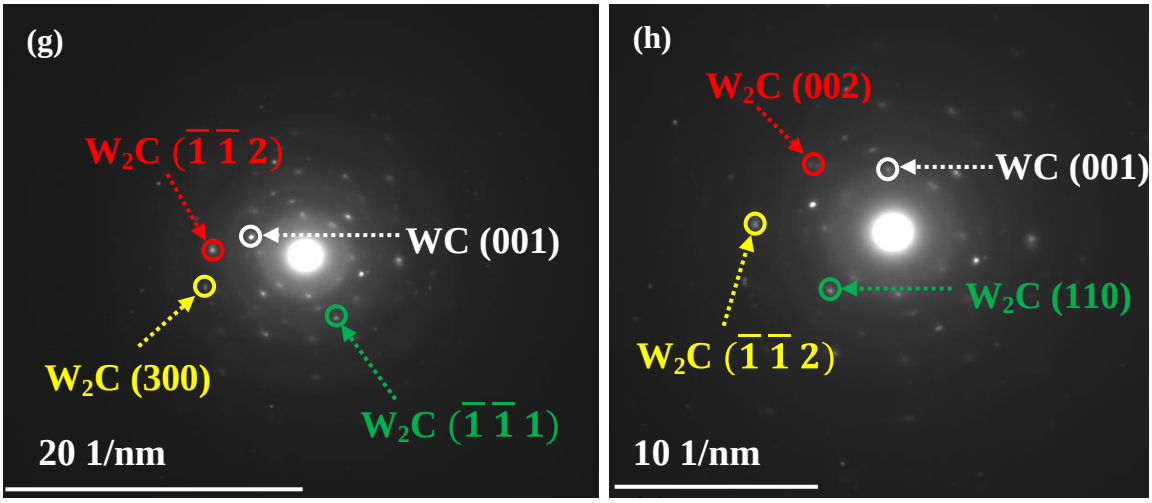

Figure 4.29: TEM/HRTEM images of obtained samples **(a,b)** A600-2-10 **(c,d)** C600-2-0.5 **(e,f)** H600-2-10; SAED patterns of **(g)** A600-2-10 and **(h)** C600-2-0.5.

References:

[1]. W. D. Schubert, E. Lassner, *Int. J. Refract. Met.* H. **10** (1991) 171-183.

[2]. R. Koc, S. K. Kodambaka, *J. Eur. Ceram. Soc.* **20** (2000) 1859-1869.

[3]. Y. Jin, X. Li, D. Liu, C. Liu, R. Yang, *Powder Technol.* **217** (2012) 482-485.

[4]. D. S. Venables, M. E. Brown, *Thermochim. Acta* **291** (1997) 131-140.

[5]. V. K. Díez, C. R. Apesteguía, D. I. J. I. Cosimo, *Latin Am. Appl. Res.* **33** (2003) 79-86.

[6]. Ž. Kamberović, D. Filipović, K. Raić, M. Tasić, Z. Anđić, M. Gavrilovski, *Mater. Technol.* **45** (2011) 27-32.

[7]. J. Ma, S. G. Zhu, *Int. J. Refract. Met. H.* **28** (2010) 623-627.

[8]. A. Rothschild, J. Sloan, A. P. E. York, M. L. H. Green, J. L. Hutchisonc, R. Tenne, *Chem. Commun.* (1999) 363-364.

[9]. X. Li, A. Westwood, A. Brown, R. Brydson, B. Rand, *Carbon* **47** (2009) 201-208.

[10]. A. Löfberg, A. Frennet, G. Leclercq, L. Leclercq, J. M. Giraudon, *J. Catal.* **189** (2000) 170-183.**9**

[11]. S. Bolokang, C. Banganayi, M. Phasha, *Int. J. Refract. Met. H.* **28** (2010) 211-216.

[12]. S. Cetinkaya, S. Eroglu, *Int. J. Refract. Met. H.* **29** (2011) 214-220.

[13]. A. Lackner, A. Filzwieser, P. Paschen, *Int. J. Refract. Met. H.* **14** (1996) 383-391.

[14]. P. Taskinen, P. Hytonen, M. H. Tikkanen, *Scand. J. Metall.* **6** (1977) 228-232.

[15]. A. Magneli, G. Andersson, B. Blomberg, L. Kihlborg, *Anal. Chem.* **24** (1952) 1998-2000.

[16]. M. Binnewies, E. Mike, Thermochemical Data of Elements and Compounds; Wiley-VCH Verlag GmbH, Weinheim 2002

[17]. W. Liu, X. Song, J. Zhang, G. Zhang, X. Liu, *Mater. Chem. Phys.* **109** (2008) 235-240.

[18]. J. Lemaître, B. Vidick, B. Delmon, *J. Catal.* **99** (1986) 415-427

[19]. C. Boyadjian, A. Ağıral, J. G. E. Gardeniers, L. Lefferts, K. Seshan, *Plasma Chem. Plasma P.* **31** (2011) 291-306.

[20]. J. H. Yan, Z. Bo, X. D. Li, C. M. Du, K. F. Cen, B. G. Chéron, *Plasma Chem. Plasma P.* **27** (2007) 115-126.

[21]. A. K. Zak, W. H. A. Majid, M. E. Abrishami, R. Yousefi, *Solid State Sci.* **13** (2011) 251-256.

[22]. B. E Warren, B. L Averbach, *J. Appl. Phys.* **21** (1950) 595-598.

[23]. J. Zang, Y. Zhang, K.W. Xu, V. Ji, *Solid State Commun.* **139** (2006) 87-91.

[24]. D. Balzar, H. Ledbetter, *J. Appl. Crystallogr.* **26** (1993) 97-103.

[25]. Y. D. Su, C. Q. Hu, C. Wang, M. Wen, W. T. Zheng, *J. Vac. Sci. Technol. A* **27** (2009) 167-173.

[26]. M. Sherif El-Eskandarany, *J. Alloys Compd.* **296** (2000) 175-182.

[27]. B. Santara, P. K. Giri, K. Imakita, M. Fujii, *J. Phys. D: Appl. Phys.* **47** (2014) 215302 (1-13).

[28]. E. Lewin, M. Råsander, M. Klintenberg, A. Bergman, O. Eriksson, U. Jansson, *Chem. Phys. Lett.* **496** (2010) 95-99.

[29]. Y. Liao, K. Pan, L. Wang, Q. Pan, W. Zhou, X. Miao, B. Jiang, C. Tian, et al., *ACS Appl. Mater. Interfaces* **5** (2013) 3663-3670.

[30]. Z. Q. Li, H. F. Zhang, X. B. Zhang, Y. Q. Wang, X. J. Wu, *Nanostruct. Mater.* **10** (1998) 179-184.

[31]. Z. Yan, H. Meng, P. K. Shen, R. Wang, L. Wang, K. Shi, H. Fu, *J. Mater. Chem.* **22** (2012) 5072-5079.

[32]. R. B. Levy, M. Boudart, *Science* **181** (1973) 547-549.

[33]. S. Izhar, M. Nagai, *J. Power Source* **182** (2008) 52-60.

[34]. J. D. Voorhies, *J. Electrochem. Soc.* **119** (1972) 219-222.

[35]. J. B. Condon, *Surface Area and Porosity Determinations by Physisorption Measurements and Theory*, Elsevier Amsterdam, Netherlands (2006).

[36]. G. Leofanti, M. Padovan, G. Tozzola, B. Venturelli, *Catal. Today* **41** (1998) 207-219.

[37]. Y. Liu, S. Shrestha, W. E. Mustain, *ACS Catal.* **2** (2012) 456-463.

[38]. W. Zhu, A. Ignaszak, C. Song, R. Baker, R. Hui, J. Zhang, F. Nan, G. Botton, et al., *Electrochim. Acta* **61** (2012) 198-206.

[39]. G. Li, C. Ma, Y. Zheng, W. Zhang, *Micropor. Mesopor. Mat.* **85** (2005) 234-240.

[40]. G. Li, C. Ma, J. Tang, Y. Zheng, *Mater. Lett.* **61** (2007) 991-993.

[41]. H. Wu, X. Wang, Y. Bai, L. Jiang, C. Wu, B. Hu, Q. Wei, X. Liu, et al., *J. Solid State Electrochem.* **17** (2013) 2453-2460.

[42]. C. Ma, Z. Y. Chen, W. F. Lin, F. M. Zhao, M. Q. Shi, *Micropor. Mesopor. Mat.* **149** (2012) 76-85.

[43]. S. E. Mrabet, M. D. Abad, C. L. Cartes, D. M. Martínezy, J. C. S. López, *Plasma Process. Polym.* **6** (2009) S444-S449.

[44]. A. C. Ferrari, J. Robertson, *Phys. Rev. B* **61** (2000) 14095-14107.

[45]. T. P. Braga, R. C. R. Santos, B. M. C. Sales, B. R. da Silva, A. N. Pinheiro, E. R. Leite, A. Valentini, *Chinese J. Catal.* **35** (2014) 514-523.

[46]. K. N. Kudin, B. Ozbas, H. C. Schniepp, R. K. Prud'homme, I. A. Aksay, R. Car, *Nano Lett.* **8** (2008) 36-41.

[47]. J. Cebik, J. K. McDonough, F. Peerally, R. Medrano, I. Neitzel, Y. Gogotsi, S. Osswald, *Nanotechnology* **24** (2013) 205703 (1-10).

[48]. G. Zhong, H. Wang, H .Yu, F. Peng, *Fuel Cells* **13** (2013) 387-391.

[49]. S. Yang, W. Cai, H. Zhang, H. Zeng, Y. Lei, *J. Phys. Chem. C* **115** (2011) 7279-7284.

[50]. G. Xi, S. Yu, R. Zhang, M. Zhang, D. Ma, Y. Qian, *J. Phys. Chem. B* **109** (2005) 13200-13204.

[51]. D. E. Grove, U. Gupta, A. W. Castleman Jr., *Langmuir* **26** (2010) 16517-16521.

[52]. F. C. Tai, C. Wei, S. H. Chang and W. S. Chen, *J. Raman Spectrosc.* **41** (2010) 933-937.

[53]. C. Liang, F. Tian, Z. Wei, Q. Xin, C. Li, *Nanotechnology* **14** (2003) 955-958.

[54]. A. S. Kurlov, A. I. Gusev, *Tungsten Carbides: Structure, Properties and Application in Hardmetals*, Springer Cham, Switzerland (2013).

[55]. Y. Wanga, S. Song, V. Maragou, P. K. Shen, P. Tsiakaras, *Appl. Catal. B-Environ.* **89** (2009) 223-228.

[56]. M. Wu, P. K. Shen, Z. Wei, S. Songa, M. Nie, *J. Power Sources* **166** (2007) 310-316.

[57]. M. Rahsepar, M. Pakshir, P. Nikolaev, Y. Piao, H. Kim, *Int. J. Refract. Met. H.* **39** (2014) 15706-15717.

[58]. Y. Li, Y. Gao, B. Xiao, T. Min, Z. Fan, S. Ma, L. Xu, *J. Alloy Compd.* **502** (2010) 28-37.

[59]. Y. Li, R. B. Thompson, *J. Appl. Phys.* **67** (1990) 2663-2665.

[60]. N. Hugot, A. Desforges, S. Fontana, J.F. Marêché, C. Hérold, A. Albiniak, G. Furdin, *J. Solid State Chem.* **194** (2012) 23-31.

CHAPTER 5

RESULTS AND DISCUSSION-II

(ELECTROCHEMICAL MEASUREMENTS)

Overview

This chapter comprises of two sections. In the first section the electrochemical study of tungsten mono-carbide (WC) nano powder has been discussed. The cyclic voltammetry (CV) analysis has been done for samples containing pure phase of WC in acidic media (H_2SO_4). The effect on the electrocatalytic activity after Pt dispersion on prepared WC nanoparticles has also been presented. Moreover, the methanol and ethanol electro oxidation has been investigated by varying the concentration of both the alcohols at room temperature. In second section the electrochemical study has been done for the product obtained under the process of fast cooling of autoclave containing mix carbide but having higher content of W_2C phase. The CV analysis has also been done for the samples in acidic media with and without doing platinum deposition. The effect of platinum dispersion on the prepared samples for methanol and ethanol electro oxidation has also been investigated by varying the concentration of alcohols at room temperature. Based on the CV results the kinetic parameters (Tafel slope and exchange current density) have also been evaluated.

In recent years, due to the continuous development in the area of energy storage and production, the carbon supported Pt (Pt/C) has been used extensively as catalyst in energy storage devices **[1, 2]**. However, due to the higher operating temperature conditions and cycling conditions of energy storage devices (fuel cells) this carbon support catalysts corrode rapidly **[3, 4]**. Furthermore, the carbon oxidation/corrosion also results to agglomerate the Pt catalyst which tends to degrade its performance significantly **[5]**. Thus, the current research is focused upon the development of new non carbon-based support catalyst materials, which have low cost, high performance, better stability and durability. Among all the non-carbon support candidates, tungsten carbide (WC) appears to be an important material which shows better chemically inertness, low cost and tolerance to CO poisoning **[6-8]**. Although a lot of work have been done on the analysis of electrochemical properties of WC nano powder, but the scientists are trying to correlate the relation between the surface properties of products obtained by different carbon source with their electrochemical performance. Hence in successive part we will discuss the effect of carburizing agent as well presence of different phase(s) in the obtained product on the electrochemical properties of samples.

5.1 Electrochemical study of synthesized WC nano powder

The cyclic voltammogram (CV) of samples (A600-10, C800-10, H800-10) containing pure phase of WC was obtained in acidic solution (0.5 mol/L H_2SO_4) and shown in **figure 5.1** for I^{st} cycle. It has been done by normalizing with electrode area after considering the anodic current to be positive. The CV curves give an idea about the oxidation stability of samples which is revealed by observing the shifting in onset potential for anodic current specifically at higher potential. As observed from **figure 5.1**, the onset potential for oxidation has been shifted towards higher potential for sample H800-10. The reason of these shifting may be its lower surface area (8.4 m^2/g), which attributes its lower activity towards oxidation. While on the other hand, the powder sample C800-10 containing pure phase of WC exhibits lower onset potential for oxidation. It may be due to its higher surface area, which attributes more active catalytic site for the electrochemical reactions **[9, 10]**. Since the synthesis conditions (temperature and time) for both the electrocatalysts are same but such kind of shifting of onset potential, suggested that the stability of synthesized sample towards electrochemical reaction changes by changing the carburizing agent.

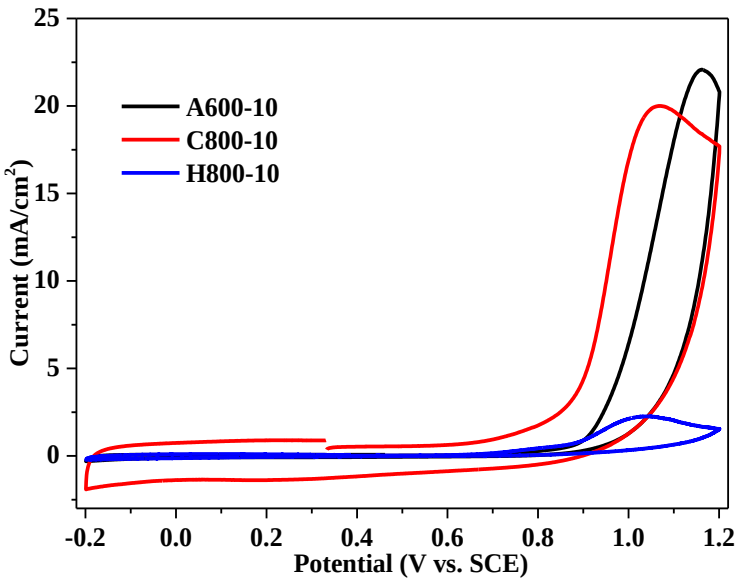

Figure 5.1: Cyclic voltammogram of samples synthesized by **(a)** A600-10 **(b)** C800-10 **(c)** H800-10 after Ist cycle in 0.5 mol/L H_2SO_4; scan speed 30 mV/sec.

Furthermore, the effect of carburizing agent on the response of samples towards the electrochemical activity is also visible from the **figure 5.1** in which the amount of anodic current for sample A600-10 seems to be higher as compared to other samples. The abrupt increment in the anodic current above ~0.9 V *vs.* SCE designates the oxidation region at which WC fully converts into WO_3 as the potential of the working electrode increases linearly **[8, 11, 12]**. In order to understand the electrochemical reaction, the CV curve has been plotted with successive scans in **figure 5.2**. The mechanism of electrochemical reactions on the samples has been considered through three regions. The lower potential region in which the initiation of carbide oxidation (-0.2 to 0.2 V) occur and the onset potential shifts to higher potential with successive scans. It arises due to the formation of oxide layer on the electrode at higher potential which delayed its oxidation. In the intermediate potential region (0.2 V to 0.8 V) the redox peak has appeared in the CV curve especially for sample C800-10 and H800-10. These peaks become more prominent with the increase in CV scans as shown in **figure 5.2(b & c)**.

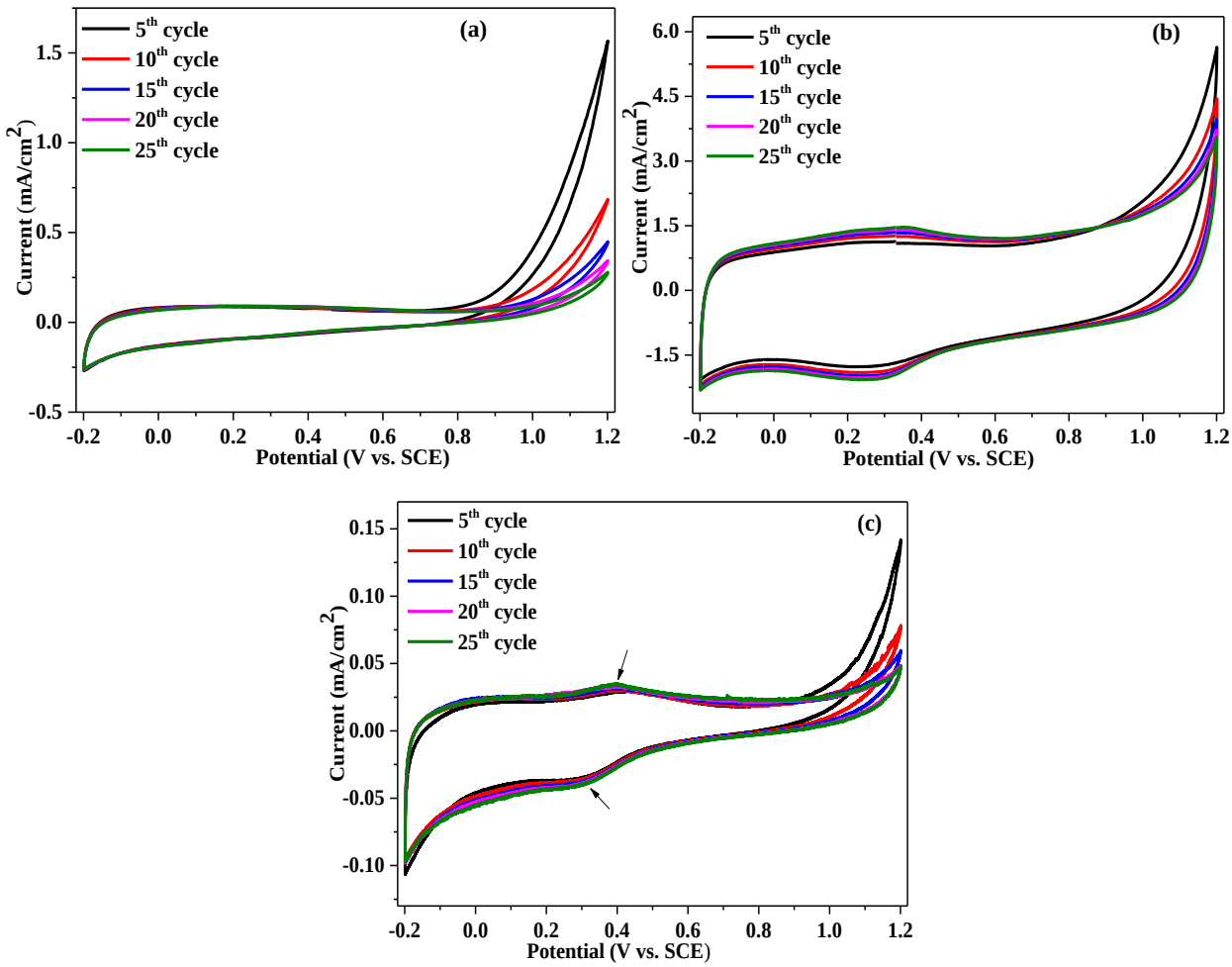

Figure 5.2: Cyclic voltammogram of samples **(a)** A600-10 **(b)** C800-10 and **(c)** H800-10 for Ist 25 cycles in 0.5 mol/L H_2SO_4; scan speed 30 mV/sec.

Furthermore at higher potential the decrement in the CV peaks with the increases in CV scans has been observed in **figure 5.2** for all samples. With the successive increase in the CV scans, consistent conversion of WC into WO_3 takes place with the emission of CO_2 as an anode by-product ($WC + 5H_2O \rightarrow WO_3 + CO_2 + 10\ H^+ + 10\ \bar{e}$) **[13]**. Since the formed WO_3 has very low solubility in the electrolyte **[14]** so it results to decreases the current gradually with the successive scans. With the decrease in potential towards cathodic sweep the anodic current is going to decrease due to the reduction of formed oxide(s) content on the prepared electrocatalysts. During reverse scan in the cathodic region the appearance of reduction peak (0.4 V-0.2 V *vs.* SCE) in the CV curve for samples C800-10 and H800-10 designates a reduction process (ORR) corresponding to reaction ($WO_3 + 2yH^+ + 2y\bar{e} \rightarrow WO_{3-y} + yH_2O;\ (0 < y < 1)$) **[15, 16]**. Such kind of process is possible only after considering the outer surface carbon layer around the WC nano particles as preferential active site for catalytic activity **[17]**. However, in the reverse scan in the cathodic region between 0.2 and -

0.2 V *vs.* SCE hydrogen atoms are adsorbed on the cathodic sweep ($WO_3 + x\,H + x\,\bar{e} \rightarrow H_xWO_3$) which desorbed on the anodic sweep. Due to the adsorption and desorption of the hydrogen on WO_3 a reversible redox process of WO_3/H_xWO_3 (Hydrogen tungsten bronzes; x=0.1–0.5) is also attributed in cyclic voltammograms [**8, 13, 18-20]**.

According to **Liu et al. [21]** tungsten bronzes are mildly soluble in acid media and can dissolve slowly. Also, it has been observed in **figure 5.2(b & c)** that the cathodic/anodic peak current intensity at lower potential region in case of sample C800-10 and H800-10 increases with the increase in CV cycles due to hydrogen adsorption/desorption process. It is because of the conversion of WC into WO_3 with increasing CV cycles which has also been reported by **Zhu et al. [8]**. Such a nature of current peak intensity indicates that the layer of anodic adsorbed WO_3 increases with the increases in CV cycles.

Moreover, the existence of redox peak with smaller difference (≈0.05 V) between the peaks position within the intermediate potential range in the CV curve obtained for sample C800-10 and H800-10 implies that the electron transfer process is more efficient. The presence of these redox peaks at lower potential for samples obtained especially by activated charcoal and hexane as carburizing agent proves it to be suitable candidate for low range potential applications without any supporting material (Pt, Pd etc.) and can be improved by platinizing the synthesized samples. Hence, the obtained results have confirmed that activity of prepared WC nano powder depends upon the reaction by which carbide is prepared (carburization by liquid hydrocarbon, solid carbon, and synthesis temperature).

Furthermore, the powder samples which has single phase WC has been platinized and observed its electrocatalytic activity in acidic media through CV curve as shown in **figure 5.3**. **Figure 5.4(a & b)** shows the XRD pattern of Pt/A600-10 and Pt/C800-10 respectively in which the diffraction peaks close to 39.5° and 46.1° can be assigned to Pt, demonstrating that the platinum precursor (H_2PtCl_6) has been successfully reduced to Pt nanoparticles. Moreover, the broad XRD diffraction peaks corresponding to Pt indicate a high dispersion of the Pt nanoparticles, which have a size of approximate 4 nm as calculated by using the Debye–Scherrer formula. The EDS elemental spectrum shown in **figure 5.4** also indicates the presence of carbon, oxygen, tungsten and platinum in the samples.

The elemental analysis clearly indicates that the electrode sample prepared by the current method consists of platinum along with tungsten carbide and carbon. The presence of O peak is due to the partial surface oxidation of WC nanoparticles during sampling **[22]**. By

comparing the CV curve for the carbide samples without **(figure 5.1)** and with platinum **(figure 5.3)**, it becomes clear that Pt modified samples displayed enhanced oxidation stability in H_2SO_4 by shifting the onset potential for oxidation at higher potential side in comparison to pure WC@C electrode.

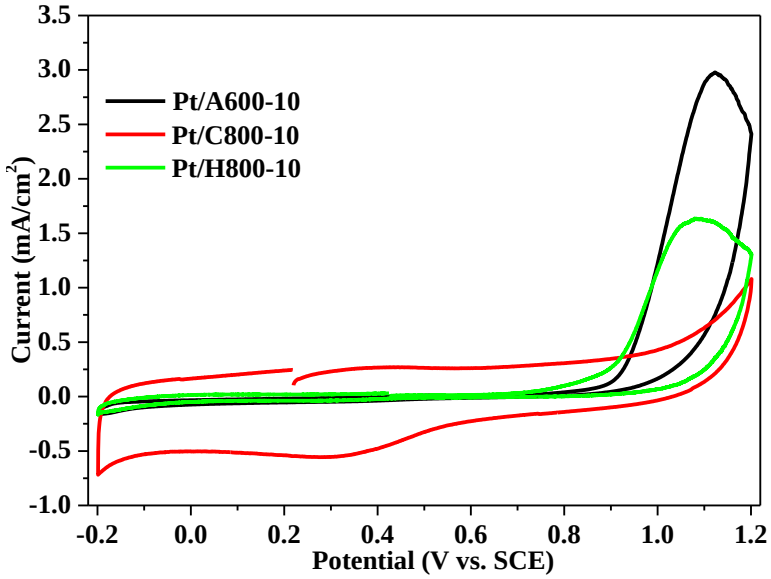

Figure 5.3: Cyclic voltammogram of samples synthesized by **(a)** Pt/A600-10 **(b)** Pt/C800-10 **(c)** Pt/H800-10 after Ist cycle in 0.5 mol/L H_2SO_4; scan speed 30 mV/sec.

The electrochemically active surface areas (ECSA) of Pt deposited electrocatalysts on the samples is also determined from the charge densities involved in the under potential deposition (UPD) processes of hydrogen adsorption/desorption by using relation $ECA = Q_H/Q_S$ **[3, 23]**. In our experiment the values of Q_H for hydrogen adsorption on Pt deposited WC samples have been measured by integrating I-V curve in the potential region -0.2 to 0.1 V *vs.* SCE in CV curve (**figure 5.3**). By dividing the value of Q_S (210 µC/cm^2) **[3]**, the ECSA of samples has been calculated and mentioned in **table 5.1**. According to **Liu et al. [24]** the core-shell nanoparticles have higher structural stability and maintained the electrochemical active area for the reactions. It has also been found from the data shown in **table 5.1,** that Pt/C800-10 acquired larger ECSA as compared to Pt/A600-10 and Pt/H800-10 electrodes. This higher value of ECSA can be attributed to the unique multimodal porous structure of WC with large specific surface area, which not only allows better dispersion of Pt catalyst but also facilitates the charge transfer at the Pt/WC interface.

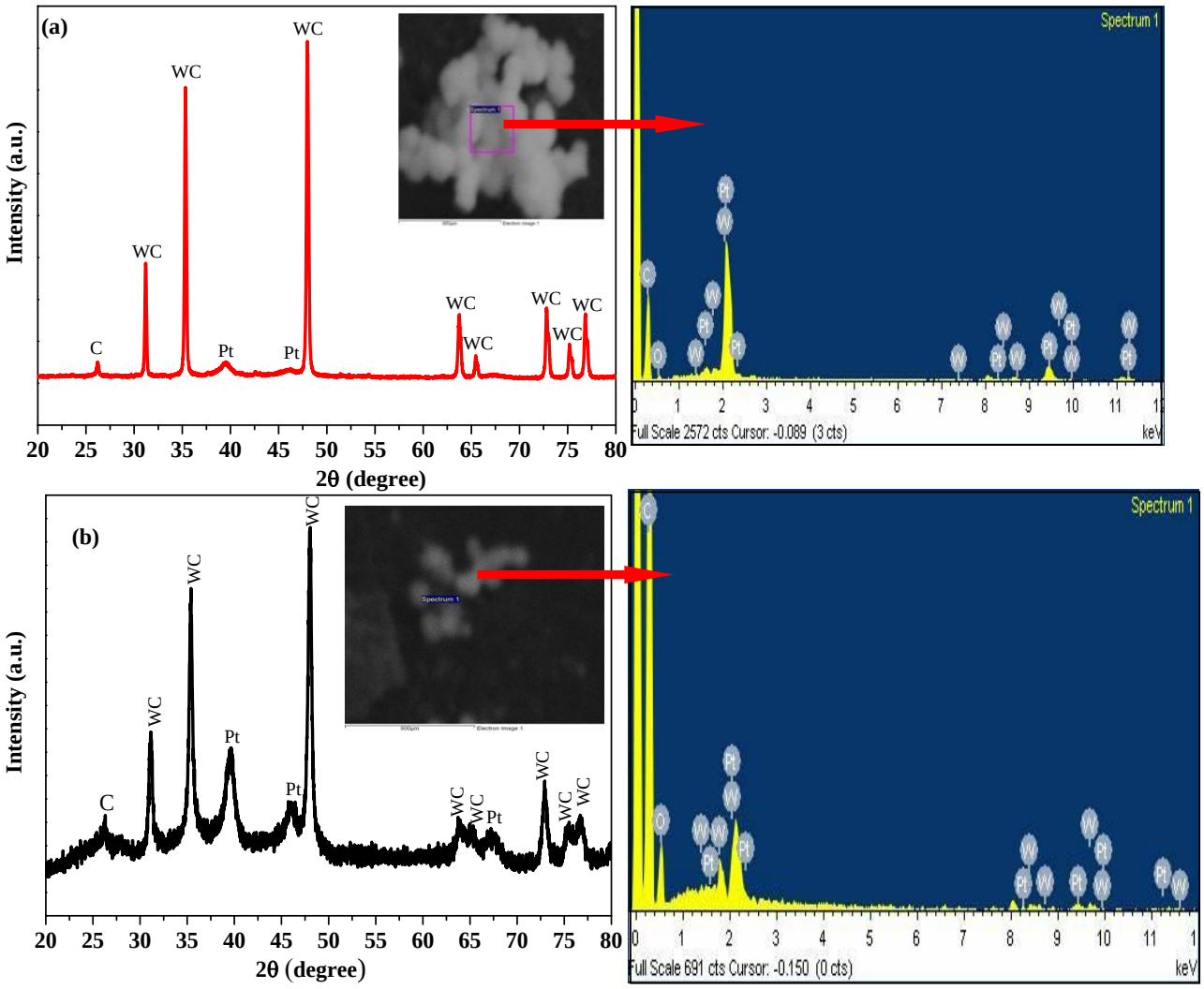

Figure 5.4: XRD pattern, SEM micrograph (inset) and EDS spectra of **(a)** Pt/A600-10 **(b)** Pt/C800-10. Elemental spectra correspond to the spectrum 1 point on the SEM micrograph.

The CV curves with successive scans after the deposition of platinum on the samples are shown in **figure 5.5**. **Figure 5.5(b & c)** attributes the shifting of 0.03 V in the redox peaks appeared in the intermediate potential range (0.2 V and 0.4 V) towards higher side for samples Pt/C800-10 and Pt/H800-10. The shifting displays the enhancement in oxidation stability of samples in acidic media during forward anodic sweep as well as oxygen reduction reaction (ORR) during cathodic sweep. But in case of sample obtained by acetone as carbon source (A600-10) after the Pt deposition, the CV curve as shown in **figure 5.5(a)** shows a minor peak during reverse scan at ~0.42 V which also corresponds to the reduction activity (ORR).

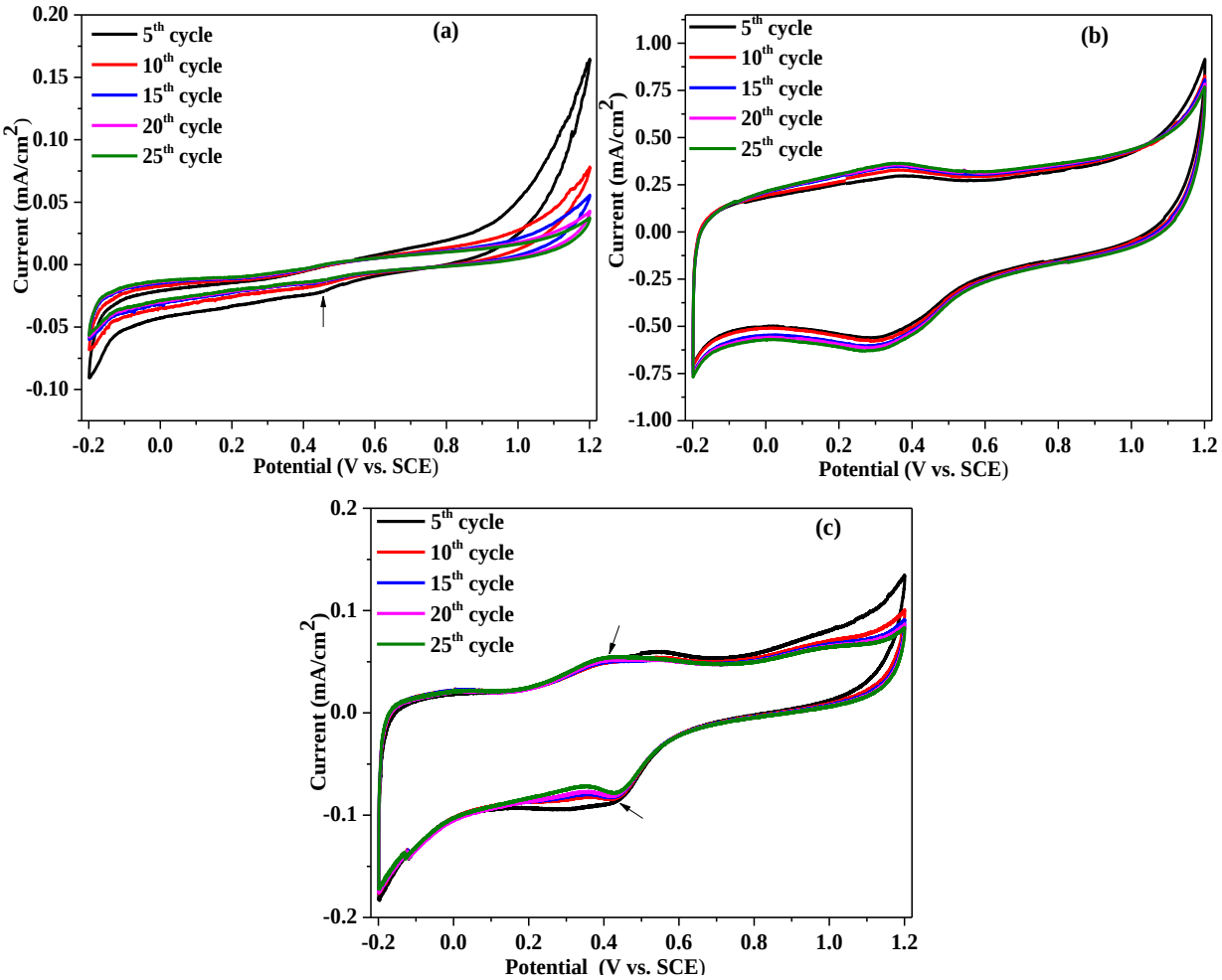

Figure 5.5: Cyclic voltammogram of samples **(a)** Pt/A600-10 **(b)** Pt/C800-10 and **(c)** Pt/H800-10 for Ist 25 cycles in 0.5 mol/L H_2SO_4; scan speed 30 mV/sec.

The appearance of the reduction peak at the respective potentials for platinized carbide samples in the range 0.30-0.45 V *vs.* SCE attribute its better characteristics in the reduction reaction as compared to $(Pt)_4$-RGO, $(Pt)_4$-WC/RGO, $(Pt:Ru)_4$-RGO samples reported by **Shi et al. [25].** The results obtained from current system are also comparable to results obtained by **Engelbrekt et al. [26]** for Pt nano particles used as electrocatalyst. Such kind of shifting as well as appearances of reduction peak after platinum deposition on the samples attributes the contribution of platinum towards the catalytic activity which is not observed by **Weigert et al. [27]** in their work. Moreover, the peak shape at lower potential region (-0.2 and -0.1 V *vs.* SCE) attributes clearly that hydrogen adsorption and desorption process is also promoted after the deposition of Pt on the carbide samples. On comparing the results with pure WC in **figure 5.2**, it has been observed that WC alone without Pt shows little activity for the hydrogen adsorption/desorption under the same electrochemical conditions. The process of hydrogen adsorption after the platinum deposition on the samples consists of two steps:

hydrogen may adsorb Ist on Pt and then migrate into formed WO_3 by hydrogen spillover mechanism **[8]**.

Moreover, after platinizing the samples, the trend of the consistent increment in the intensities of the redox peaks during anodic/cathodic sweep at lower potential with CV scans also indicates the production of more WO_3 which has been followed by only Pt/C800-10 sample **(figure 5.5(b))**. However, the CV curves in **figure 5.5(a & c)** observed for Pt/A600-10 and Pt/H800-10 shows that the cathodic current at lower potential region is being decreased regularly with the successive scan due to the decrease in surface area caused by the WO_3 coverage **[28]**. Hence, after the formation of oxide layer, the surface of electrocatalyst becomes rough and deformed. Due to this reason the detachment and agglomeration of Pt on WC surface takes place which results in elimination of the cooperative effect of Pt/WC catalyst **[21]**.

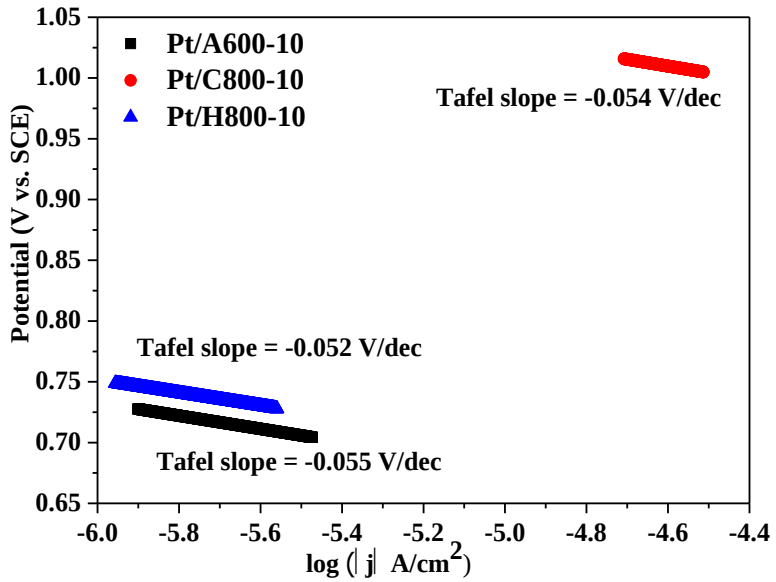

Figure 5.6: Tafel slope of ORR obtained with sample **(a)** Pt/A600-10 **(b)** Pt/C800-10 and **(c)** Pt/H800-10 in 0.5 mol/L H_2SO_4.

Figure 5.6 shows the Tafel diagram obtained for all the Pt deposited samples during cathodic scan. This shows a linear relation between logarithm current density and potential. It gives the values of Tafel slope of the same order which is usually reported for Pt catalyzed ORR reaction by other authors **[29, 30]**. The value of exchange current density can also be obtained by the extrapolation of the Tafel line to the equilibrium potential for the ORR **[30]**.

Table 5.1: Kinetic data obtained from the analysis of current-potential data of the polarization curve in 0.5 mol/L H_2SO_4 on Pt/A600-10, Pt/C800-10 and Pt/H800-10 catalysts.

Samples	ECSA (cm^2)	Onset potential (V) *vs.* SCE	Tafel slope (V/dec)	Exchange current density (A/cm^2)
Pt/A600-10	0.37	0.738	-0.054	7.86×10^{-7}
Pt/C800-10	2.42	1.039	-0.055	1.07×10^{-5}
Pt/H800-10	0.56	0.768	-0.052	3.82×10^{-7}

The calculated exchange current density corresponding to all electrocatalyst is given in **table 5.1**. The comparison of data shows that the exchange current density obtained for Pt/C800-10 catalyst display two orders of magnitude higher than Pt/A600-10 and Pt/H800-10 catalyst. Moreover, the observed onset potential for the ORR is on higher side for electrocatalyst Pt/C800-10 as compared to other electrodes. Hence all these parameters indicate that the electrocatalyst prepared by solid carburizing agent attributes better catalytic activity towards ORR.

5.1.1 Methanol and ethanol electro-oxidation

The performance of platinum deposited WC@C as an anode electrocatalysis was also evaluated by studying the alcohol electro oxidation. The CV curves shown in **figure 5.7** were obtained at room temperature for methanol and ethanol electro-oxidation on platinized samples in 0.5 mol/L H_2SO_4 containing 0.5, 0.7 and 0.9 mol/L organic molecule (methanol/ethanol). The electro-oxidation of methanol and ethanol is a 6-electron ($CH_3OH + H_2O \rightarrow CO_2 + 6H^+ + 6\bar{e}$) and 12-electron ($CH_3CH_2OH + 3H_2O \rightarrow 2CO_2 + 12H^+ + 12\bar{e}$) process respectively and takes place on Pt support through several intermediates products **[26, 31-34]**. **Figure 5.7** shows the broad feature of the peak in the CV curve after the addition of organic molecules which indicates that the methanol/ethanol has been oxidized within this potential range. One main anodic peak in the range 0.55-0.65 V *vs.* SCE in **figure 5.7(a, c & e)** during the forward scan represents the oxidation of methanol.

In **figure 5.7(b, d & f)** the I^{st} anodic peak at ~0.62 V *vs.* SCE during forward scan represents the oxidation of ethanol. While on the other hand the second peak ~1.0 V *vs.* SCE arise due to the further oxidation of intermediate products **[35]**. Hence it is clear that the catalyst shows good catalytic behavior for the electro-oxidation of both alcohols (methanol/ethanol). In the forward scan the Pt/A600-10 electrode has shown oxidation peak

for methanol and ethanol at higher potential as compared to other two electrodes Pt/C800-10 and Pt/H800-10 prepared by using activated charcoal and hexane as carburizing agent respectively. Moreover, **figure 5.7(c & d)** clearly reveals that for Pt/C800-10 electrocatalyst, the onset potential of methanol and ethanol oxidation shifts to lower potential with the increase in methanol/ethanol concentration due to the enhanced alcohol diffusion. According to **Huang et al. [36]** the increased alcohol concentration accelerates the diffusion of alcohol to the interface of catalysts and eventually promotes the reaction. One of the aspects of shifting of the onset potential is also related to the presence of oxygen-containing functional groups on the prepared samples **[37]**. These oxygen-containing functional groups could also promote the diffusion of intermediates oxide of alcohol. The presence of oxygen on the surface of sample C800-10 may be due to its higher specific surface area (522.5 m^2/g) which enhances its activity towards higher affinity with atmospheric oxygen. The peak potential for forward (E_f) and reverse (E_b) scan corresponding to each electrocatalysts has been given for 0.5 mol/L H_2SO_4+0.9 mol/L CH_3OH/C_2H_5OH in **table 5.2**. However, it has also been observed that both the current density corresponding to forward anodic peak current (I_f) and the backward anodic peak current (I_b) for electro-oxidation of methanol and ethanol on Pt/C800-10 is much higher than that on Pt/A600-10 and Pt/H800-10.

In the CVs, the anodic peak in the reverse scan for platinum deposited sample (Pt/WC@C) attributes to the removal of the incomplete oxidized carbonaceous species formed in the forward scan **[3].** Further the value of I_f/I_b can be used to evaluate the catalyst tolerance to the intermediate carbonaceous species formed via decomposition of fuel (ethanol/methanol) and accumulated on the electrode surface **[38]**. Normally the low I_f/I_b ratio indicates the poor oxidation of alcohol to carbon dioxide during the anodic scan and excessive accumulation of carbonaceous residues on the catalyst surface **[3]**.

Therefore the values of I_f/I_b ratio obtained from **table 5.2** reveals that prepared electrocatalysts exhibits less accumulation of intermediate carbonaceous species and good anti-poisoning ability while using methanol as fuel as compared to ethanol. Moreover, based on the dependence of current (I) on the concentration (c) of alcohol, the reaction rate constant (k) can also be calculated by using relation between I and c as **[36, 39]**:

$$I = kc^n \tag{5.1}$$

$$log(I) = log(k) + nlog(c) \tag{5.2}$$

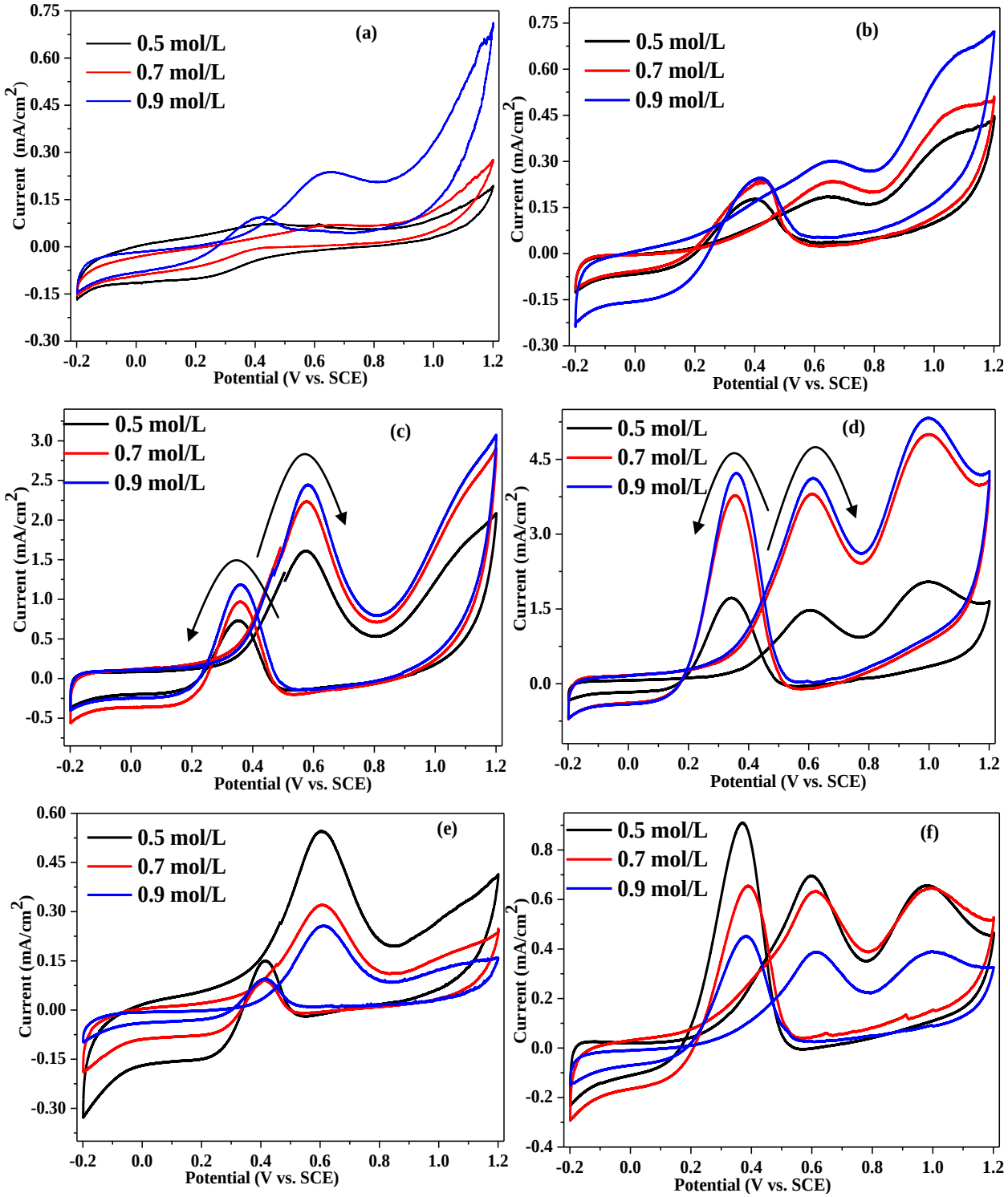

Figure 5.7: Cyclic voltammogram of **(a,b)** Pt/A600-10 **(c,d)** Pt/C800-10 and **(e,f)** Pt/H800-10 catalysts in 0.5 mol/L H_2SO_4 with 0.5, 0.7 and 0.9 mol/L of methanol **(a, c & e)** and ethanol **(b, d & f)**.

where I is the peak current density, k is the reaction rate constant, c is the bulk concentration of methanol and n is the reaction order. The observed values of reaction rate constant (k) for Pt/C800-10 catalyst are 2.72 and 5.75 for methanol and ethanol electro-oxidation respectively. These values are observed to be higher than the other electrocatalyst Pt/A600-10 ($k_{methanol}$ = 0.231, $k_{ethanol}$ = 0.835) and Pt/H800-10 ($k_{methanol}$ = 0.216, $k_{ethanol}$ = 0.375).

Further, in order to evaluate the kinetic parameters (exchange current density and Tafel slope) associated with the catalytic activity of prepared electrocatalyst for MOR and EOR, the plots of electrode potential against the logarithm current density are drawn in **figure 5.8** for 0.9 mol/L concentrations of methanol and ethanol. The exchange current density and Tafel slope for cathodic process are evaluated by using equations (5.3) and (5.4) [**2, 40**].

$$E = a + b \log i \tag{5.3}$$

where

$$a = E_r - b \log i_o \tag{5.4}$$

$$\eta = E - E_r = b \log \left(\frac{i}{i_o}\right) \tag{5.5}$$

In this equation "b" is termed as the Tafel slope (in V/dec) and is given by the relation as $b = \frac{2.303\ RT}{\alpha F}$ where α is the product of an electron transfer coefficient and number of electron transferred in rate determining step, f is Faraday's constant (96485.3 C/mol), T is absolute temperature, R is universal gas constant (8.314 J/mol K), "i" is the apparent current density (in A/cm^2), E_r is reversible potential in (V *vs.* SCE) and η is the overpotential. Eq. (5.3) is a linear equation and can be used to evaluate the value of constant "a" and "b" from the slope and intercept of the plot of E *vs.* $\log i$, respectively. The exchange current i_o of a given electrode reaction is calculated by using the value of a and b after putting E_r=0.6 V.

The values of exchange current density and Tafel slope obtained for 0.9 mol/L methanol and ethanol is given in **table 5.2**. The higher value of exchange current density obtained from methanol oxidation as compared to ethanol oxidation suggests that the prepared electrocatalyst has a higher catalytic activity for the electro-oxidation of methanol. Among all the data obtained for methanol oxidation, Pt/C800-10 catalyst gives the largest current density as compared to Pt/A600-10 and Pt/H800-10. These values further suggest that Pt/C800-10 catalyst has higher catalytic activity for methanol oxidation.

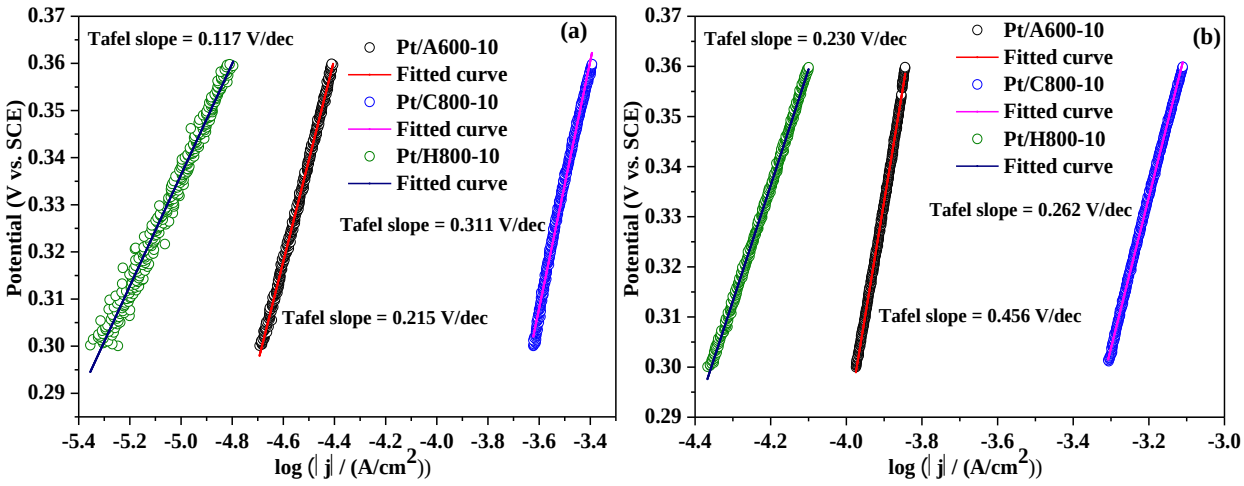

Figure 5.8: Tafel plot obtained from the rising portion of the forward anodic peak of CV curve on Pt/A600-10, Pt/C800-10 and H800-10 in **(a)** 0.5 mol/L H_2SO_4 + 0.9 mol/L CH_3OH **(b)** 0.5 mol/L H_2SO_4 + 0.9 mol/L CH_3CH_2OH solutions.

It arises due to the fact that high crystallinity of WC in the samples A600-10 and H800-10 may weaken its combination with platinum **[41]**. On the other hand sample C800-10 exhibits high activity toward methanol oxidation because of higher mesoporosity in the sample which results to good combination with platinum **[41]**. Moreover, the obtained higher value of current density for methanol as fuel clearly attributes the weak interaction of carbonaceous species with the electrocatalyst.

The enhanced electrochemical activity of the core-shell (WC@C) nano structured C800-10 catalyst is due to two main reasons. First, the presence of amorphous carbon around WC modifies the dispersion of Pt nano particles and influences the chemi-adsorption of methanol and ethanol poisoning species (CO). Secondly, the amorphous carbon around the WC assists in formation of a microcrystalline Pt thin film, which strongly influences the surface atom densities and chemical reactivity.

Table 5.2: Kinetic data obtained from the analysis of current–potential data of the polarization curve of the electro-oxidation of 0.9 mol/L CH_3OH and 0.9 mol/L CH_3CH_2OH in 0.5 mol/L H_2SO_4 on Pt/A600-10, Pt/C800-10 and Pt/H800-10 catalysts.

		Pt/A600-10	**Pt/C800-10**	**Pt/H800-10**
Methanol	E_f	0.64	0.58	0.61
	E_b	0.40	0.36	0.41
	I_f/I_b	2.5	2.1	2.68
	Intercept "*a*"	1.308	1.296	0.926
	Tafel slope "*b*" (V/dec)	0.215	0.311	0.117
	i_o at 0.6V (A/cm^2)	5.10×10^{-4}	5.79×10^{-3}	1.60×10^{-3}
	α	0.276	0.191	0.508
Ethanol	E_f	0.66	0.61	0.61
	E_b	0.41	0.36	0.38
	I_f/I_b	1.23	0.97	0.86
	Intercept "*a*"	2.112	1.253	1.306
	Tafel slope "*b*" (V/dec)	0.456	0.262	0.230
	i_o at 0.6V (A/cm^2)	4.84×10^{-4}	3.20×10^{-3}	8.40×10^{-4}
	α	0.130	0.227	0.258

5.2 Electrochemical study of W_2C nanopowder

Among all the synthesized products produced during the fast cooling of autoclave, the cyclic voltammogram (CV) have been done for samples (A600-2-10, C600-2-0.5, H600-2-10) which contained higher amount of W_2C phase. It has been done in acidic solution (0.5 mol/L H_2SO_4) and the results are shown in **figure 5.9** for Ist cycle by normalizing the electrode area after considering the anodic current to be positive. Since the onset potential for oxidation of sample corresponds to its starting of corrosion process. So, the CV curve also gives an idea about the corrosion resistance of sample in terms of oxidation stability which is revealed by observing the shifting in onset potential for anodic current at higher potential. Hence the appearance of higher onset potential for oxidation of sample H600-2-10 as compared to other electrode attributes its higher corrosion resistance/ oxidation stability in acidic media. However, the existence of onset potential for oxidation in sample C600-2-0.5

towards lower potential may be due to its higher surface area which attributes the enhancement activity towards oxygen affinity. Such kind of shifting in onset potential clearly reveals that the stability of electrode towards electrochemical reaction changes by changing the carburizing agent.

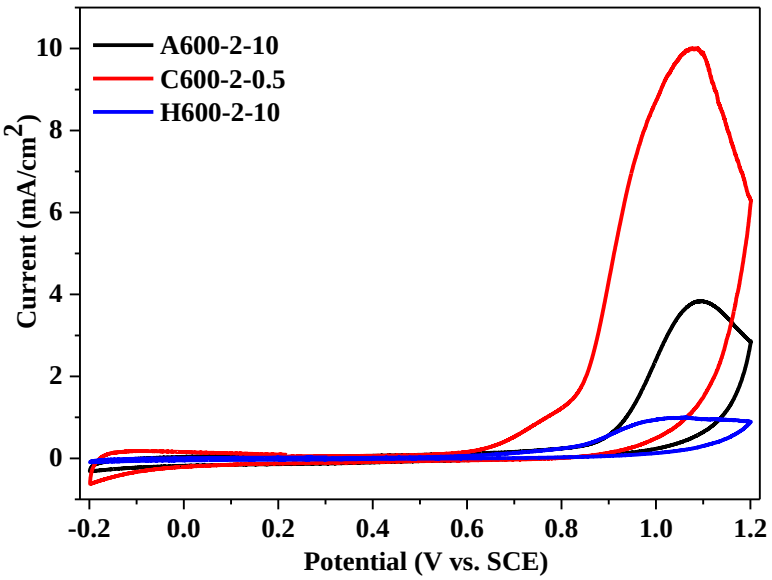

Figure 5.9: Cyclic voltammogram of samples synthesized by **(a)** A600-2-10 **(b)** C600-2-0.5 and **(c)** H600-2-10 after Ist cycle in 0.5 mol/L H_2SO_4; scan speed 30 mV/sec.

At higher potential the abrupt increment in the anodic current above ~0.9 V *vs.* SCE designates that obtained carbide sample got converted completely into WO_3 as the potential of the working electrode increases linearly **[8, 11, 12]**. In order to understand the electrochemical reaction, the CV curve has been plotted with successive scans as shown in **figure 5.10**. The electrochemical reactions that occur on the surface of as has been observed in the **figure 5.10** can be considered through three regions. The lower potential region (-0.2 to 0.2 V) in which the initiation of oxidation of product occur and the onset potential shifts to higher potential with successive scans. It arises due to the formation of oxide layer on the electrode at higher potential which delayed its oxidation. In the intermediate potential region (0.2 V to 0.8 V) the CV curve persist linear behavior until second oxidation process is initiated. Furthermore at higher potential region the decrement in the CV peaks in successive CV scans has been observed and shown in **figure 5.10** for all samples. The carbide samples slowly oxidize to WO_3 during each process of successive increase in the CV scans.

As discussed earlier, the formed inactive surface layer of WO_3 with the emission of CO_2 as an anode by-product has very low solubility in the electrolyte and it results to decreases the

current gradually **[14]**. Furthermore, it has been observed that with the decrease in potential towards cathodic sweep the anodic current is going to decrease due to the reduction of formed oxide(s) content on the prepared electrocatalyst.

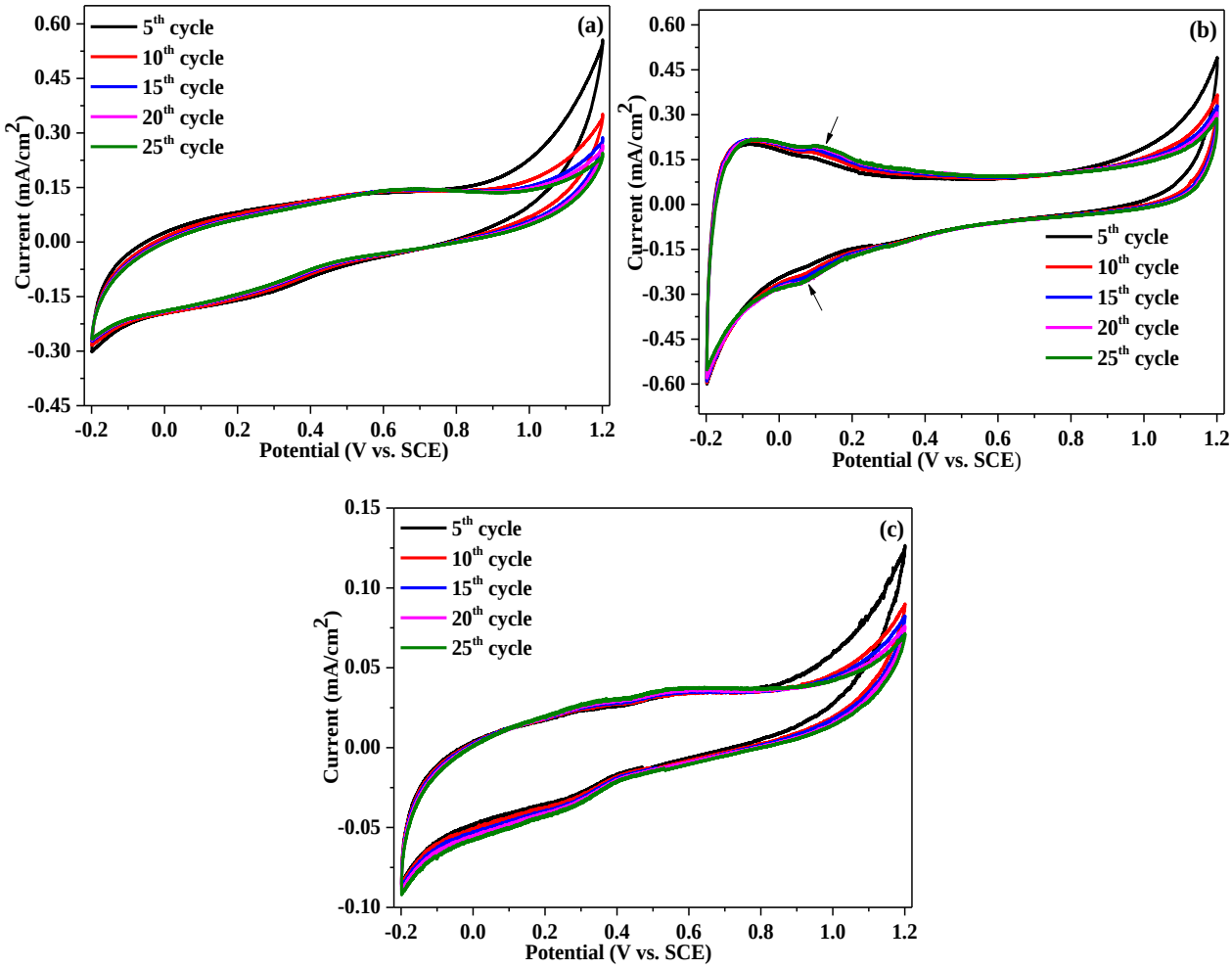

Figure 5.10: Cyclic voltammogram of samples **(a)** A600-2-10 **(b)** C600-2-0.5 and **(c)** H600-2-10 for Ist 25 cycles in 0.5 mol/L H_2SO_4; scan speed 30 mV/sec.

During the reverse scan, redox peaks have appeared between 0.15 and 0.05 V *vs.* SCE in the CV curve obtained for samples C600-2-0.5. It corresponds to adsorption of hydrogen atoms at 0.07 V *vs.* SCE on the cathodic sweep and desorption of hydrogen atom 0.11 V *vs.* SCE on the anodic sweep. This result has also been reported by Shim et al. **[15]** for their system Pt-WO_3/C and indicates that without Pt deposition the prepared sample in our case attributes comparable results of hydrogen adsorption and desorption process. According to them the position of these peaks does not correspond to strongly bonded hydrogen.

On comparing the results of **figure 5.2(b)** and **figure 5.10(b)**, it is clear that the presence of W_2C/W in the carbon coated sample (C600-2-0.5) promote the process of hydrogen

intercalation/de-intercalation which has not been observed in carbon coated C800-10 sample containing single phase of WC. Also, it has been observed that the cathodic/anodic peak current intensity in case of sample C600-2-0.5 due to hydrogen adsorption/desorption increases with the increase in CV cycles. It is because of the formation of WO_3 with the increase in CV cycles **[8]**. The smaller difference (≈0.04 V) between these peaks implies that the electron transfer process is more efficient. The presence of these redox peaks at lower potential for samples obtained especially by activated charcoal (C600-2-0.5) proves it to be suitable candidate as electrocatalyst without any supporting material (Pt, Pd etc.) and can be improved by platinization of the synthesized samples. While on the other hand, the CV curve obtained for sample A600-2-10 and H600-2-10 has not shown any such peak at lower potential. Moreover, the intensity of anodic and cathodic current at lower potential also decreases with CV cycles due to the formation of WO_3 which decreases its active surface area regularly. Hence, this result indicates that the sample prepared by acetone and hexane attributes its inertness towards HER/HOR/ORR process.

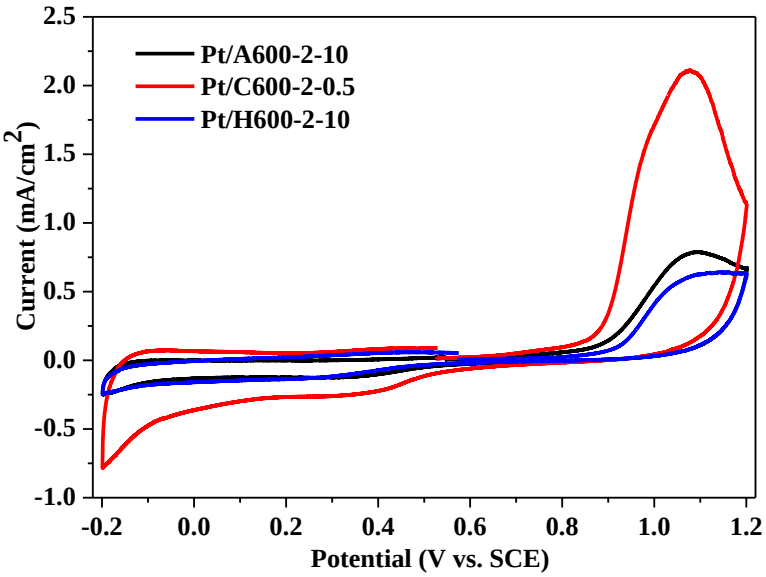

Figure 5.11: Cyclic voltammogram of samples synthesized by **(a)** Pt/A600-2-10 **(b)** Pt/C600-2-0.5 and **(c)** Pt/H600-2-10 after Ist cycle in 0.5 mol/L H_2SO_4; scan speed 30 mV/sec.

In order to investigate the effect of platinum deposition on the electrocatalytic activity of the powder samples, it has been platinized and analyzes their electrocatalytic activity in acidic media through CV curve is shown in **figure 5.11**. On comparing the CV curves for the prepared samples without **(figure 5.10)** and with platinum **(figure 5.11)**, it is clear that the

samples after Pt deposition attribute better oxidation stability in H_2SO_4 by shifting the onset potential for oxidation at higher potential side.

The electrochemically active surface areas (ECAs) of Pt deposited electrocatalysts is evaluated by using the relation $ECA = Q_H/Q_S$ **[3,23]** after integrating the I-V curve in between -0.2 and 0.1 V *vs.* SCE corresponding to the adsorption of atomic hydrogen at the surface of electrode. It helps to determine the charge densities (Q_H) in the hydrogen adsorption potential region in the CV curve. By dividing the value of Q_S (210 μC/cm^2) **[3]**, the electro active surface area of samples has been calculated and given in **table 5.3**. It has been observed from the data given in **table 5.3** that, Pt/C600-2-0.5 acquired larger ECSA as compared to Pt/A600-2-10 and Pt/H600-2-10 electrodes. This higher value of ECSA can be attributed to the porous structure of product having large specific surface area, which not only allows better dispersion of Pt catalyst but also facilitates the charge transfer at the catalyst/support (Pt/MC) interface.

The CV curves of samples after the deposition of platinum with successive scans is shown in **figure 5.12.** It displays the reduction peaks in the intermediate potential range 0.2 V and 0.4 V during cathodic sweep. These peaks directly attributes to the occurrence of oxygen reduction reaction (ORR) whose positions varied with the change in the electrode prepared by different carburizing agents as well as phase(s) content in the obtained product. The reduction peak corresponding to ORR process has appeared at ~0.41 V *vs.* SCE in the CV curve (**figure 5.12(b))** of Pt/C600-2-0.5 electrocatalyst. It indicates that after the platinum deposition, the ORR process dominates which suppresses the peaks of HER/HOR at lower potential range. But in case of samples synthesized by liquid carbon source (A600-2-10 and H600-2-10) the peak corresponds to ORR appeared at ~0.38 V *vs.* SCE. Hence, the presence of W_2C as well as initial carburizing agent have improved the ORR process in sample Pt/C600-2-0.5 by shifting the most prominent peak at higher potential as compared to pure WC electrode (**figure 5.5(b)**) and other electrodes (**figure 5.12(a & c)**).

Moreover, as discussed earlier the appearance of these peaks at this potential attribute its better characteristics in the reduction reaction as compared to $(Pt)_4$-RGO, $(Pt)_4$-WC/RGO, $(Pt:Ru)_4$-RGO samples reported by Shi et al. **[25]** as well as comparable to results presented by **Ma et al. [2]** for their system Pt-WC/RGO. However, after platinizing the samples, the trend of the consistent decrement in the intensities of the reduction peaks at ~0.41 V during cathodic sweep with CV scans indicates that the catalyst/support combination may not retain sufficient activity due to the consistent conversion of WC into WO_x on its surface. On further

decreasing the potential, the peak shape in the lower potential region (-0.2 and 0.2 V) attributes the hydrogen adsorption and desorption process. This process seems to be enhanced due to the contribution of both Pt and prepared carbides contents.

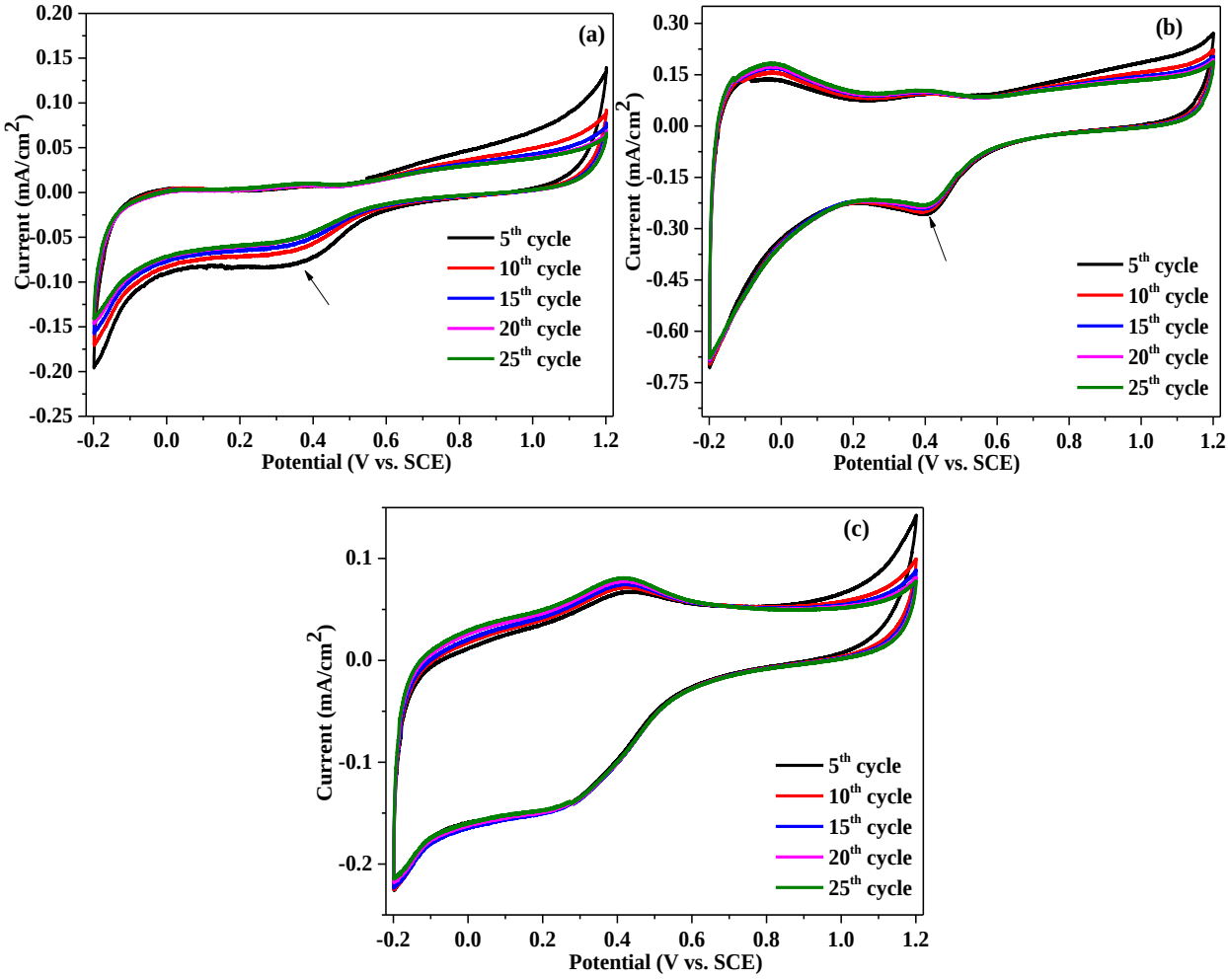

Figure 5.12: Cyclic voltammogram of samples **(a)** Pt/A600-2-10 **(b)** Pt/C600-2-0.5 and **(c)** Pt/H600-2-10 for Ist 25 cycles in 0.5 mol/L H_2SO_4; scan speed 30 mV/sec.

This result clearly indicates that carbides content alone without Pt shows little activity towards hydrogen adsorption and desorption. The decrement in the intensities of anodic and cathodic peaks corresponding to hydrogen adsorption/desorption for sample Pt/A600-2-10 and Pt/H600-2-10 is due to increased content of WO_3 as shown in **figure 5.12(a & c) [8]**. The reason behind the decrement in the overall catalytic activity of electrocatalyst is due to the formation of WO_3 because after the formation of oxide layer, the surface of electrocatalyst becomes rough and deforms due to which agglomeration of Pt occur and finally it is detached from the supported surface **[21]**.

Figure 5.13 displays the Tafel diagram for all the samples corresponding to ORR during cathodic scan. This shows a linear relation between logarithm current density and potential and gives the values of Tafel slope of the same order which has been reported for Pt catalyzed ORR reaction by other authors **[29, 30]**. The value of exchange current density has been obtained by the extrapolation of the Tafel line to the equilibrium potential for the ORR as discussed earlier. The calculated exchange current density corresponding to all electrocatalyst is given in **table 5.3**. The comparison of data shows that the exchange current density obtained for Pt/C600-2-0.5 catalyst gives one order of magnitude higher than Pt/H600-2-10 catalyst which has lower content of W_2C in the base prepared material. The effect of W_2C on the electrochemical activity can also be observed by comparing the results of catalyst Pt/A600-2-10 and Pt/A600-10. It reveals that the value of exchange current density as well as onset potential for ORR got modified on the introduction of W_2C in the prepared electrocatalyst. The onset potential for the ORR has also been observed to shift on higher side for electrocatalyst Pt/C600-2-0.5 as compared to others electrode.

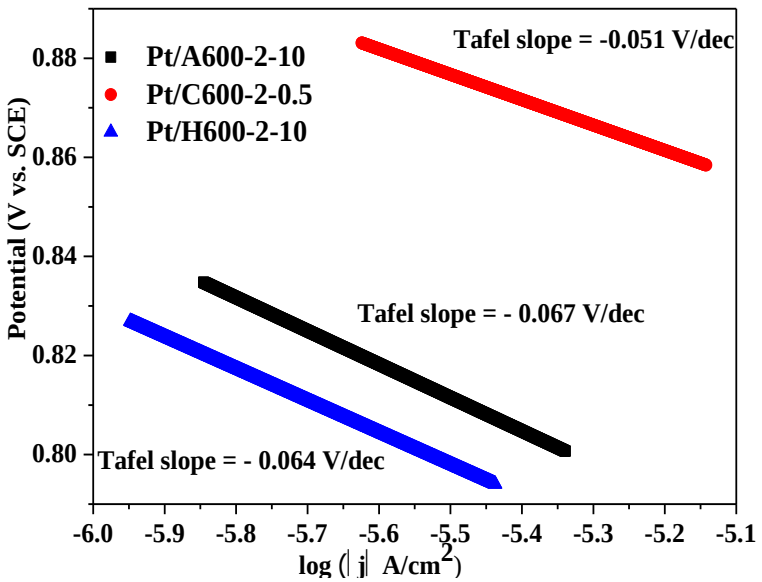

Figure 5.13: Tafel slope of ORR obtained with sample **(a)** Pt/A600-2-10 **(b)** Pt/C600-2-0.5 and **(c)** Pt/H600-2-10 in 0.5 M H_2SO_4.

Table 5.3: Kinetic data obtained from the analysis of current-potential data of the polarization curve in 0.5 mol/L H_2SO_4 on Pt/A600-2-10, Pt/C600-2-0.5 and Pt/H600-2-10 catalysts.

Samples	ECSA (cm^2)	Onset potential (V) *vs.* SCE	Tafel slope (V/dec)	Exchange current density (A/cm^2)
Pt/A600-2-10	0.51	0.845	-0.067	1.07×10^{-6}
Pt/C600-2-0.5	1.41	0.902	-0.051	1.73×10^{-6}
Pt/H600-2-10	0.41	0.842	-0.064	7.22×10^{-7}

5.2.1 Methanol and ethanol electro-oxidation studies

The effect of platinum deposition on the prepared samples for alcohol oxidation has been investigated by taking CV at room temperature as shown in **figure 5.14.** After the addition of organic molecule the broad feature of the peaks in the CV curves has been observed in **figure 5.14**, which indicates that the methanol/ethanol has been oxidized within the scan potential range. One main anodic peak in the range 0.50-0.65 V *vs.* SCE in **figure 5.14(a, c & e)** during the forward scan represents the oxidation of methanol. While in **figure 5.14(b, d & f)** I^{st} anodic peak at ~0.6 V during the forward scan represents the oxidation of ethanol and the second peak at ~1.0 V corresponds to the further oxidation of intermediate products. In the forward scan the Pt/A600-2-10 electrocatalyst has shown oxidation peak for methanol electro-oxidation at higher potential as compared to other two electrocatalyst Pt/C600-2-0.5 and Pt/H600-2-10. The peak potential for forward (E_f) and reverse (E_b) scan corresponding to each electrocatalysts for 0.5 mol/L H_2SO_4+0.9 mol/L CH_3OH/C_2H_5OH has been given in **table 5.4**. In the CVs curve, the observed anodic peak in the reverse scan for platinum deposited samples attributes to the removal of the incomplete oxidized carbonaceous species formed in the forward scan **[3].**

Moreover, as discussed earlier the value of I_f/I_b can be used to evaluate the catalyst tolerance to the intermediate carbonaceous species formed via decomposition of ethanol/methanol and accumulated on the electrode surface **[38]**. The variation in the value of I_f/I_b for all electrocatalysts has been also given in **table 5.4.** It suggests that depending upon the structural and surface properties of electrocatalyst, their tolerance to carbonaceous species accumulation has changed during methanol as well as ethanol electro-oxidation. Normally low I_f/I_b ratio indicates the poor oxidation of alcohol to carbon dioxide during the anodic scan and excessive accumulation of carbonaceous residues on the catalyst surface **[3]**. The higher

values of I_f/I_b ratio obtained for respective electrocatalysts as given in **table 5.4** reveals that prepared electrocatalysts exhibit less accumulation of intermediate carbonaceous species and good anti-poisoning ability while using methanol as fuel as compared to ethanol. However, on the basis of I_f/I_b ratio it can be said that electrocatalyst Pt/C600-2-0.5 attributes moderate behavior for both alcohol oxidations. The variations in the alcohol oxidation with different electrocatalyst have also been studied and shown in **figure 5.14**. It clearly reveals that for electrocatalyst Pt/C600-2-0.5, the onset potential of methanol and ethanol oxidation shift to lower potential with the increase in the methanol/ethanol concentration. It may be due to the enhanced alcohol diffusion to the interface of catalysts which eventually promotes the reaction with the increment in the alcohol concentration **[36]**.

However, as discussed earlier one of the aspects of shifting in the onset potential is also related to the presence of oxygen-containing functional groups on the prepared sample which could also promote the diffusion of intermediates oxide of alcohol **[37].**The presence of oxygen on the surface of sample C600-2-0.5 may be due to its higher specific surface area (27.7 m^2/g) which enhances its activity exhibiting higher affinity with atmospheric oxygen. Similar to discussion done in case of electrochemical study for alcohol oxidation by pure WC the reaction rate constant (k) can also be determined by using relation between I and c given in equations (5.1) and (5.2)

The obtained values of reaction rate constant for Pt/A600-2-10 and Pt/C600-2-0.5 are ($k_{methanol}$ = 0.255 and $k_{ethanol}$ = 0.071) and ($k_{methanol}$ = 0.039 and $k_{ethanol}$ = 0.138) respectively. These values are observed to be higher than the other electrocatalyst Pt/H600-2-10 ($k_{methanol}$ = 0.003 and $k_{ethanol}$ = 0.004) which attributes that Pt deposition on H600-2-10 has not improved the electrochemical properties of W_2C contained H600-2-10 electrocatalyst towards alcohol electro-oxidations.

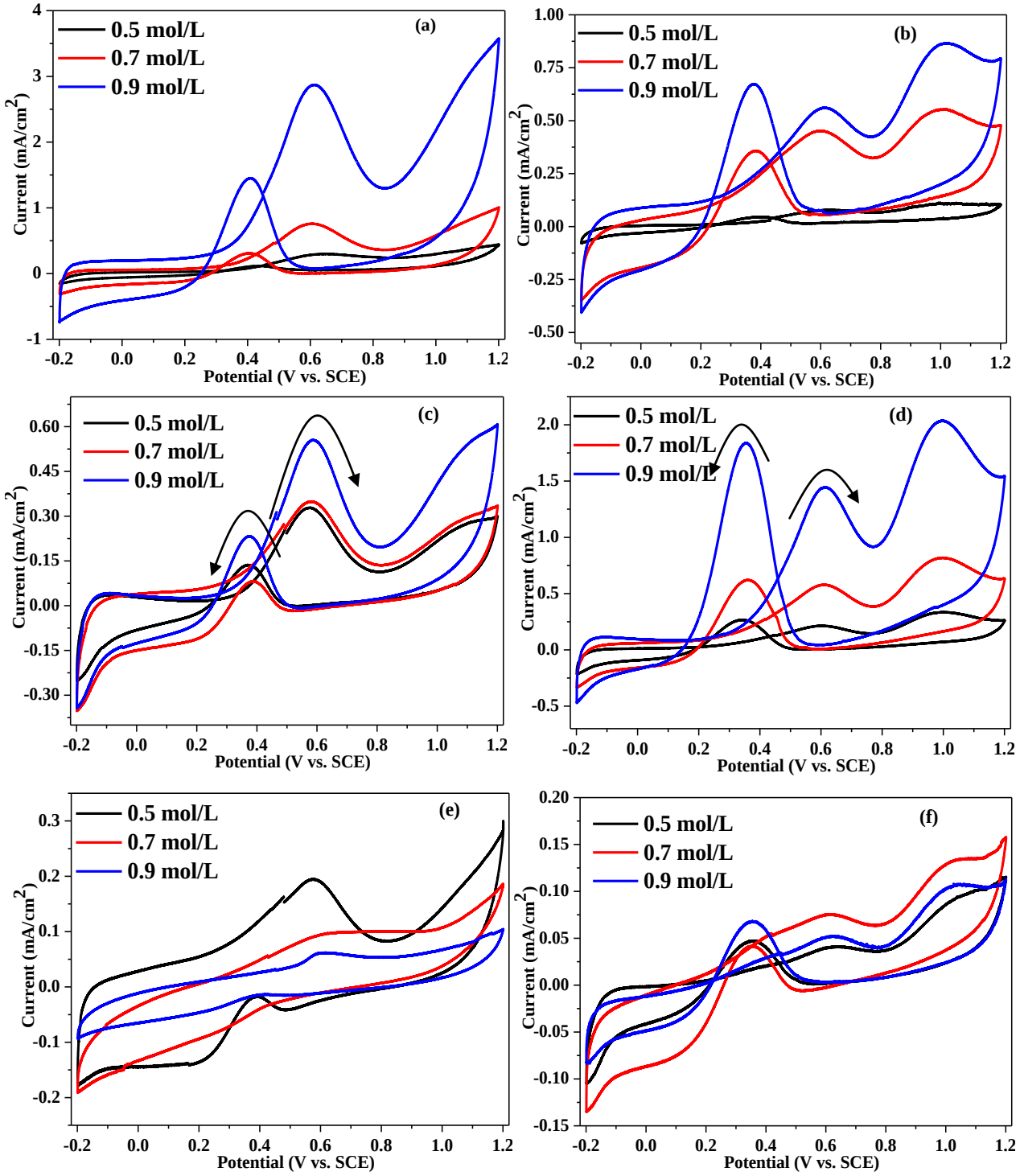

Figure 5.14: Cyclic voltammogram of **(a-b)** Pt/A600-2-10 **(c-d)** Pt/C600-2-0.5 and **(e-f)** Pt/H600-2-10 catalysts in 0.5 mol/L H_2SO_4 with 0.5, 0.7 and 0.9 mol/L of methanol **(a, c & e)** and ethanol **(b, d & f)**.

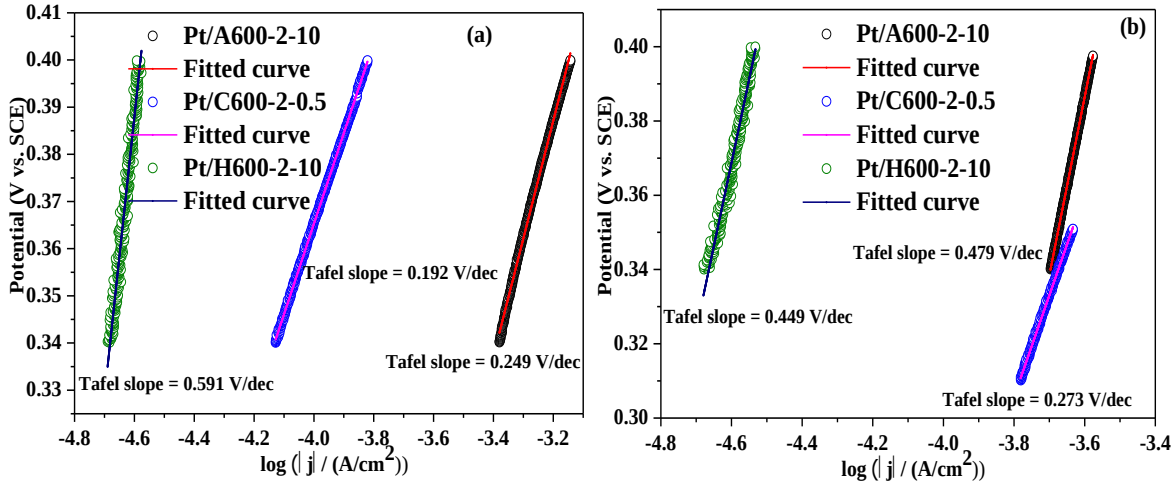

Figure 5.15: Tafel plot obtained from the rising portion of the forward anodic peak of CV curve on Pt/A600-2-10, Pt/C600-2-0.5 and H600-2-10 in **(a)** 0.5 mol/L H_2SO_4 + 0.9 mol/L CH_3OH **(b)** 0.5 mol/L H_2SO_4 + 0.9 mol/L CH_3CH_2OH solutions.

Further, in order to evaluate the kinetic parameters associated with the catalytic activity of prepared electrocatalyst for MOR and EOR, the plots of electrode potential against the logarithm current density are drawn and shown in **figure 5.15** for 0.9 mol/L concentration of methanol/ethanol. The exchange current density and Tafel slope have been calculated with the help of equations (5.3) and (5.4), the respective values have been given in **table 5.4**.

The value obtained from **table 5.4** shows that Pt/C600-2-0.5 catalyst exhibit higher exchange current density as compared to other electrocatalysts. Hence, it suggests that electrocatalyst prepared by solid-sate carburizing agent have higher catalytic activity for alcohol electro oxidation. Moreover, the obtained higher value of exchange current density of C600-2-0.5 by using methanol as fuel attributes its weak interaction with carbonaceous species and suggests better electrocatalyst for methanol electro-oxidation.

Table 5.4: Kinetic data obtained from the analysis of current–potential data of the polarization curve of the electro-oxidation of 0.9 mol/L CH_3OH and 0.9 mol/L C_2H_5OH in 0.5 mol/L H_2SO_4 on Pt/A600-2-10, Pt/C600-2-0.5 and Pt/H600-2-10 catalysts.

		Pt/A600-2-10	**Pt/C600-2-0.5**	**Pt/H600-2-10**
Methanol	E_f	0.62	0.59	0.60
	E_b	0.41	0.38	0.40
	I_f/I_b	2	2.43	4.32
	Intercept "*a*"	1.133	1.186	3.107
	Tafel slope "*b*" (V/dec)	0.192	0.249	0.591
	i_o at 0.6V (A/cm^2)	1.67×10^{-3}	4.43×10^{-3}	5.72×10^{-5}
	α	0.238	0.309	0.100
Ethanol	E_f	0.61	0.61	0.63
	E_b	0.38	0.36	0.36
	I_f/I_b	0.82	0.78	0.63
	Intercept "*a*"	2.112	1.346	2.436
	Tafel slope "*b*" (V/dec)	0.479	0.273	0.449
	i_o at 0.6V (A/cm^2)	6.97×10^{-4}	1.85×10^{-3}	8.14×10^{-5}
	α	0.124	0.217	0.132

References:

[1]. M. K. Debe, *Nature* **486** (2012) 43-51.

[2]. C. Ma, W. Liu, M. Shi, X. Lang, Y. Chu, Z. Chen, D. Zhao, W. Lin, et al., *Electrochim. Acta* **114** (2013) 133-141.

[3]. L. Xiong, L. Zheng, C. Liu, L. Jin, Q. Liu, J. Xu, *J. Electrochem. Soc.* **162** (2015) F468-F473.

[4]. R. Borup, J. Meyers, B. Pivovar, Y. S. Kim, R. Mukundan, N. Garland, D. Myers, M. Wilson et al., *Chem. Rev.* **107** (2007) 3904-3951.

[5]. H. Tang, Z. Qi, M. Ramani, J. F. Elter, *J. Power Sources* **158** (2006) 1306-1312.

[6]. G. Jin, B. Xu, H. Wang, Q. Li, S. Wei, *Mater. Lett.* **61** (2007) 2454-2456.

[7]. H. H. Hwu, J. G. Chen, *Chem. Rev.* **105** (2004) 185-212.

[8]. W. Zhu, A. Ignaszak, C. Song, R. Baker, R. Hui, J. Zhang, F. Nan, G. Botton, et al., *Electrochim. Acta* **61** (2012) 198-206.

[9]. H. Zheng, Z. Chen, Y. Li, C. Ma, *Electrochim. Acta* **108** (2013) 486-490.

[10]. G. Li, C. Ma, Y. Zheng, W. Zhang, *Micropor. Mesopor. Mat.* **85** (2005) 234-240.

[11]. E. Weigert, D. Esposito, J. G. Chen, *J. Power Sources* **193** (2009) 501-506.

[12]. K. Lee, A. Ishihara, S. Mitsushima, N. Kamiya, K. Ota, *Electrochim. Acta* **49** (2004) 3479-3485.

[13]. J. D. Voorhies, *J. Electrochem. Soc.* **119** (1972) 219-222.

[14]. P. Zoltowski, *Electrochim. Acta* **31** (1986) 103-111.

[15]. J. Shim, C. R. Lee, H. K. Lee, J. S. Lee, E. J. Cairns, *J. Power Sources* **102** (2001) 172-177.

[16]. P. J. Kulesza, L. R. Faulkner, *J. Am. Chem. Soc.* **110** (1988) 4905-4913.

[17]. K. Huang, K. Bi, J. C. Xu, C. Liang, S. Lin, W. J. Wang, T. Z. Yang, Y. X. Du, et al., *Electrochim. Acta* **174** (2015) 172-177.

[18]. G. A. Tsirlina, O. A. Petrii, *Electrochim. Acta* **32** (1987) 637-647.

[19]. H. Chhina, S. Campbell, O. Kesler, *J. Power Sources* **164** (2007) 431-440.

[20]. F. Harnisch, U. Schröder, M. Quaas, F. Scholz, *Appl. Catal. B-Environ.* **87** (2009) 63-69.

[21]. Y. Liu, S. Shrestha, W. E. Mustain, *ACS Catal.* **2** (2012) 456-463.

[22]. P. K. Sahoo, S. S. K. Kamal, M. Premkumar, T. J. Kumar, B. Sreedhar, A. K. Singh, S. K. Srivastava, K. C. Sekhar, *Int. J. Refract. Met. H.* **27** (2009) 784-791.

[23]. M. J. Watt-Smith, J. M. Friedrich, S. P. Rigby, T. R. Ralph, F. C. Walsh, *J. Phys. D Appl. Phys.* **41** (2008) 174004 (1-8).

[24]. Y. T. Liu, Q. B. Yuan, D. H. Duan, Z. L. Zhang, X. G. Hao, G. Q. Wei, S. B. Liu, *J. Power Sources* **243** (2013) 622-629.

[25]. M. Shi, W. Zhang, D. Zhao, Y. Chu, C. Ma, *Electrochim. Acta* **143** (2014) 222-231.

[26]. C. Engelbrekt, N. Šešelj, R. Poreddy, A. Riisager, J. Ulstrupa, J. Zhang, *J. Mater. Chem. A* **4** (2016) 3278-3286.

[27]. E. C. Weigert, A. L. Stottlemyer, M. B. Zellner, J. G. Chen, *J. Phys. Chem. C* **111** (2007) 14617-14620.

[28]. X. Cui, H. Zhang, X. Dong, H. Chen, L. Zhang, L. Guo, J. Shi, *J. Mater. Chem.* **18** (2008) 3575-3580.

[29]. J. N. Soderberg, A. C. Co, A. H. C. Sirk, V. I. Birss, *J. Phys. Chem. B* **110** (2006) 10401-10410.

[30]. H. Meng, P. K. Shen, *J. Phys. Chem. B* **109** (2005) 22705-22709.

[31]. A. S. Aricòa, S. Srinivasanb, V. Antonucci, *Fuel Cells* **1** (2001) 133-161.

[32]. J. C. Amphlett, R. M. Baumert, R. F. Mann, B. A. Peppley, P. R. Roberge, *J. Electrochem. Soc.* **142** (1995) 1-8.

[33]. G. L. Soloveichik, *Beilstein J. Nanotechnol.* **5** (2014) 1399-1418.

[34]. F. Şen, S. Şen, G. Gökağaç, *Phys. Chem. Chem. Phys.* **13** (2011) 1676-1684.

[35]. G. A. Camara, T. Iwasita, *J. Electroanal. Chem.* **578** (2005) 315-321.

[36]. T. Huang, S. Mao, G. Zhou, Z. Zhang, Z. Wen, X. Huang, S. Ci, J. Chen, *Nanoscale* 7 (2015) 1301-1307.

[37]. E. Yoo, T. Okata, T. Akita, M. Kohyama, J. Nakamura, I. Honma, *Nano Lett.* **9** (2009) 2255-2259.

[38]. Y. Lin, X. Cui, C. H. Yen, C. M. Wai, *Langmuir* **21** (2005) 11474-11479

[39]. E. Telli, R. Solmaz, G. Kardaş, *Russ. J. Electrochem.* **47** (2011) 811-818.

[40]. E. L. Redmond, B. P. Setzler, F. M. Alamgir, T. F. Fuller, *Phys. Chem. Chem. Phys.* **16** (2014) 5301-5311.

[41]. Z. Fu, Q. M. Huang, X. D. Xiang, Y. L. Lin, W. Wu, S. J. Hu, W. S. Li, *Int. J. Hydrogen Energ.* **37** (2012) 4704-4709.

CHAPTER 6

CONCLUSIONS AND FUTURE SCOPE

Overview

This chapter summarizes the work done on the synthesis of WC and W_2C nano powders using different carbon sources and WO_3 as precursor. The variation in the reaction conditions has led to the development of different types of morphological features in the synthesized carbides which have been characterized using different techniques viz. XRD, DSC/TGA, BET, Raman and TEM. The results of electrochemical studies of these synthesized carbides in bare and platinum modified conditions with different solvents have been summarized and concluded in this chapter.

6.1 Conclusions

Metal carbides (MC) are different class of materials that show good electronic conductivity like metals. Apart from this, these materials are chemically inert, low cost, tolerance to CO poisoning as well as having high hardness even at higher temperature. Because of these properties these are mostly used in cutting tools. Among all metal carbides, tungsten carbides (WC/W_2C) are the materials, which have wide applications mostly for mechanical and electrochemical applications especially at nano scale. The properties of these materials are mainly dependent on the reactions conditions by which it is prepared (carburization by liquid hydrocarbon/solid carbon, time and synthesis temperature). Moreover, the performance of prepared tungsten carbides nano particles can be enhanced by encapsulating it with carbon layer which protect it from thermal and acidic attack. Hence, after considering all these facts, the main aim of the present work was to synthesize WC and W_2C nano particles from WO_3 using different carbon sources (liquid/solid) by single-step route (thermo-chemical) at low temperature. In the present work, the carbon coated tungsten carbides nano particles have been synthesized in self designed autoclave. For the synthesis of carbon coated carbide nano particles magnesium was used as reducing agent.

For the synthesis of WC nano powder at different temperature and time three different carbon sources have been used. After considering the reaction path of these three carbon sources, it can be concluded that the reduction as well as carburization process with acetone is fast as compared to other carbon sources because of the lower intermediate path even at lower temperature. Among all categories of synthesized WC nano powder, it has been observed that the sample prepared by solid carbon source has lower tensile strain as compared to samples obtained with liquid hydrocarbons. The results of thermal analysis indicate that the synthesized samples are thermally stable in air upto ~550 °C. The thermal analysis results also show that the maximum weight loss occurs at high temperature for samples obtained by liquid hydrocarbons which attributes their higher thermal stability. The presence of carbon coating around the obtained carbide particle in TEM/HRTEM images confirmed that the carbide particles obtained by liquid carburizing agent have faceted type morphology which is encapsulated by graphitic carbon. On the other hand, the carbide nano particles obtained using activated charcoal, contained spherical morphology coated with amorphous carbon layer. The influence of these carburizing agents as well carbon coating has also been attributed on the specific surface area of the obtained product, which is observed by BET method. This study indicates that the material obtained from the solid carbon source

exhibited higher active surface area due to involvement of amorphous carbon as compared to samples obtained by liquid carbon sources. The ordering and disordering in the carbon content produced with different carbon sources have also been analyzed by Raman spectroscopy which concluded that the product obtained by solid carbon source contained higher value of I_D/I_G ratio. This higher value of I_D/I_G ratio signifies the disordered characteristics due to which it attains lower thermal stability and higher surface area.

After considering the results obtained by WC nano powder the optimization has been done in the synthesis conditions (temperature, time and amount of carburizing agent) of W_2C using same carburizing agent (acetone and activated charcoal). Out of all synthesis conditions, it has been observed that 600 °C was the optimized synthesis temperature to get W_2C enriched product in 2 h synthesis time by using acetone (10 mL) and activated charcoal (0.5 g). However, by using another carburizing agent (hexane) the condition of semi-carburization cannot be achieved by adopting the similar synthesis conditions as followed by acetone. Moreover, it has also been observed that the samples which prepared by solid carbon source have minimum strain as compared to samples prepared by liquid hydrocarbons. One of the aspects has also been observed from the strain analysis that due to the deficiency of carbon atom in W_2C the order of strain is lower as compared to WC. The onset temperature of oxidation corresponding to DSC peak has been shifted to lower temperature for sample obtained by solid carbon source which attributes the lower thermal stability of sample. The TEM/HRTEM images show that the obtained carbide particles encapsulated by graphitic carbon and have different morphology viz. spherical and faceted in case of liquid carbon sources. While, the product obtained by solid carbon source exhibit spherical morphology encapsulated by amorphous carbon layer. The sample prepared by solid carbon source exhibited higher surface area as compared to samples obtained with liquid carbon source. The nature of carbon (graphitic/amorphous) present in the product has also been analyzed by Raman spectroscopy which provide higher value of I_D/I_G for the product obtained by solid carbon source. This value exhibits amorphous nature of carbon in the product which is in well agreement with BET and TEM analysis.

Electrochemical study of synthesized nanopowder

The results of CV attribute that the electrode (WC and W_2C) prepared by solid carbon source exhibits better electrocatalytic activity as compared to other electrodes prepared by liquid carbon source. The W_2C phase enriched sample shows clear evidence of hydrogen

evolution process without any supporting element (Pt, Pd). Further, after the platinum deposition the W_2C enriched phase attributes more prominent peak corresponding to oxygen reduction reactions. The results of the alcohol (methanol/ethanol) electro-oxidation reveal that all the prepared electrocatalysts (WC/W_2C) shows better electrochemical performance in terms of higher exchange current density for methanol oxidations. But, among all the electrocatalysts, the electrocatalyst obtained by solid carbon source, inspite of lower tolerance of CO provide higher exchange current density as well as the reaction rate.

6.2 Future Scope

The present work has confirmed that single phase WC nano powder can be obtained by changing the carburizing agent. However, it is difficult to obtain single phase W_2C nano particles by current synthesis method. So, by changing the carburizing agent, the single phase W_2C can be synthesized achieved by controlling the carbon diffusivity in the system using other carbon source. Furthermore, the electrochemical studies of carbides obtained by current method can be done with another nobel metals (Pd, Au, Ru) in different acidic media and alcohol(s).